Modelling of the heat and mass transfers near reactive walls : application to the oxidation of carbonaceous compounds in after-treatment devices

Adam Chabane

NNT : 2015SACLC028

THÈSE DE DOCTORAT
DE
L'UNIVERSITÉ PARIS-SACLAY
PREPARÉE A
CENTRALESUPÉLEC

ÉCOLE DOCTORALE N° 579

Sciences mécaniques et énergétiques, matériaux et géosciences

Spécialité énergétique

Par

Adam Mounsif Chabane

Modélisation des transferts de masse et de chaleur au voisinage de parois réactives.
Applications à l'oxydation de composés carbonés pour le post-traitement.

Thèse présentée et soutenue à Rueil-Malmaison, le 08 décembre 2015:

Composition du Jury :

Pr.	O. Simonin	INPT/IMFT	Président
Pr.	C. Jimenez	CIEMAT Madrid	Rapporteure
Pr.	E. Shaer	LRGP Nancy	Rapporteur
Dr., HDR.	G. Moreac-Njeim	RENAULT	Examinatrice
Pr.	L. Catoire	ENSTA ParisTech	Examinateur
Dr., HDR.	C. Angelberger	IFPEN	Directeur de thèse
Pr.	F. Nicoud	Université de Montpellier II	Co-directeur de thèse
Dr.	K. Truffin	IFPEN	Encadrante

université PARIS-SACLAY
ÉCOLE DOCTORALE
Sciences mécaniques et énergétiques, matériaux et géosciences (SMEMAG)

Titre : Modélisation des transferts de masse et de chaleur au voisinage de parois réactives. Applications à l'oxydation de composés carbonés pour le post-traitement.

Mots clés : parois réactives, combustion, catalyse, cinétique chimique, conditions aux limites.

Résumé : la crise environnementale a conduit l'industrie automobile à faire face à des contraintes croissantes tandis que les limitations drastiques de polluants entrent en vigueur. Afin de réduire les émissions polluantes issues de la combustion, l'une des solutions adoptées est de post-traiter les fumées à l'aide de systèmes de post-traitement catalytique à l'image du catalyseur 3 voies (TWC) pour les moteurs à essence ou le catalyseur d'oxydation (DOC) pour les moteurs diesel. Ces appareils présentent une structure en nid d'abeille constituée d'un réseau de canaux à l'échelle millimétrique appelés monolithes et dont les parois intérieures sont recouvertes d'une fine couche de métal précieux aux propriétés catalytiques. Les polluants sont transformés via l'interaction entre les molécules présentes dans la phase gaz et les sites actifs du métal précieux. Etant donné les conditions laminaires d'écoulement au sein des monolithes, un mélange faible et une diffusion moléculaire limitée peuvent être rencontrés au voisinage de la paroi réactive. Le taux de conversion des polluants peut être alors insuffisant pour des conditions opératoires données. Dans le but d'optimiser les transferts, des obstacles peuvent être introduits par déformation mécanique des parois du canal catalytique au cours du processus de fabrication. Les simulations numériques peuvent contribuer à l'émergence de solutions innovantes basées sur une compréhension et une maitrise profonde des phénomènes sous-jacents. Afin d'atteindre cet objectif, le premier élément clé a été de formuler et d'intégrer dans le code de dynamique des fluides AVBP une approche numérique combinant d'une part des conditions aux limites dédiées à la prise en compte de parois réactives, et d'autre part, la résolution de la cinétique chimique gaz et surface via un solveur d'EDP.

L'approche a permis la prise en compte de la cinétique détaillée et l'interaction entre la phase gaz et les parois réactives. L'outil développé a été validé en premier lieu à l'aide de calculs de réacteurs hétérogènes zéro-dimensionnels. Les résultats ont montré un parfait accord avec le solveur de référence SENKIN. L'approche a été validée ensuite en l'appliquant à la simulation de deux canaux réactifs aux parois planes et en comparant les résultats numériques aux résultats expérimentaux de Dogwiler *et al.* L'approche développée s'est révélée être capable de reproduire les principales caractéristiques de la combustion catalytique pour différents points de fonctionnement. Enfin, l'outil développé a été appliqué à l'étude de l'impact de l'introduction d'obstacles pariétaux sur les taux de conversion des systèmes catalytiques. Les résultats ont permis d'ouvrir des perspectives très intéressantes quant à la contribution de la CFD 2D et de la chimie hétérogène détaillée à l'optimisation du design des systèmes de post-traitement catalytique. En particulier, l'étude de l'influence des obstacles pariétaux a montré que le design de la géométrie des monolithes constitue un fort potentiel d'optimisation de l'efficacité des systèmes de conversion catalytique et ce, à moindre coût grâce à une utilisation optimisée du métal précieux rendue possible par une meilleure interaction entre l'écoulement, les réactions chimiques dans la phase gaz et la paroi réactive.

Université Paris-Saclay
Espace Technologique / Immeuble Discovery
Route de l'Orme aux Merisiers RD 128 / 91190 Saint-Aubin, France

Title: Modelling of the heat and mass transfers near reactive walls. Application to the oxidation of carbonaceous compounds in after-treatment devices.

Keywords: reactive walls, combustion, catalysis, chemical kinetics, boundary conditions.

Abstract: the environmental emergency has led automotive industry to deal with growing constraints as drastic regulations of pollutant emissions are emerging. In order to reduce emissions resulting from the combustion process, one of the solution adopted is to post-process pollutants by the means of catalytic after-treatment systems such as three-way converters (TWC) for gasoline applications or oxidation catalysts (DOC) for Diesel applications. These devices present a honeycomb shape which consists in a grid of millimeter-scale narrow channels called monoliths whose interior wall are coated with precious metals presenting catalytic properties. Pollutants are converted through the chemical interaction involving gas-phase molecules and active precious metal sites. Given the laminar flow encountered within these monoliths, weak mixing and molecular diffusion could occur near the catalytic walls. Pollutant conversion rates may therefore prove insufficient for certain operating conditions. In order to promote transfers, obstacles could be introduced by mechanically deforming the channel wall during the manufacturing process. Numerical simulations can contribute to the emergence of innovative technologies based on a profound understanding and mastering of the underlying phenomena that simulation allows. In order to achieve this goal, a first key element was the formulation and integration into the AVBP CFD code of a numerical approach combining specific boundary conditions for reactive walls and ODE solvers for the gas phase and surface chemistry. The approach allowed to account for detailed kinetics and the interplay between the reactive surface and the gas-phase. The resulting tool was first validated using a zero-dimensional heterogeneous reactor computations. The results were shown to perfectly match the ones obtained with the reference kinetic solver SENKIN. Furthermore, the approach was then validated by applying it to the simulation of two planar reactive channel flows, and comparing the predictions with experimental findings of Dogwiler *et al*.. The developed approach proved to be able of reproducing main features of the catalytic combustion observed for different operating points. Finally, the developed tool was applied to explore the impact of introducing wall obstacles on the conversion rate of catalytic devices. The resulting findings have proved to open very interesting perspectives for contributing to the optimization of the design of catalytic converters using 2D CFD and detailed heterogeneous chemistry. In particular, the study of the impact of wall obstacles indicates the potential for contributing to further increase the efficiency of catalytic converters via the design of monolith geometries that would allow a more efficient and thus less costly usage of Pt-coating as a consequence of optimized interactions between the gas flow, gas phase chemistry and surface chemistry.

REMERCIEMENTS

Cette thèse de doctorat n'aurait jamais été accomplie sans la participation et le soutien de nombreuses personnes. Je tiens tout d'abord à remercier mon équipe encadrante qui m'a permis de réaliser et d'achever avec succés mes travaux au sein de l'IFPEN. Merci à la pertinence, rigueur et pragmatisme de mes directeurs de thèse Christian et Franck qui ont toujours su donner une direction à mes travaux même pendant les moments oú je semblais être totalement perdu. Je m'incline aussi devant la patience, tolérence et disponibilité de Karine et André qui n'ont jamais hésité à mettre les mains dans le cambouis.

Ces trois dernières années n'auraient pas été possibles sans le maintien d'un niveau intellectuel trés élevé en CB309 dont les porte-drapeaux sont mes amis et collègues Nicolas et La gork. Je n'oublie pas bien entendu les personnes qui ont su nous léguer cette culture: Carlo, Stéphane, Anthony et julien sans oublier JB Michel. Benji, Betty, Haifa, Lama, Elias, Karl, Federico, Valerio, Hugo, Pablo, Sophie et Mamady: merci à vous aussi pour votre soutien permanent. Merci à Elefterios et Edouard qui ont mis la barrière intellectuelle encore plus haut et ont su apporter un vent de fraîcheur à cette dernière année de thèse. Petite pensée également aux derniers arrivés qui n'ont pas l'air moins intelligents : Matthieu et le roux.

Je voudrais également remercier pour leur participation et nombreux conseils Olivier cabrit, Olivier Colin, Anthony Velghe, Stéphane Jay et Antonio Pires Da Cruz. Merci également à Nathalie, Amel et Irène pour leur disponibilité.

Enfin, je tiens à remercier mon entourage qui sans doute ne lira jamais cette thèse et n'y comprendrait pas grand chose de toute façon. Je pense ainsi à mes parents et à mes sœurs qui ont toujours été présents, à mes vieux amis Max, Jo, Fadi, Matthieu, Fayçal, Marianna, Amira, Nassim et toute la bande de Rouennais et Algerois. Je tire également chapeau à mes colocataires Nadjib, Karim et Walid qui ont su me supporter pendant ces trois dernières années.

Nomenclature

Roman letters

A_r	pre-exponential factor of the r^{th} gas-phase reaction, (mol, cm, s)
A_r^s	pre-exponential factor of the r^{th} surface reaction, (mol, cm, s)
$A_r^{s,cov}$	Coverage dependent pre-exponential factor of the r^{th} surface reaction, (mol, cm, s)
C_M	third body mole concentration, $\left(mol.m^{-3}.s^{-1}\right)$
C_k	mole concentration of the k^{th} gas-phase species, $\left(mol.m^{-3}.s^{-1}\right)$
C_k^s	mole concentration of the k^{th} surface species,$\left(mol.m^{-2}.s^{-1}\right)$
$C_{p,k}$	heat capacity at constant pressure, $\left(J.kg^{-1}.K^{-1}\right)$
$C_{v,k}$	heat capacity at constant volume, $\left(J.kg^{-1}.K^{-1}\right)$
D_k	mass diffusion coefficient of the k^{th} gas-phase species, $\left(m^2.s^{-1}\right)$
$D_{k,j}$	binary mass diffusion coefficient of the k^{th} gas-phase species to j^{th} species, $\left(m^2.s^{-1}\right)$
Da	Damköhler number, (s)
$Da\|_{AI}$	Damköhler number based on the auto-ignition time, (s)
dt_{CFL}	time step based on the acoustics, (s)
dt_{chem}	time step based on the gas-phase chemical reactions, (s)
dt_{F_o}	time step based on the diffusive transport, (s)
$dt_{chem}^{surface}$	time step based on surface reactions, (s)
E	total non-chemical energy, $\left(J.kg^{-1}\right)$
Ea_r	activation energy of the r^{th} gas-phase, $\left(J.mol^{-1}\right)$
Ea_r^s	activation energy of the r^{th} surface reaction, $\left(J.mol^{-1}\right)$
$Ea_r^{s,cov}$	coverage dependent activation energy of the r^{th} surface reaction, $\left(J.mol^{-1}\right)$
Fo	Fourier number
$h_{s,k}$	sensible enthalpy of the k^{th} species, $\left(J.kg^{-1}\right)$
h_k	total enthalpy of the k^{th} species, $\left(J.kg^{-1}\right)$
h_c	channel half-height, (m)
I_k	surface to gas-phase chemical rates ratio
$\triangle h_{f,k}^o$	standard enthalpy of formation of the k^{th} species, $\left(J.kg^{-1}\right)$
$\vec{J_k}$	diffusive flux of the k^{th} gas-phase species, $\left(kg.m^{-2}.s^{-1}\right)$
k_r^f	forward rate constants of the r^{th} gas-phase reaction, (mol, cm, s)
$k_r^{s,f}$	forward rate constants of the r^{th} surface reaction, (mol, cm, s)
K_r^{eq}	equilibrium constant of the r^{th} gas-phase reaction, (mol, cm, s)
$K_r^{s,eq}$	equilibrium constant of the r^{th} surface reaction (mol, cm, s)

Roman letters

l_{diff}	characteristic diffusion length within a chemical time, τ_{chem}
L_f	axial thickness of the gas-phase reaction front, (m)
Le	Lewis number
m_c	surface carbon mass, (kg)
$\dot{m}$	convected mass rate at the wall, $\left(kg.m^{-2}.s^{-1}\right)$
p	Thermodynamic pressure, (Pa)
Pr	Prandtl number
Pt	Platinum
$\vec{q}$	heat flux, $\left(J.m^{-2}.s^{-1}\right)$
Re	Reynolds number
$\mathcal{Q}_r$	reaction rate of the r^{th} gas-phase reaction, $\left(mol.m^{-3}\right)$
$\mathcal{Q}_r^s$	reaction rate of the r^{th} surface reaction, $\left(mol.m^{-2}\right)$
R	universal gas constant, $\left(J.mol^{-1}K^{-1}\right)$
R_k^{chem}	rate of change of the k^{th} gas-phase species due to gas-phase reactions
$R_k^{s,chem}$	rate of change of the k^{th} gas-phase/surface species due to surface reactions
R_k^{conv}	rate of change of the k^{th} gas-phase species due to convective transport
R_k^{diff}	rate of change of the k^{th} gas-phase species due to diffusive transport
$\dot{s}_k$	rate of production by surface reactions of the k^{th} species, $\left(kg.m^{-2}.s^{-1}\right)$
$\dot{s}_k^{hom}$	rate of production by surface reactions of the k^{th} species determined by the kinetic solver, $\left(kg.m^{-2}.s^{-1}\right)$
Sc_k	Schmidt number of the k^{th} species
t	physical time (s)
t_{AI}	*a priori* estimated ignition time
t_{diff}^{spec}	diffusion characteristic time of gas-phase species
T	temperature, (K)
T^{hom}	temperature seen by the kinetic solver, (K)
$\vec{u}$	velocity vector, $\left(m.s^{-1}\right)$
U_{Stefan}	Stefan velocity,$\left(m.s^{-1}\right)$

Roman letters

$\vec{V}_k$	diffusion velocity field of the k^{th} gas phase species, $\left(m.s^{-1}\right)$
W_k	molecular weight of the k^{th} gas phase species, $\left(kg.mol^{-1}\right)$
W_k^s	molecular weight of the k^{th} surface species, $\left(kg.mol^{-1}\right)$
W_{ads}^s	molecular weight of the adsorbed species
x_{stab}	flame anchoring position
X_k	mole and mass fraction of the k^{th} gas phase species
X_f	axial position of the gas-phase reaction front
x'	axial coordinate normalized by the channel length
Y_k	mass fraction of the k^{th} gas phase species
Y_k^{eq}	mass fractions of the k^{th} gas-phase species at the steady state.
Y_k^{hom}	mass fractions of the k^{th} gas-phase species seen by the kinetic solver
y'	transverse coordinate normalized by the channel height

Greek symbols

β_r^s	temperature exponent of the r^{th} gas-phase reaction
β_r^s	temperature exponent of the r^{th} surface reaction
$\bar{\bar{\delta}}$	*Kronecker* symbol
$\varepsilon_{k,r}$	surface coverage parameter for activation energy of the r^{th} species involved in the r^{th} surface reaction
$\eta_{k,r}$	surface coverage parameter for the pre-exponential factor of the r^{th} species
γ_r	sticking coefficient for adsorption reactions
Γ	surface site density, $\left(mol.m^{-2}\right)$
λ	heat conduction coefficient, $\left(W.m^{-1}.K^{-1}\right)$
μ	dynamic viscosity, $(Pa.s)$
$\nu_{k,r}^f$	molar stoichiometric coefficient of the k^{th} gas phase species present as a reactant
$\nu_{k,r}^b$	molar stoichiometric coefficient of the k^{th} gas phase species present as a product in the r^{th} reaction
$\nu_{k,r}^{s,f}$	molar stoichiometric coefficient of the k^{th} surface species present as a reactant in the r^{th} reaction
$\nu_{k,r}^{s,b}$	molar stoichiometric coefficient of the k^{th} surface species present as a product in the r^{th} reaction
Ω_G	index set of gas-phase species involved in gas-phase and surface reactions
Ω_s	index set of surface species involved in surface-phase reactions

Greek symbols

$\dot{\omega}_k$	rate of production by gas-phase reactions of the k^{th} species, $\left(kg.m^{-3}.s^{-1}\right)$
$\dot{\omega}_k^{hom}$	rate of production by gas-phase reactions of the k^{th} species determined by the kinetic solver, $\left(kg.m^{-3}.s^{-1}\right)$
$\dot{\omega}_T$	gas-phase heat release rate in, $\left(J.m^{-3}.s^{-1}\right)$
$\dot{\omega}_T^{eq}$	gas-phase heat release at the steady state, $\left(J.m^{-3}.s^{-1}\right)$
$\vec{\psi}$	set of variables undergoing gas-phase reactions
$\vec{\Pi}$	set of variables undergoing surface reactions
ρ	gas-phase density, $\left(kg.m^{-3}\right)$
σ_k	Number of sites that each adsorbed species occupies
$\bar{\bar{\tau}}$	viscous stress tensor, $\left(kg.m^{-1}.s^{-2}\right)$
θ_k	surface site fraction
τ	normalized time
χ_k	thermal diffusion ratios

indexes

i,j	refers to the direction of a vector component
k	refers to the k^{th} species
n	refers to wall-normal vectors
s	refers to surface reactions
w	denotes for vectors or scalars at the wall

Abbreviations

AI	auto-ignition
MCR	mass conversion rate
ODE	ordinary differential equation

Contents

List of Figures

List of Tables

Chapter 1

Context & introduction

Automotive industry is dealing with growing constraints as drastic regulations of pollutant emissions are emerging. For instance, the limits of pollutant rejections imposed by the EURO norms [8] are becoming tougher and tougher since 1993. The stringency of the norms is highlighted in Figure 1.1 thus showing the political will of reducing the environmental impact of road transport.

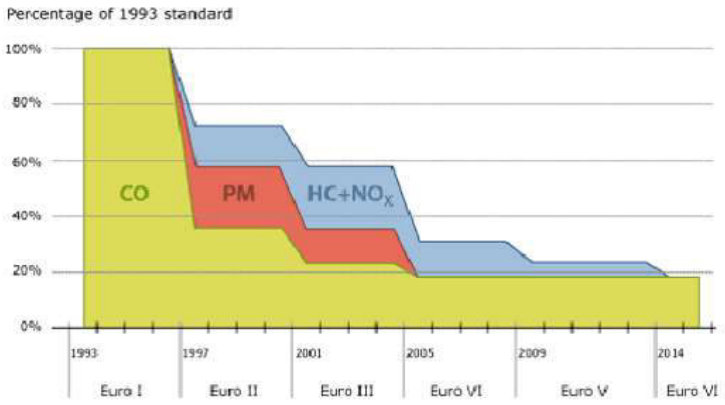

FIGURE 1.1: Stringency of the norms since 1993 [1]. CO, NO_x and HC stand for carbon monoxide, nitrogen oxides and hydrocarbon compounds respectively. PM refers to particulate matter.

Post-processing emissions by the means of devices embedded downstream from internal combustion engines (ICE) is one of the solutions adopted by car manufacturers to reduce pollutants. Solid emissions such as particulate matter (PM) can be trapped inside particulate filters [9] while gaseous pollutants (CO, HC and NO_x) are converted inside catalytic after-treatment systems such as three-way converters (TWC) for gasoline applications [10] or oxidation catalysts (DOC) for Diesel applications [11]. Automotive pollutant control devices for gaseous emissions present a honeycomb shape which consists in a grid of ceramic

or metallic made millimeter-scale narrow channels called monoliths. Interior walls of monoliths are coated with a metal oxide porous layer known as washcoat over which precious metal crystalites (Rhodium/Platinum) presenting catalytic properties are distributed. Pollutants are converted through reactions occurring at the catalytic wall of the monoliths where gas-phase molecules and active precious metal sites are involved.

In these kind of applications, catalysis favors and provides reaction paths that would not be possible or infinitely slow under typical exhaust gas thermodynamic conditions.

Figure 1.2a illustrates the channel network structuring the honeycomb-shaped catalytic converter. Figure 1.2b gives a more detailed view of the monolith interior by showing how the porous layer is bonded to the surface of the support. The main function of the washcoat is to provide high surface area needed for the dispersion of catalytic metals to ensure a better conversion. Inorganic base metal oxides can be added to the wash coat as stabilizers.

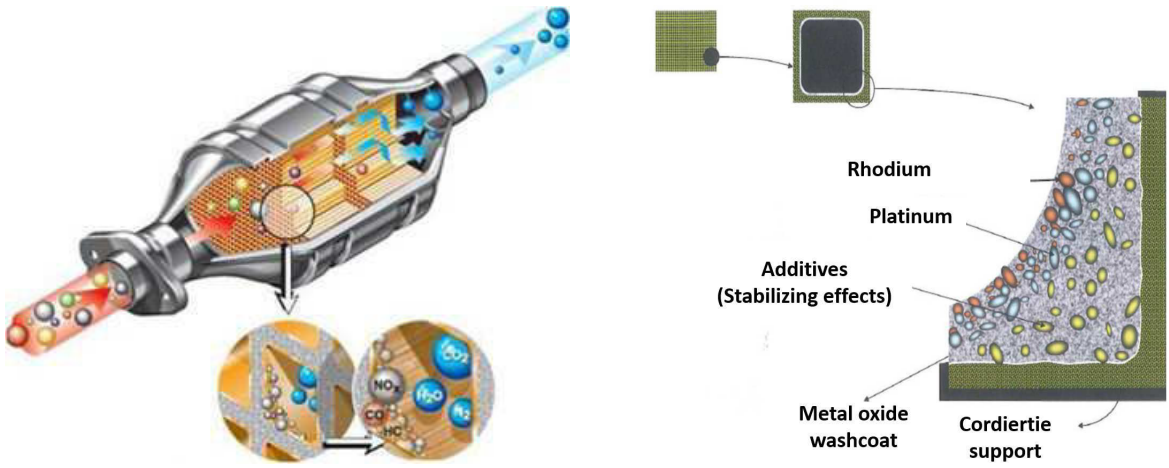

(A) Honeycomb shaped catalyst

(B) Catalytic coating

FIGURE 1.2: Left: Structure of a honeycomb-shape catalyst [2]. Right: Catalyst washcoat [3].

Although the flow is turbulent in the exhaust-gas upstream from the catalyst with a Reynolds number of 5000-80000 [12], flows encountered within narrow monolithic channels of converters are laminar with prevailing Reynolds number between 75-600 [13]. Typical reaction rate curves for catalytic systems are plotted versus temperature in Figure 1.3. Below 500K, the line (orange) follows an exponential growth which corresponds to a purely kinetic regime i.e, surface reactions do not undergo transfer limitations. At this temperature range surface reactions are prevailing in the absence of gas-phase ones. For temperatures above 1200K, homogeneous reactions rates which are represented by the red line are dominating. Under this regime which is referred as CST (Catalytically Stabilized Thermal combustion) [14], catalytic

reactions tend to stabilize homogeneous reactions. Under the temperature range that is highlighted in purple (500K-1200K) homogeneous reactions are activated, however their rates remain low compared to surface ones. The line of the surface reaction rates reaches a plateau (blue dashed line) as a consequence of weak mixing and diffusion that occur near the reactive walls. This results in heat and mass transfer limitations. Therefore, the catalytic conversion rates could be limited by molecular diffusion fluxes and chemical kinetics, which may prove insufficient for certain operating conditions. This regime that is characterized by surface reactions undergoing kinetic and diffusion limitation in the presence of a gas-phase chemical activity corresponds to the operating domain of automotive catalytic converters.

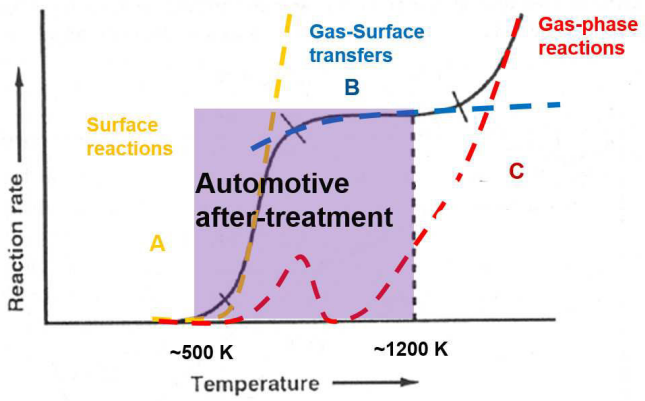

FIGURE 1.3: Typical rate curve for catalytic systems [4]. A: kinetic regime; B:heat and mass transfer limitation; C: gas-phase reactions

In order to enhance transfers under this operating range, Figure 6 shows how a transfer promoter in the form of an obstacle could be introduced on the otherwise smooth interior walls of the monoliths [15]. These obstacles are created by mechanically deforming the channel wall during the manufacturing process. Different possible wall/obstacle shapes such as baffles, helical/rectangular ribs, sinusoidal/corrugated walls or dimpled tubes and wire coal inserts [16, 17] can therefore be obtained.

The contact between the pollutant species carried by the exhaust-gas flow and the catalytic metals at the surface could thereby be enhanced. The resulting flow perturbations, in the form of e.g. recirculation, could lead to higher heat and mass transfer rates to the channel wall and thus larger reaction rates at the surface, which could improve the overall performance of the system. Moreover, the resulting enhancement of transfers and reactivity may enable to reduce the amount of catalytic metals used for coating as the available reactive contact area would be optimized.

Understanding in detail the underlying chemical and physical phenomena inside monolithic channels could be a key path in order to identify potential technological improvements which might concern the

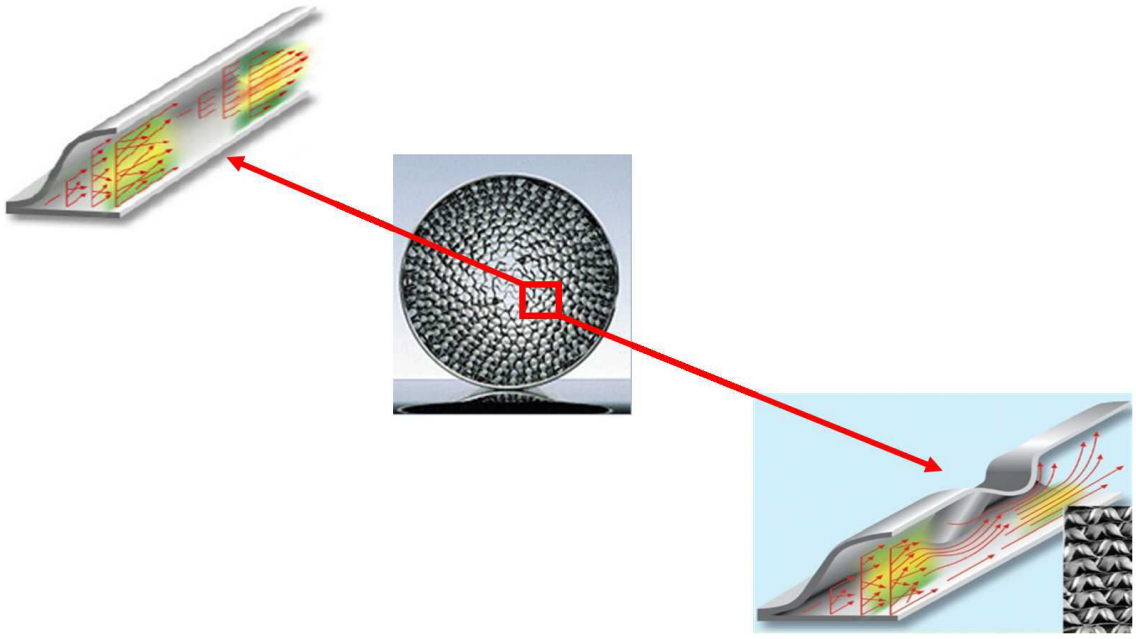

FIGURE 1.4: Introduction of a transfer promoter in the shape of a semi-spherical rib on the wall of a monolithic catalyst [5]

obstacles' shape, their numbers and dimensions. The design of obstacles and the amount of precious metal coating should thereby be explored for an optimized and cost-effective conversion performance.

Industrial context and objectives of the present study:

As vehicle emissions are limited by more and more drastic policies, pollution control actions are taken at the source, i.e, by developing new type of fuels [18] and clean combustion modes or by post-processing the exhaust-gas emissions through efficient after-treatment devices which is the focus of the present study. In order to explore optimization strategies, experiments could be carried out but under restricted configurations. Moreover, measurements are limited given the involved confinement and high chemical reactivity [6]. Therefore, numerical simulations appear to be a practical tool for system optimization as realistic operating conditions could be explored. Nonetheless, experimental data remain necessary in order to validate the numerical modeling. The use of reliable numerical tools can contribute to the emergence of innovative technologies based on a profound understanding and mastering of the underlying phenomena that simulation allows. The present study aims at developing and adapting an already existing numerical tool to study the flow within millimeter-scale channels with catalytic walls representative of catalytic monoliths and to numerically evaluate the effect of obstacles introduction on the local reactivity and transfers.

The burnt gases expelled from the combustion chamber and entering the after-treatment system and the

monolith channels are composed of an important number of chemical species resulting from the combustion process, and from the conditions found during expansion and flow through the exhaust ducts. The underlying physicochemical processes within each channel of a typical honeycomb structure are illustrated in Figure 1.5. As the multi-species flow interacts with the catalytic metals, catalytic ignition (light-off) and gas-phase reactions (homogeneous ignition) could be achieved depending on the operating conditions ($U_{IN},\ T_{IN},\ Y_{IN}$) and on the heat transfer mechanisms such as transverse diffusion, heat conduction in the solid channel walls and surface radiation heat transfer.

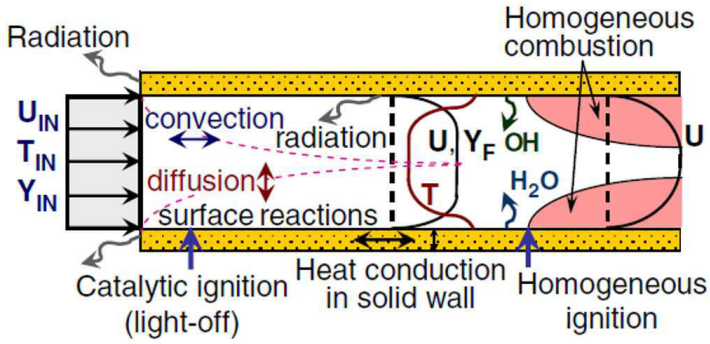

FIGURE 1.5: Physicochemical processes possibly occurring in a catalytic channel [6]

Surface reactions result in the production of gas-phase species that diffuse in the channel, e.g. H_2O and OH but also they might yield a deficient reactant on the catalyst surfaces as illustrated by the fuel mass fraction Y_F in Figure 1.5. This adsorption and desorption activity at the reactive wall thereby modifies the wall gradient of the gas-phase species and leads to a mass flux at the reactive interface known as *Stefan* flux [19, 20]. These features make the reactive interface behave as a transpiring wall [21]. In addition to wall heat losses and heat transfers with the gas-phase, surface reactions might be exothermic or endothermic which yields a heat release or adsorption in the near-wall region. These dynamics therefore modify the momentum, heat and mass transfer in the vicinity of the wall and imply that standard assumptions of impermeable and isothermal/adiabatic walls are no longer valid as compared to inert-wall conditions [22, 23]. Also, the underlying processes yielding the activation of both surface and gas-phase chemistry involved in pollutant conversion are transient. The following physical features thereby should be taken into account :

- Multi-species flows.
- Presence of both gas-phase and surface reactions.
- Variable density due to the interplay between chemical reactions and hydrodynamics.

- Modification of the momentum, mass and heat-flux at the reactive wall due to surface reactions.
- Radiative transfers and wall heat conduction.
- Transient behavior.

The variable density code AVBP co-developed at IFPEN and CERFACS solves the compressible unsteady 3D Navier-Stokes equations including gas-phase chemical reactions. At the start of the present work, the numerical methods were not adapted for the resolution of complex gas-phase kinetics. Simplified one- or two-step kinetics are however not sufficient to describe with sufficient accuracy the gas phase chemistry in catalytic monolith, especially as surface chemistry has also to be accounted for. Another alternative could be the development of chemistry tabulation approaches, but this path was not followed due to the *a priori* difficulty to account for surface chemistry in such approaches. For instance, defining a progress variable accounting for heterogeneous reactions might represent a very challenging task.

During the previous study of Cabrit *et al.* [24, 25], boundary conditions simulating the impact of surface reactions on the momentum and mass transfer at the reactive wall were implemented in AVBP . Simplified one- and two-step kinetics were used to describe surface reactions. Nevertheless, reactive walls were considered isothermal and complex surface kinetics with the associated numerical resolution were not addressed. The objective of the present work was to develop an approach that could addresse all main physical and chemical phenomena of importance for the simulation of catalytic monoliths, with the following main targets:

- Accounting for elementary chemical reactions and radical species within the description of chemical reactions of the gas-phase and the catalytic wall is essential in order to capture transient chemical phenomena such as gas-phase ignition and catalytic light-off. As detailed kinetic mechanisms include a large number of radicals, a large spectrum of species characteristic times is involved. As a result, the implementation of robust and fast ODE solver for both chemical kinetics is required to handle the induced stiffness with an acceptable accuracy and computational cost;
- Formulation of proper boundary conditions for determining wall fluxes in the presence of surface chemistry;
- Understanding the influence of obstacles on the reactivity and near-wall transfers by performing numerical simulations of the heterogeneous combustion in a narrow channel with catalytic walls representative of monolithic catalysts encountered in automotive converters.

Organization of the manuscript

This Ph.D manuscript is divided into seven Chapters:

- In the first Chapter, the general context was presented.
- The second Chapter describes the conservation equations governing multi-species reactive gaseous flows. The formulation of the *Navier-Stokes* equations and the numerical method used by the CFD code are reported. The gas-phase chemistry equations are detailed, along with the associated numerical resolution methods.
- Governing equations for surface reaction kinetics are introduced in the third Chapter. The derivation of a boundary condition dedicated to the prediction of a proper wall heat flux in the presence of surface reaction is presented. The overall numerical methodology enabling to account for reactive walls in a CFD code is depicted, as well as the numerical resolution method for complex surface kinetics.
- The fourth Chapter consists of a 1D application example that corresponds to the results of our published article in the International Journal of Heat and Mass transfer (IJHMT) [26]. Transient numerical simulation of the ignition of a gas mixture by a reactive wall in a quiescent flow is performed. The interplay between gas-phase diffusion and surface chemistry is emphasized.
- In the fifth Chapter, a 2D numerical simulation of combustion of lean premixed CH_4/Air mixture in a Pt-coated meso-scale channel with flat walls is described. Numerical results are compared to experimental data provided at steady-state by Dogwiler *et al.* [27] for validation. Moreover, a transient analysis is carried out to provide insight into the dynamic of heterogeneous chemistry encountered within catalytic channels.
- The sixth Chapter is dedicated to presenting numerical simulation results of combustion in a catalytic channel with wall obstacles. Convex and concave cavities were introduced to the planar catalytic channel studied in the fifth Chapter. The planar channel, serving as a reference case, enables to study the impact of obstacles on the conversion performances. The influence of full and segmented Pt-distribution is also assessed in order to assist coating optimization strategies.
- Finally, the last chapter is dedicated to the conclusions and perspectives of the present thesis.

Chapter 2

Governing flow equations and their resolution

2.1 Conservation equations

2.1.1 Navier-Stokes equations

Note: in this Section, the Einstein summation rule is used

The *Navier-Sokes* equations are described for multi-species compressible reactive flows. The considered variables used to describe the conservation laws are the density ρ, the mass fractions Y_k, the velocity vector u_i, the total non-chemical energy E and the thermodynamical static pressure p :

$$\frac{\partial \rho}{\partial t} + \frac{\partial \left(\rho u_i\right)}{\partial x_i} = 0 \tag{2.1}$$

$$\frac{\partial \left(\rho Y_k\right)}{\partial t} + \frac{\partial \rho \left(\left(u_i + V_{k,i}\right) Y_k\right)}{\partial x_i} = \dot{\omega}_k \tag{2.2}$$

$$\frac{\partial \left(\rho u_i\right)}{\partial t} + \frac{\partial \rho \left(\rho u_i u_j\right)}{\partial x_j} = -\frac{\partial p}{\partial x_i} + \frac{\partial \tau_{i,j}}{\partial x_j} \tag{2.3}$$

$$\frac{\partial \left(\rho E\right)}{\partial t} + \frac{\partial \left(\rho E u_i\right)}{\partial x_i} = -\frac{\partial q_i}{\partial x_i} + \frac{\partial \left(\tau_{i,j} u_i\right)}{\partial x_j} - \frac{\partial \left(p u_i\right)}{\partial x_i} + \dot{\omega}_T \tag{2.4}$$

$$\frac{p}{\rho} = rT \tag{2.5}$$

Eqs. (2.1-2.5) respectively correspond to the conservation of mass, species, momentum, total non-chemical energy and the ideal gas law. It is stressed that several variables could describe the energy conservation of a multi-species flow [28]. Here, the total non-chemical energy is chosen :

$$E = \sum_{k \in \Omega_G} h_{s,k} Y_k - (p/\rho) + \frac{1}{2} u_i u_j \tag{2.6}$$

$h_{s,k}$ is the sensible enthalpy of k^{th} gas-phase species and is related to the mass heat capacity at constant pressure $C_{p,k}$ using the following expression :

$$h_{s,k} = \int_{T_0}^{T} C_{p,k} dT \tag{2.7}$$

where $\Omega_G = [1, N_g]$ with N_g referring to the total number of gas-phase species in the mixture. $h_{s,k}$ stands for the sensible enthalpy of the k^{th} gas-phase species. In Eqs. (2.1-2.5), $V_{k,i}$ is the i^{th} component of the diffusion velocity of the k^{th} gas-phase species. It characterizes the molecular transport properties of the mixture. This aspect will be developed further in this Chapter (Subsection 2.1.2). $\dot{\omega}_k$ stands for the rate of production/consumption of the k^{th} species by gas-phase chemical reactions while $\dot{\omega}_T$ refers to the heat release or adsorption rate due to gas-phase chemical reactions. Radiative heat transfers are taken into account in the energy equation. This assumption will be discussed further in this report.

The ideal gas law is used in order to close the system where r refers to the mixture constant defined as :

$$r = \frac{R}{W} \tag{2.8}$$

where $R = 8.314 J \cdot mol^{-1} \cdot K^{-1}$ stands for the ideal gas constant, and W is the mean molecular wight of the mixture :

$$W = \sum_{k \in \Omega_G} X_k W_k = \left(\sum_{k \in \Omega_G} Y_k / W_k \right)^{-1} \tag{2.9}$$

X_k and W_k respectively refer to the mole fraction and the molecular wight of the k^{th} gas-phase species. The relation between the mole and mass fractions is reminded :

$$X_k W = Y_k W_k \tag{2.10}$$

The viscous stress tensor $\tau_{i,j}$ is given by the following relation :

$$\tau_{i,j} = \left(-\frac{1}{3}\mu\right)\frac{\partial u_l}{\partial x_l}\delta_{i,j} + \mu\left(\frac{\partial u_j}{\partial x_i} + \frac{\partial u_i}{\partial x_j}\right) \tag{2.11}$$

where $\delta_{i,j}$ is the Kronecker symbol ($\delta_{i,j} = 1$ if $i = j$, else $\delta_{i,j} = 0$), μ is the dynamic viscosity (related to the kinematic viscosity using $\nu = \mu/\rho$). Dynamic viscosity is assumed to be independent of the gas composition so that only temperature dependence is considered through the power law.

The heat flux q_i involved in the total non-chemical energy equation E, is given by :

$$q_i = \underbrace{-\lambda\frac{\partial T}{\partial x_i}}_{\text{Fourier term}} + \underbrace{\rho\sum_{k\in\Omega_G} h_{s,k}Y_k V_{k,i}}_{\text{heat diffusion due to molecular multi-species transport}} \tag{2.12}$$

In Eq. (2.12), two terms are involved in the expression of the heat flux: the *Fourier* flux which is the temperature diffusion by molecular effect and the multi-species term of molecular diffusion that characterizes the species sensible enthalpy transport by its diffusion velocity. λ stands for the thermal diffusion coefficient and is determined using :$\lambda = \mu C_p/P_r$.

General comment on the multi-species variables

The presented variables expressing the conservation of mass, momentum, energy and heat for multi-species fluids are subjected to the following constraints :

$$\sum_{k\in\Omega_G} Y_k = \sum_{k\in\Omega_G} X_k = 1 \tag{2.13}$$

$$\sum_{k\in\Omega_G} \dot{\omega}_k = 0 \tag{2.14}$$

$$\sum_{k\in\Omega_G} \rho Y_k V_{k,i} = 0 \tag{2.15}$$

The above expressions consist in constraints of mass conservation which need to be satisfied in order to ensure mass conservation during the numerical resolution of the conservation equations.

2.1.2 Modeling the multi-species transport terms

Note: in this Section, a vector notation is used

A proper approach to determine the diffusion velocity $V_{k,i}$ involved in the L.H.S of Eq. (2.2) would consist of the inversion of the system of *Williams* [29]. However, this is a very costly task as the system has to be solved in each direction and at each instant. The *Hirschfelder and Curtiss* approximation is thereby preferred as it provides an explicit expression of the diffusion velocity [30] :

$$\vec{V}_k X_k = -D_k \vec{\nabla} X_k \tag{2.16}$$

where D_k is an equivalent diffusion coefficient. Using the expression of Eq. 2.10, Eq.(2.16) can be expressed in terms of mass fraction :

$$\vec{V}_k Y_k = -D_k \frac{W_k}{W} \vec{\nabla} X_k \tag{2.17}$$

As exact expressions of diffusion velocities are not used, the *Hirschfelder and Curtiss* approximation does not necessary satisfy mass conservation $\sum_{k\in\Omega_G} Y_k V_{k,i} = 0$. To overcome this issue, a correction velocity is introduced in the expression of the diffusion velocity (Eq.(2.17)) so that the compatibility of species and mass conservation equation is ensured :

$$\vec{V}_k = -D_k \frac{\vec{\nabla} X_k}{X_k} + \vec{V}^{correc} \tag{2.18}$$

The expression of the correction velocity $\vec{V}^{correc}$ is obtained by introducing the expression in Eq.(2.18) in the species conservation equation given in Eq.(2.2) and summing all over the gas-phase species :

$$\vec{V}^{correc} = \sum_{k \in \Omega_G} D_k \frac{W_k}{W} \vec{\nabla} X_k \tag{2.19}$$

The relation between the mole fraction gradients and their mass fraction counterparts reads :

$$\vec{\nabla} X_k = \frac{W}{W_k} \vec{\nabla} Y_k - \frac{W^2}{W_k} Y_k \sum_{l \in \Omega_G} \frac{1}{W_l} \vec{\nabla} Y_l \tag{2.20}$$

Eventually, knowing the expression of the correction velocity and the mole fraction gradient expressions given by Eqs.(2.19)-(2.20), the diffusive mass flux $\vec{J_k}$ reads :

$$\vec{J_k} = \rho \vec{V_k} Y_k = \rho \left(-Dk \frac{W_k}{W} \vec{\nabla} X_k + Y_k \vec{V}^{correc} \right) \tag{2.21}$$

D_k is determined using a simple model by introducing the Schmidt Sc_k numbers which is considered to be constant in time and space $D_k = \mu / \rho Sc_k$.

2.1.3 Gas-phase kinetics equations

A chemical system of N_g species reacting through R gas phase reactions is considered as follows:

$$\sum_{k \in \Omega_G} \nu^f_{k,r} \mathcal{M}_k \rightleftharpoons \sum_{k \in \Omega G} \nu^b_{k,r} \mathcal{M}_k \quad \text{for r =1,R} \tag{2.22}$$

where $\mathcal{M}_k$ is the chemical symbol of the k^{th} species, $\nu^f_{k,r}$ and $\nu^b_{k,r}$ respectively stand for the stoichiometric coefficients of the k^{th} species in the r^{th} reaction. $\dot{\omega}_k$ is the mass rate of production or consumption of the k^{th} species in the r^{th} reaction :

$$\dot{\omega}_k = W_k \sum_{r=1}^{R} (\nu^b_{k,r} - \nu^f_{k,r}) \mathcal{Q}_r \tag{2.23}$$

where $\mathcal{Q}_r$ is the mole progress rate of the r^{th} reaction given by :

$$\mathcal{Q}_r = C^g_M \left(k^f_r \prod_{k \in \Omega_G} (C^g_k)^{\nu^f_{k,r}} - k^b_r \prod_{k \in \Omega_G} (C^g_k)^{\nu^b_{k,r}} \right) \tag{2.24}$$

where $C_k^g = \rho Y_k / W_k$ is the mole concentration of the k^{th} gas-phase species. Regarding third-body reactions[1], $C_M^g = \sum_{k \in \Omega_G} \alpha_{k,r} C_k^g$ is the equivalent mole concentration of the third-body M. $\alpha_{k,r}$ is defined as the efficiency of the k^{th} species in the r^{th} reaction. $C_M^g = 1$ for reactions that do not involve a third body. k_r^f and k_r^b respectively denote for the forward and reverse rate constants of the r^{th} reaction. The forward rate constant is modeled using the Arrhenius law as follows:

$$k_r^f = A_r T^{\beta_r} exp\left(\frac{-Ea_r}{RT}\right) \tag{2.25}$$

where A_r is the pre-exponential constant, β_r is the temperature exponent and Ea_r is the activation energy of the r^{th} reaction. The reverse constant is evaluated using the the equilibrium constant K_r^{eq}, $k_r^b = k_r^f / K_r^{eq}$. K_r^{eq} is determined using [31] :

$$K_r^{eq} = \left(\frac{p_{atm}}{RT}\right)^{\sum_{k \in \Omega_G} (\nu_{k,r}^b - \nu_{k,f}^f)} exp\left(\frac{\Delta S_0^r}{R} - \frac{\Delta H_0^r}{RT}\right) \tag{2.26}$$

where p_{atm} is the atmospheric pressure, ΔS_0^r and ΔH_0^r are the entropy and enthalpy of the r^{th} reaction at a reference thermodynamic state. The gas phase heat release rate reads :

$$\dot{\omega}_T = - \sum_{k \in \Omega_G} \triangle h_{f,k}^o \dot{\omega}_k \tag{2.27}$$

where $\triangle h_{f,k}^o$ is the enthalpy of formation of the k^{th} species.

2.2 Resolution of the transport equations and gas-phase chemistry

2.2.1 General features of the AVBP code

The AVBP code [32] solves the time-dependent compressible Navier-Stokes equations for multi-species reactive flows in two and three space dimensions. It uses a *cell-vertex* finite-volume (FV) method for numerical discretization and it is based on a unstructured and hybrid grid approach.

[1] Chemical reactions for which the reaction rate depend on the surrounding species in the mixture. The third body M is involved in both sides of the reaction,i,e. in the reagents and products). It has a kinetic impact but is not chemically involved

In the case of *cell-vertex* methods, variables are stored at the cell vertices or grid nodes whereas the control volume is delimited by the cells of the primal mesh as shown in Figure 2.1. In other words, the grid nodes do not represent the center of the control volume as for the *cell-centered* or *vertex-centered* methods. The *cell-vertex* method is attractive as it is compatible with finite-element (FE) type methods which enables a flexible use of both FV and FE numerical schemes.

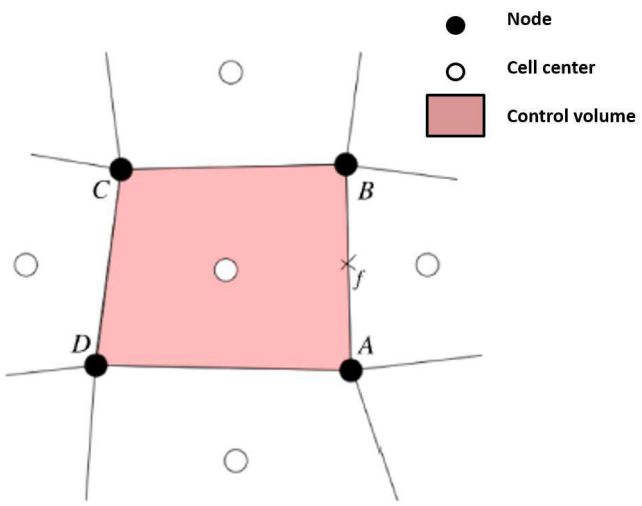

FIGURE 2.1: Two-dimensional schematic of a *cell-vertex* method. The control volume is delimited by the nodes of the mesh. The fluxes f are integrated along the cell edges (or faces in 3D) delimited by the grid nodes. This Figure is taken from the Ph.D report of N. Lamarque[7]

Different numerical schemes are available in the AVBP code and the two schemes that were used in the present thesis are listed as follows :

- *Lax-Wendroff (LW) scheme*: It is an adapted version of the LW scheme [33–35] to the *cell-vertex* method. This numerical scheme is two-order in time and space and centered. The second order is reached using a single time integration step.
- *Galerkin Runge-Kutta scheme* : finite element numerical schemes that are more accurate in time and space as they are of fourth-order. The time integration is performed using a 3-step Runger-Kutta time stepping.

2.2.2 Numerical resolution of gas-phase chemistry

Gas-phase chemistry is represented by the volumetric source term $\dot{\omega}_k$ in the R.H.S of Eq. (2.2). The latter is either integrated directly, i.e. integrated in the same time and with the same method as transport

terms or solved independently of the diffusive and convective terms according to an operator-splitting technique [36] as will be explained in Subsection 2.2.2.2. The heat release due to gas-phase reactions is always taken into account explicitly, i.e. no splitting is performed concerning energy. Only Gas-phase species source terms are concerned. $\dot{\omega}_T$ is calculated as shown in Eq. (2.27) once $\dot{\omega}_k$ is obtained.

2.2.2.1 Explicit direct resolution

The explicit direct resolution means that the volumetric source term $\dot{\omega}_k$ in the R.H.S of Eq. (2.2) is first calculated as in Eq. (2.23) at every iteration and added explicitly which means that a temporal integration is performed including transport process as follows :

$$\rho Y_k^{n+1} = \rho Y_k^n + dt_{min} \left[R_k^{conv} + R_k^{diff} + R_k^{chem} \right] \tag{2.28}$$

where dt_{min} is the minimum time step of the integration, R_k^{conv} and R_k^{diff} are respectively the operators expressing the rates of change of Y_k due to convective and diffusive transport. R_k^{chem} is the operator giving the rate of change due to gas-phase chemical reactions. It implies that the inclusion of the gas-phase chemical source term $\dot{\omega}_k$ is performed at the same time as the diffusive and convective terms. No assumptions are made regarding the differences between the chemical, diffusive and convective timescales. If the gas-phase chemical kinetics are stiff , the explicit integration might undergo numerical instabilities especially if the time step is not small enough. The numerical time step could be decreased but this is likely to yield undesirable CPU times.

2.2.2.2 Operator-splitting technique

The alternative to the direct integration method is to isolate chemistry resolution and tackle it with a dedicated solver. In this thesis, the AVBP code was coupled with the kinetic solver CLOE developed and owned by IFPEN. This approach that consists of separating chemistry from the diffusive and convective transport processes in Eq. (2.2) is called the Operator-Splitting technique [36]. As a result, the transport equation for gas-phase species mass fractions Eq. (2.2) can be expressed in the following form :

$$\forall \ k \in \Omega_G : \frac{\partial \rho Y_k}{\partial t} = R_k^{chem}(t) + R_k^{conv}(t) + R_k^{diff}(t) \tag{2.29}$$

In order to solve Eq.(2.29), chemical reactions are separated from convective and diffusive transport and a the integration of chemistry is performed with respect to the steps described in Figure 2.2 :

- Step 1: the vector $\vec{\psi}$ that includes the gas-phase species and temperature is defined as shown in Eq. 2.30. The index hom refers to homogeneous which indicates that the variable solely undergoes chemical reactions independently of transport.

$$\psi_i = \begin{pmatrix} \psi_1 \\ . \\ . \\ . \\ \psi_{N_g} \\ \psi_{N_g+1} \end{pmatrix} = \begin{pmatrix} \rho Y_1^{hom} \\ . \\ . \\ . \\ \rho Y_{N_g}^{hom} \\ T^{hom} \end{pmatrix} \tag{2.30}$$

- Step 2: at each time step and every node of the mesh, the i^{th} component of $\psi_i(t)$ is sent to the kinetic solver CLOE to solve the system of Eq. (2.31), where R_i^{chem} is the i^{th} component of the chemical operator that includes the chemical source terms:

$$\begin{cases} \vec{\psi} = \left(\rho Y_1^{hom}, ..., \rho Y_k^{hom}, ..., \rho Y_{N_g}^{hom}, T^{hom}\right) \\ \dfrac{\partial \psi_i}{\partial t} = R_i^{chem}(t) \quad \forall i = [1, .., N_g + 1] \end{cases} \tag{2.31}$$

- Step 3: Once the integration over a time step corresponding to dt_{min} is achieved, the solution $\psi_i(t + dt_{min})$ is returned to the CFD code AVBP.

- Step 4: $Y_k^{hom}\,(t + dt_{min})$ is used to estimate the chemical source term $\dot{\omega}_k$ of Eq. (2.2) in the following way :

$$\dot{\omega}_k = \frac{\left(\rho Y_k^{hom}\,(t + dt_{min}) - \rho Y_k\,(t)\right)}{dt_{min}} \tag{2.32}$$

- Step 5: finally, R_k^{chem} is replaced in Eq. (2.29) using the expression of Eq. (2.32). The time integration over a time step dt_{min} expressed in Eq. (2.28) becomes :

$$\rho Y_k\,(t + dt_{min}) = \rho Y_k^{hom}\,(t + dt_{min}) + (dt_{min})\left(R_k^{conv} + R_k^{diff}\right) \tag{2.33}$$

Note here that the chemical operator R_k^{chem} does not include any spatial discretization as convective and diffusive operators would do. In other words, chemistry is a local process for each grid node. As a result, Eq. (2.31) corresponds to an N_n independent ODE systems comprising $N_g + 1$ unknowns where N_n is the number of mesh nodes. Figure 2.3 provides a physical view of the operator-splitting technique. It

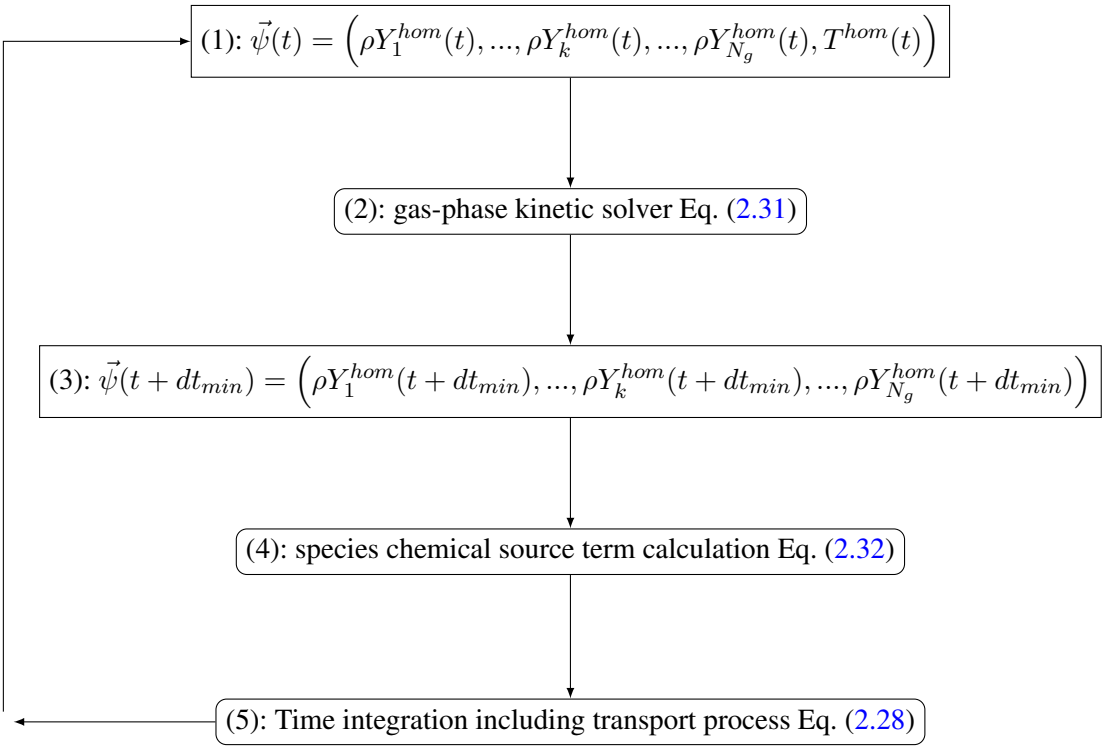

FIGURE 2.2: Coupling AVBP with the gas-phase kinetic solver CLOE

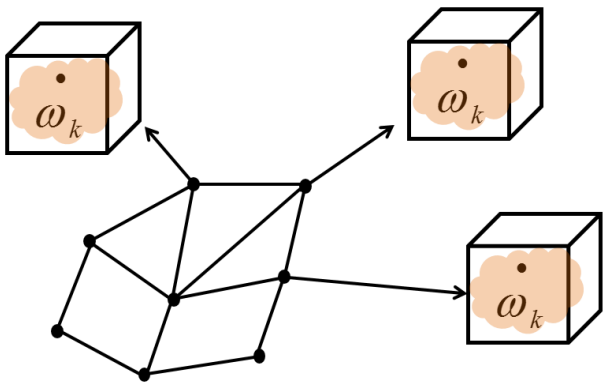

FIGURE 2.3: Physical view of the operator-splitting method

shows that physically speaking, each computational node of the mesh could be seen as an independent homogeneous reactor governed by the ODE system of Eq. (2.31). The governing equations of the homogeneous reactors depend on the numerical solver used for kinetics resolution.

Different numerical solvers are available in the kinetic solver CLOE :

- DDASPK [37]
- DASAC [38]
- LSODAR [39]
- DVODE [40]
- First order Euler method with sub-cycling (adapting time step)

Although the temperature is evaluated by the CFD code by transporting the total non-chemical energy, the homogeneous reactor ODE includes the temperature equation in order to update the temperature value at every sub-iteration in the case of implicit solvers such DVODE or DASAC. A proper resolution is thereby ensured. This results in a system having a size of $N_g + 1$:

$$\begin{cases} \vec{\psi} = \left(\rho Y_1^{hom}, ..., \rho Y_k^{hom}, ..., \rho Y_{N_g}^{hom}, T^{hom}\right) \\ \dfrac{\partial \rho Y_k^{hom}}{\partial t} = R_k^{chem}(t) = \dot{\omega}_k \quad \forall k \in \Omega_G \\ \dfrac{\partial T^{hom}}{\partial t} = R_{N_g+1}^{chem}(t) = -\dfrac{\sum\limits_k h_k \dot{\omega}_k^{hom}}{\rho c_p} \quad \forall k \in \Omega_G \end{cases} \tag{2.34}$$

where $\dot{\omega}_k^{hom}$ is the chemical source term determined by the kinetic solver. Here, the presented energy equation is enthalpy based as constant pressure assumption is made. If a constant volume equation is considered, an internal energy based equations is used. These assumptions are made in order to decouple chemical reactions and convection. The exact approach would consist in a generic formulation by accounting for both pressure and volume variations.

It is stressed that, if the numerical method used by the kinetic solvers does not involve any time sub-stepping or iterative methods such as for first order Euler explicit method, temperature equation is not required. Hence the system size can be reduced to N_g instead of $N_g + 1$ thus becoming.

$$\begin{cases} \vec{\psi} = \left(\rho Y_1^{hom}, ..., \rho Y_k^{hom}, ..., \rho Y_{N_g}^{hom}\right) \\ \dfrac{\partial \rho Y_k^{hom}}{\partial t} = R_k^{chem}(t) = \dot{\omega}_k^{hom} \quad \forall k \in \Omega_G \end{cases} \tag{2.35}$$

2.2.3 Limiting the time step by gas-phase chemistry

In order to ensure that the time variations related to all the physical and chemical phenomena involved are numerically captured, the limitation of the integration time step dt_{min} by gas-phase reactions might be required according to the use of the explicit direct integration method (Section 2.2.2.1) or the operator-splitting technique (Section 2.2.2.2):

- If the explicit direct integration method is used then the time step related to gas-phase chemistry dt_{chem}^{Gas} is estimated using the chemical source terms as follows:

$$dt_{chem}^{Gas} = min\left[\frac{\rho}{\dot{\omega}_k}\right] \tag{2.36}$$

  The overall dt_{min} over which the integration of the governing equations is performed is determined as follows:

$$dt_{min} = min\left[dt_{CFL}, dt_{F_o}^{min}, dt_{chem}^{Gas}\right] \tag{2.37}$$

  where dt_{CFL} and $dt_{F_o}^{min}$ respectively stand for the acoustic and diffusion time steps.

- If the Operator-splitting technique is used then the limitation of the time step by gas-phase chemistry is not necessarily required. The integration of gas-phase chemistry could be performed using an implicit method (or explicit with sub-cycling) with an initial time step $dt_{min} = min\left[dt_{CFL},\ dt_{F_o}^{min}\right]$ which is used for the integration of transport.

- As the resolution of chemistry has a cost, the resolution of gas-phase chemistry is not strictly required at every time step weather the operator-splitting technique or the direct integration method is used. As a matter of fact, if gas-phase chemistry is not limiting and $\frac{dt_{chem}^{Gas}}{dt_{min}} > 10$ then the resolution of chemistry could be performed every n time steps where $n = \left[\frac{dt_{chem}^{Gas}}{dt_{min}}\right]$. The underlying assumption is that the gas-phase species mass fractions are considered constant for a physical time that is equal to $n \times dt_{min}$. It is stressed that this approach might save a considerable CPU time but is likely to induce numerical instabilities.

2.2.3.1 Verification of the chemistry resolution

In order to verify the inclusion of detailed gas phase chemistry into AVBP using the coupling with the kinetic solver CLOE, the resulting tool is applied to the simulation of a zero-dimensional heterogeneous

reactor. It is composed of one computational cell whose boundaries are all set to be adiabatic and free-slip, resulting in a simple closed volume reactor exclusively exhibiting gas phase reactions, but no molecular or convective transport. The numerical results are compared with the ones obtained with a reference kinetic solver SENKIN of the CHEMKIN library [41]. Table 2.1 shows the initial conditions of the homogeneous reactor computation. The description and the numerical resolution method of the gas-phase chemistry are presented as well.

Mixture	ϕ	p(t=0), T(t=0)	Kinetic scheme	Integration method
CH_4/Air	0.37	1 atm and 1365 K	Reduced Aramco Mech 1.3 [42, 43]	DVODE [40]

TABLE 2.1: Features of the homogeneous reactor computation. ϕ stands for the equivalence ratio. P(t=0) and T(t=0) are the initial pressure and temperature of the reactor.

The considered gas-phase chemistry is representative of the lean combustion of a CH_4/Air mixture. The kinetic mechanism used to describe the gas-phase chemistry is a reduced skeletal version of the Saudi Aramco mechanism 1.3 (Aramco Mech 1.3) [42] which involves 16 species and includes 39 bidirectional reactions and 1 unidirectional reaction. The implicit solver DVODE [40] is used for the present computation. Figure 2.4 shows the resulting time evolution of the species mass fractions and temperature. As 16 species are involved, only two of the major species (CH_4, O_2) and the hydroxyl radical OH are shown. Clearly, the time evolutions resulting from the present coupling (AVBP-CLOE) match very well the CHEMKIN results. This thereby verifies that the coupling with the kinetic solver properly ensures the resolution of gas-phase chemistry.

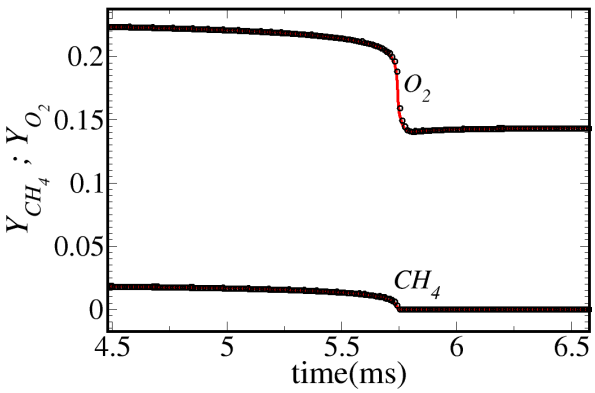

(A) CH_4 and O_2 mass fractions

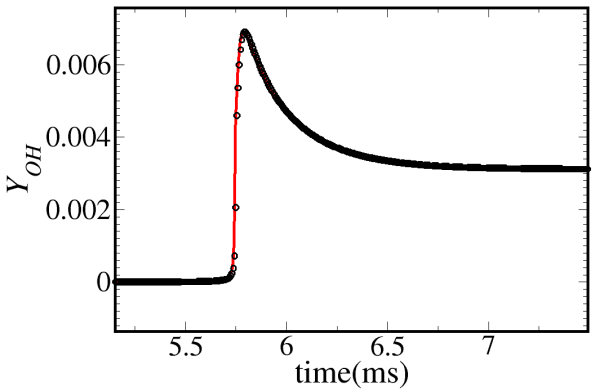

(B) OH mass fraction

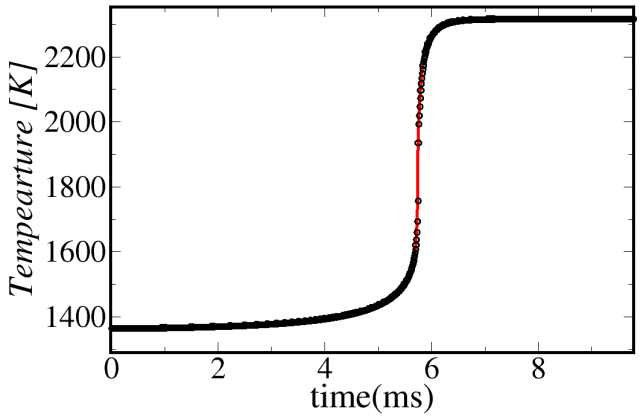

(C) Temperature

FIGURE 2.4: Time evolution of the gas-phase species and temperature. Lines: AVBP-CLOE. Symbols: CHEMKIN

Chapter 3

Accounting for surface kinetics in computational fluid dynamics

3.1 Formalism of surface reactions

3.1.1 Description of surface reactions and assumptions

This Section aims at illustrating the description of surface reactions occurring at a reactive wall that are addressed in this thesis. At this purpose, Figures 3.1 to 3.3 provide examples of the interaction between carbon monoxide CO and Platinum Pt. Figure 3.1 shows an example of a gas-phase carbon monoxide species noted $CO(g)$ diffusing near a support presenting Pt active site at its surface. As $CO(g)$ diffuses toward Pt, chemical bonds (represented by the red bond on the right side) are created thus yielding the formation of a new species noted $CO(s)$ highlighted by the red frame. This illustrates an adsorption reaction.

Figure 3.2 shows that the CO-adsorbate $CO(s)$ is returned to the gas-phase as the chemical bonds between CO and Pt are broken. This illustrates a desorption reaction which is the reciprocal of the adsorption reaction. Also, adsorbate species and active sites might interact as shown in Figure 3.3 where the interaction between $CO(S)$ and Pt leads to the formation of two type of surface species: $C(s)$ and $O(s)$. Only adsorbate and active sites are involved in these type of reactions. It is stressed that the backward reaction is possible which consists of the interaction between two surface species: $C(s) + O(s) \rightarrow CO(s) + Pt$.

Therefore, the three types of surface reactions that are considered in the present thesis are listed as follows:

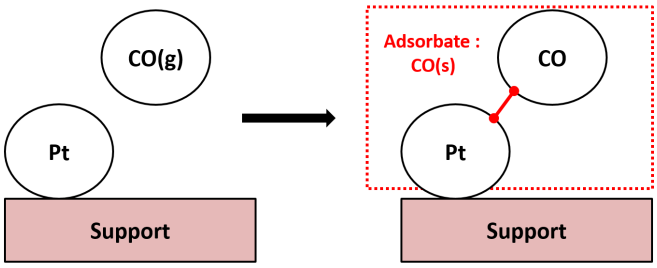

FIGURE 3.1: Schematic of the CO adsorption over Pt: $CO(g) + Pt \rightarrow CO(s)$

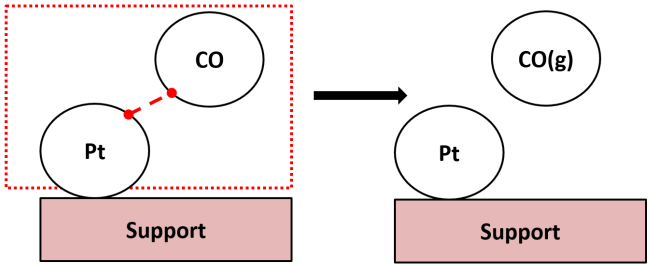

FIGURE 3.2: Schematic of the CO desorption reaction: $CO(s) \rightarrow CO(g) + Pt$

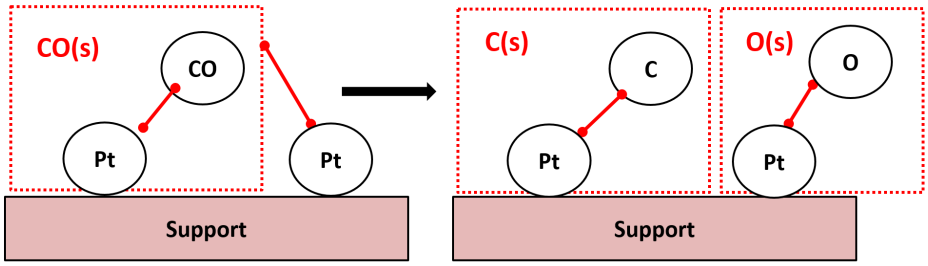

FIGURE 3.3: Interactions involving surface species: $CO(s) + Pt \rightarrow C(s) + O(s)$

- Adsorption reactions involving gas-phase and surface active sites
- Desorption reactions where adsorbed species are returned to the gas-phase
- Surface reactions involving surface species and active sites.

In the present study, surface reactions will be accounted for under the following assumptions:

- Only surface species that stand on the top layer of the reactive support are considered. This means that the bulk species that lie inside the porous network are not accounted for.

- The local molecular mass diffusion of surface species is considered to be very fast with respect to surface reactions so that the surface species concentration can be considered as locally homogeneous. This assumption is referred as the mean field approximation [44].

3.1.2 Set of equations of surface kinetics

A surface chemical system of N_g gas-phase species and N_s surface species reacting through R_s surface reactions is represented as follows :

$$\sum_{k\in\Omega_g} \nu_{k,r}^{s,f}\mathcal{M}_k + \sum_{k\in\Omega_s} \nu_{k,r}^{s,f}\mathcal{T}_k \rightleftharpoons \sum_{k\in\Omega_g} \nu_{k,r}^{s,b}\mathcal{M}_k + \sum_{k\in\Omega_s} \nu_{k,r}^{s,b}\mathcal{T}_k \tag{3.1}$$

where $\Omega_s = [1, N_s]$. $\mathcal{M}_k$ and $\mathcal{T}_k$ respectively stand for the chemical symbol of the k^{th} gas-phase and surface species. $\nu_{k,r}^{s,f}$ and $\nu_{k,r}^{s,b}$ respectively stand for the stoichiometric coefficients of the k^{th} gas-phase and surface species involved in the r^{th} surface reaction. $\dot{s}_k$ $(kg.m^{-2}.s^{-1})$ is the mass rate of production or consumption of the k^{th} gas-species or surface species in the r^{th} surface reaction :

$$\dot{s}_k = W_k \sum_{r=1}^{R_s} (\nu_{k,r}^{s,b} - \nu_{k,r}^{s,f})\mathcal{Q}_r^s \tag{3.2}$$

where $\mathcal{Q}_r^s$ is the mole progress rate of the r^{th} surface reaction given by:

$$\mathcal{Q}_r^s = \left(k_r^{s,f} \left(\prod_{k\in\Omega_G} (C_k^g)^{\nu_{k,r}^{s,f}} \right) \left(\prod_{k\in\Omega_s} (C_k^s)^{\nu_{k,r}^{s,f}} \right) \right) - \left(k_r^{s,b} \left(\prod_{k\in\Omega_G} (C_k^g)^{\nu_{k,r}^{s,b}} \right) \left(\prod_{k\in\Omega_s} (C_k^s)^{\nu_{k,r}^{s,b}} \right) \right) \tag{3.3}$$

In Eq. (3.3), both gas-phase species concentrations (C_k^g) and surface adsorbates or active sites concentrations (C_k^s) are involved. Whereas C_k^g is in $mol.m^{-3}$, $C_k^s = \Gamma\theta_k/W_k^s$ is the surface mole concentration of the k^{th} surface species whose units are in $mol.m^{-2}$. The different variables involved in the definition of C_k^s are explained as follows:

- W_k^s is the molecular weight of the k^{th} surface species or active site.

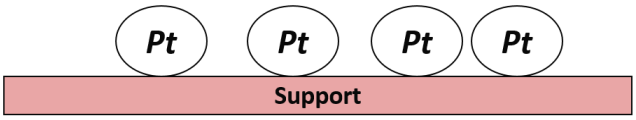

FIGURE 3.4: Illustration of the site density of a Pt active site

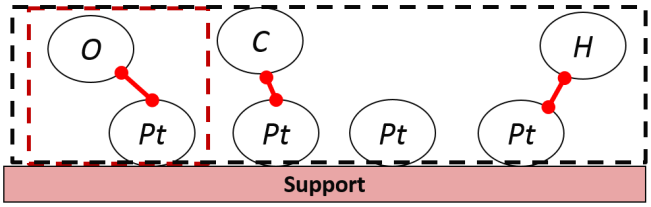

FIGURE 3.5: Illustration of an adsorbate site fraction

- Figure 3.4 shows an example of a support over which active sites of platinum Pt are laid. The site density Γ $(mol \cdot m^{-2})$ refers to the number of moles of active sites per surface unit of the support. In this thesis, Γ is supposed to remain constant.

- θ_k is the site fraction which represents the mole ratio between the k^{th} surface species and the total number of adsorbates and void active sites. Figure 3.5 shows an example of a support over which different adsorbates ($O(Pt)$, $C(PT)$ and $H(Pt)$) and void active sites (Pt) are laid. The site fraction of the adsorbate $O(Pt)$ referred as θ_O is the ratio between the number of moles of the adsorbate $O(Pt)$ highlighted by the red box and the total number of moles of the adsorbates and Pt void site highlighted by the black box.

- $k_r^{s,f}$ and $k_r^{s,b}$ respectively denote for the forward and reverse rate constants of the r^{th} surface reaction. The forward rate constant is modeled using the Arrhenius law as follows:

$$k_r^{s,f} = A_r^{s,cov} T_w^{\beta_r^s} exp\left(\frac{-Ea_r^{s,cov}}{RT_w}\right) \tag{3.4}$$

where T_w is the reactive wall temperature and β_r^s is the wall temperature exponent. $A_r^{s,cov}$ and $E_r^{s,cov}$ are respectively the coverage dependent pre-exponential factor and activation energy of the r^{th} surface reaction that can be written as follows:

$$ln(A_r^{s,cov}) = ln(A_r^s) + \sum_{k \in \Omega_s} \eta_{k,r} \theta_k \tag{3.5}$$

and

$$Ea_r^{s,cov} = Ea_r^s + \sum_{k \in \Omega_s} \varepsilon_{k,r} \theta_k \tag{3.6}$$

where A_r^s and Ea_r^s are the pre-exponential and activation energy at zero coverage. $\eta_{k,r}$ and $\varepsilon_{k,r}$ are kinetic coefficients accounting for the coverage of the surface. $k_r^{s,b}$ is determined using the equilibrium constant $K_r^{s,eq} = k_r^{s,b}/k_r^{s,f}$.

Assuming the adsorption to be activated, the parameters β_r^s, $E_r^{s,cov}$ and $A_r^{s,cov}$ become [44–46] :

$$\beta_r^s = \frac{1}{2}, \;\; E_r^{s,cov} = 0, \;\; A_r^{s,cov} = \left(\frac{\gamma_r}{\Gamma^m}\right) \sqrt{\frac{R}{2\pi W_{ads}^s}} \tag{3.7}$$

where γ_r is the sticking factor of the adsorption reaction, σ_k is the number of sites that each adsorbed species occupies, m corresponds to the number of surface species involved in the surface reaction and W_{ads}^s is the molecular weight of the gas-phase adsorbed species.

With respect to the assumptions made in this study, the evolution equation describing the variation of the surface species site fraction is shown in Eq. 3.8 [22] :

$$\frac{\partial \theta_k}{\partial t} = \frac{\dot{s}_k}{\Gamma W_k} \;\; \forall \;\; k \;\; \in \;\; \Omega_s \tag{3.8}$$

3.2 Derivation of the boundary conditions for momentum, species and energy

In this Section, the approach resulting in the mass and energy balance at the reactive interface is detailed. The expressions of the momentum, mass and energy wall fluxes are then derived from the interface balances. The mass balance allows to obtain the expression of the *Stefan* velocity and the gas-phase species normal gradients accounting for surface reactions whereas the energy balance gives the normal heat flux at the reactive boundary. Flux balances at the reactive interface are obtained by integrating the transport equations over the control volume sketched in Figure. 3.6:

g is the index standing for gas-phase scalars whereas s stands for solid-phase scalars. w is the index standing for variables at the wall, $\vec{n^g}$ is the vector normal to the interface and directed toward the gas-phase, $\vec{n^s}$ is vector normal to the interface and directed toward the solid, S is the elementary reactive

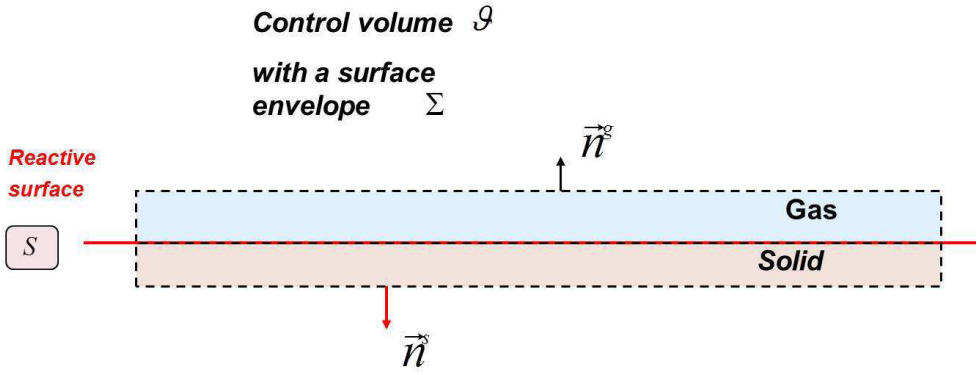

FIGURE 3.6: sketch of the control volume at the reactive interface

surface which refers to the interface, $\mathcal{V}$ refers to the control volume and Σ stands for the surface envelope of the control volume.

3.2.1 Mass balance

The balance is obtained as follows : The species conservation Eq. (2.2) is integrated over the control volume $\mathcal{V}$ [31, 44]

$$\int_{\mathcal{V}} \left(\frac{\partial \rho Y_k}{\partial t} + \nabla \cdot (\rho \vec{u} Y_k) \right) d\mathcal{V} = \int_{\mathcal{V}} \left(-\nabla \cdot \left(\rho \vec{V}_k Y_k \right) + \dot{\omega}_k \right) d\mathcal{V} \tag{3.9}$$

Applying the *Green-Ostrogradski* theorem one obtains:

$$\int_{\mathcal{V}} \left(\frac{\partial \rho Y_k}{\partial t} \right) d\mathcal{V} + \int_{\mathcal{V}} -\dot{\omega}_k d\mathcal{V} = \int_{\Sigma} \left(- \left(\rho \vec{V}_k Y_k \right) \cdot \vec{n} \right) d\Sigma + \int_{\Sigma} - \left(\rho Y_k \vec{u} \cdot \vec{n} \right) d\Sigma \tag{3.10}$$

Eq. (3.10) represents the integral form of the transport equation given in Eq. (2.2). If the volume tends to zero ($\mathcal{V} \to 0$), the control volume surface Σ tends to the reactive interface S ($\Sigma \to S$) [31]. As the volume tends to zero, no mass accumulation occurs. The first term of Eq. (3.10) becomes :

$$\lim_{\mathcal{V} \to 0} \int_{\mathcal{V}} \left(\frac{\partial \rho Y_k}{\partial t} \right) d\mathcal{V} = 0 \tag{3.11}$$

The gas-phase production rates is decomposed into two terms, the first is non-zero in the gas-phase and null at the wall whereas the second one equals zero in the gas-phase and non-zero at the interface:

$$\dot{\omega}_k = \dot{\omega}'_k + \dot{s}_k \delta(y) \tag{3.12}$$

where $\dot{\omega}'_k$ and $\dot{s}_k$ respectively represent the gas-phase and surface rate of production of the k^{th} species per unit area and :

$$\int_{-\infty}^{+\infty} \delta(y)\, dy = 1 \tag{3.13}$$

As the volume tends to zero, one can write :

$$\lim_{\mathcal{V}\to 0} \int_{\mathcal{V}} \dot{\omega}'_k d\mathcal{V} = 0 \tag{3.14}$$

According to the *Dirac* function definitions above :

$$\lim_{\mathcal{V}\to 0} \int_{\mathcal{V}} \dot{\omega}_k d\mathcal{V} = \int_S \dot{s}_k dS \tag{3.15}$$

Eventually, the volume integral of the L.H.S in Eq. (3.10) becomes :

$$\lim_{\mathcal{V}\to 0} \left(\int_{\mathcal{V}} \left(\frac{\partial \rho Y_k}{\partial t} \right) d\mathcal{V} + \int_{\mathcal{V}} -\dot{\omega}_k d\mathcal{V} \right) = -\int_S \dot{s}_k dS \tag{3.16}$$

As convection and diffusion are not present in the solid wall and the boundary of the control volume is static $\left(\vec{J_k}^{\,s} = \vec{u^s} = \vec{0}\right)$, one obtains :

$$\begin{aligned} \lim_{\Sigma\to S} \left(\int_{\Sigma} \left(-\left(\rho \vec{V}_k Y_k \right) \cdot \vec{n} \right) d\Sigma + \int_{\Sigma} \left(\rho Y_k \left(-\vec{u} \right) \cdot \vec{n} \right) d\Sigma \right) &= \int_S \left(-\left(\rho_w^g \vec{V}_{k,w}^{\,g} Y_{k,w} \right) \cdot \vec{n}^g \right) dS \\ &+ \int_S \left(\rho_w^g Y_{k,w} \left(-\vec{u}^g \right) \cdot \vec{n}^g \right) dS \end{aligned} \tag{3.17}$$

As a result, Eqs.(3.16, 3.17) give :

$$\underbrace{-\int_S \dot{s}_k dS}_{\text{rate of production by surface reaction}} = \underbrace{-\int_S \left(\rho_w^g \vec{V}_{k,w}^g Y_{k,w}\right) \cdot \vec{n}^g dS}_{\text{Mass flux diffusion}} + \underbrace{\int_S \rho_w^g Y_{k,w} \left(-\vec{u}^g \cdot \vec{n}^g\right) dS}_{\text{Mass flux convection}} \tag{3.18}$$

Where :

$$\begin{cases} \vec{V}_{k,w}^g \cdot \vec{n}^g = V_{k,n,w} \\ \vec{u} \cdot \vec{n}^g = U_{Stefan} \end{cases} \tag{3.19}$$

The mass balance at the reactive interface (Eq. (3.18)) reads then :

$$(\rho_w V_{k,n,w} Y_{k,w}) + (\rho_w U_{Stefan} Y_{k,w}) = \dot{s}_k \tag{3.20}$$

It is stressed that Eq. (3.20) is consistent with the mass balance near a reactive wall in [17, 25, 44, 47]. Summing Eq. (3.20) over all the gas-phase species and considering the mass conservation, an expression for the wall-normal *Stefan* velocity is obtained:

$$U_{Stefan} = \frac{1}{\rho_w} \left(\sum_{k \in \Omega_G} \dot{s}_k \right) \tag{3.21}$$

Here, the expression of the prescribed normal gradient of the gas-phase species is derived. First, let us first consider the mass balance at the interface given by Eq. (3.20) :

$$(\rho_w V_{k,n,w} Y_{k,w}) + (\rho_w U_{Stefan} Y_{k,w}) = \dot{s}_k \tag{3.22}$$

By isolating the species diffusion flux, one obtains :

$$(\rho_w V_{k,n,w} Y_{k,w}) = \dot{s}_k - (\rho_w U_{Stefan} Y_{k,w}) \tag{3.23}$$

The species mass flux is written as in Eq. (2.21) according to the *Hirschfelder & Curtiss* approximation :

$$J_{k,i} = \rho V_{k,i} Y_k = \rho \left(-Dk \frac{W_k}{W} \frac{\partial X_k}{\partial x_i} + Y_k V_i^{correc} \right) \tag{3.24}$$

By multiplying Eq. (3.24) by the interface normal $\vec{n}^g$, one obtains :

$$\vec{J}_{k,w} \cdot \vec{n}^g = \rho_w \vec{V}_{k,w} \cdot \vec{n}^g Y_{k,w} = -\rho_w \left(-Dk \frac{W_k}{W_w} \vec{\nabla} X_{k,w} \cdot \vec{n}^g - Y_{k,w} \vec{V}_w^{correc} \cdot \vec{n}^g \right) \tag{3.25}$$

with $\vec{V}_w^{correc} \cdot \vec{n}^g$ and $\vec{\nabla} X_{k,w} \cdot \vec{n}^g$ corresponding respectively to the wall-orthogonal correction velocity and species molar fractions expressed as in Eqs. (3.26, 3.27) :

$$\vec{V}_w^{correc} \cdot \vec{n}^g = \sum_{k \in \Omega_G} D_k \frac{W_k}{W_w} \vec{\nabla} X_{k,w} \cdot \vec{n}^g \tag{3.26}$$

$$\vec{\nabla} X_{k,w} \cdot \vec{n}^g = \frac{W_w}{W_k} \vec{\nabla} Y_{k,w} \cdot \vec{n}^g - \frac{W_w^2}{W_k} Y_{k,w} \sum_{l \in \Omega_G} \frac{1}{W_l} \vec{\nabla} Y_{l,w} \cdot \vec{n}^g \tag{3.27}$$

Making use of Eq. (3.27) and inserting Eqs. (3.21, 3.26, 3.25) into the mass balance at the interface given by Eq. (3.23), it becomes possible to relate the species mass fraction at the wall $Y_{k,w}$ to its normal gradient at the boundary surface by isolating the latter [24, 25]:

$$\vec{\nabla} Y_{k,w}^{BC} \cdot \vec{n}^g = \frac{Y_{k,w}}{D_k \rho_w} \sum_{l \in \Omega_G} \dot{s}_l + \frac{Y_{k,w}}{D_k} \vec{V}_w^{correc} \cdot \vec{n}^g + Y_{k,w} W_w \left(\sum_{l \in \Omega_{gas}} \frac{1}{W_l} \vec{\nabla} Y_{k,w} \cdot \vec{n}^g \right) - \frac{\dot{s}_k}{\rho_w D_k} \tag{3.28}$$

3.2.2 Energy balance

An energy balance at the reactive interface is now derived in order to prescribe the proper temperature gradient at the wall in the presence of surface reactions. In order to properly represent the interplay between surface reactions and gas-phase temperature, a specific boundary condition is derived from the energy balance at the reactive interface. A similar approach as the one used for the mass balance is applied to the total non-chemical energy given in Eq. (2.4) :

$$\frac{\partial \rho E}{\partial t} + \nabla \cdot (\rho E \vec{u}) = \dot{\omega}_T + \nabla \cdot (-\vec{q} + \bar{\bar{\sigma}} \vec{u}) \tag{3.29}$$

By integrating over the control volume, one obtains :

$$\int_{\mathcal{V}} \left(\frac{\partial \rho E}{\partial t} + \nabla \cdot (\rho \vec{u} E) \right) d\mathcal{V} = \int_{\mathcal{V}} \left(\nabla \cdot (\bar{\bar{\sigma}} \vec{u} - \vec{q}) + \dot{\omega}_T \right) d\mathcal{V} \tag{3.30}$$

By Applying the *Green-Ostrogradski* theorem, Eq. (3.30) becomes:

$$\int_{\mathcal{V}} \left(\frac{\partial \rho E}{\partial t} \right) d\mathcal{V} + \int_{\mathcal{V}} -\dot{\omega}_T d\mathcal{V} = \int_{\Sigma} \left((\bar{\bar{\sigma}} \vec{u} - \vec{q}) \cdot \vec{n} \right) d\Sigma + \int_{\Sigma} \left(-\rho E \vec{u} \cdot \vec{n} \right) d\Sigma \tag{3.31}$$

Eq. (3.31) represents the integral form of the transport equation given in Eq. (2.4). If the volume tends to zero ($\mathcal{V} \to 0$), the control volume surface Σ tends to the reactive interface S ($\Sigma \to S$) [31]. Eq. (3.31) becomes :

$$\lim_{\mathcal{V} \to 0} \left(\int_{\mathcal{V}} \frac{\partial \rho E}{\partial t} d\mathcal{V} + \int_{\mathcal{V}} -\dot{\omega}_T d\mathcal{V} \right) = \lim_{\Sigma \to S} \left(\int_{\Sigma} \left((\bar{\bar{\sigma}} \vec{u} - \vec{q}) \cdot \vec{n} \right) d\Sigma + \int_{\Sigma} \left(-\rho E \vec{u} \cdot \vec{n} \right) d\Sigma \right) \tag{3.32}$$

As the volume tends to zero, energy accumulation does not occur. Hence, the first term of Eq. (3.32) becomes :

$$\lim_{\mathcal{V} \to 0} \int_{\mathcal{V}} \left(\frac{\partial \rho E}{\partial t} \right) d\mathcal{V} = 0 \tag{3.33}$$

The gas-phase heat release can be decomposed into two terms as in Eq. (3.12):

$$\dot{\omega}_T = \dot{\omega}'_T + \dot{S}_T \delta(y) \tag{3.34}$$

When the volume tends to zero, one can write :

$$\lim_{\mathcal{V} \to 0} \int_{\mathcal{V}} \dot{\omega}'_T d\mathcal{V} = 0 \tag{3.35}$$

The volume integral of $\dot{\omega}_T$ becomes :

$$\lim_{\mathcal{V}\to 0}\left(\int_{\mathcal{V}} -\dot{\omega}_T d\mathcal{V}\right) = -\int_S \dot{S}_T dS \tag{3.36}$$

Eventually, the volume integral of the left hand-side in Eq. (3.31) becomes :

$$\lim_{\mathcal{V}\to 0}\left(\int_{\mathcal{V}} \left(\frac{\partial \rho E}{\partial t}\right) d\mathcal{V} + \int_{\mathcal{V}} -\dot{\omega}_T d\mathcal{V}\right) = -\int_S \dot{S}_T dS \tag{3.37}$$

Considering only thermal diffusion in the solid wall:

$$\begin{aligned}\lim_{\Sigma\to S}\left(\int_\Sigma \left(\left(\bar{\bar{\sigma}}\vec{u} - \vec{q}\right)\cdot\vec{n}\right) d\Sigma + \int_\Sigma \left(\rho E\left(-\vec{u}\right)\cdot\vec{n}\right) d\Sigma\right) &= \int_S \left(\left(\bar{\bar{\sigma}}^g_w \vec{u}^g_w - \vec{q}^g_w\right)\cdot\vec{n}^g\right) dS \\ &+ \int_S \left(\rho^g_w E^g_w\left(-\vec{u}^g_w\right)\cdot\vec{n}^g\right) dS \\ &+ \int_S \left(\left(-\vec{q}^s_w\right)\cdot\vec{n}^s\right) dS\end{aligned} \tag{3.38}$$

As a result, Eqs.(3.37,3.38) give :

$$\begin{aligned}\underbrace{-\int_S \dot{S}_T dS}_{\text{heat release due to surface reactions}} &= \underbrace{\int_S \left(\bar{\bar{\sigma}}^g_w \vec{u}^g_w\right)\cdot\vec{n}^g dS}_{\text{stress heat}} \underbrace{-\int_S \left(\vec{q}^g_w\right)\cdot\vec{n}^g dS}_{\text{heat flux diffusion}} \underbrace{+\int_S \rho^g_w E_w\left(-\vec{u}^g_w\cdot\vec{n^g}\right) dS}_{\text{total non-chemical energy convection}} \\ &+ \underbrace{\int_S \left(\vec{q}^s_w\right)\cdot\vec{n}^g dS}_{\text{heat diffusion in solid wall}}\end{aligned} \tag{3.39}$$

With the following notations :

$$\begin{cases}\left(\bar{\bar{\sigma}}^g_w \vec{u}^g_w - \vec{q}^g_w\right)\cdot\vec{n}^g = \left(\bar{\bar{\sigma}}^g\cdot\vec{u}^g\right)_{n,w} - q^g_{n,w} \\ \vec{u}_w\cdot\vec{n}^g = U_{Stefan} \\ \left(-\vec{q}^s_w\right)\cdot\vec{n}^g = q^s_{n,w}\end{cases} \tag{3.40}$$

The heat balance at the reactive interface becomes :

$$-\dot{S}_T = \left(\bar{\bar{\sigma}}^g \cdot \vec{u}^g\right)_{n,w} - q^g_{n,w} - \rho^g_w E_w U_{Stefan} + q^s_{n,w} \tag{3.41}$$

Diffusion of gas-phase species in the solid wall is neglected and the surface heat release is considered to result from both gas-phase and surface species. These assumptions result in the following expressions:

$$\begin{cases} q^s_{n,w} = -\lambda^s \vec{\nabla} T^s_w \cdot \vec{n}^g \\ \dot{S}_T = -\left(\sum\limits_{k\in\Omega_S} h_k \dot{s}_k + \sum\limits_{k\in\Omega_G} \triangle h^o_{f,k} \dot{s}_k \right) \end{cases} \tag{3.42}$$

By introducing the terms above into Eq. (3.41), and replacing E by its expression one obtains :

$$\begin{aligned} \left(\lambda^g \vec{\nabla} T^g_w - \lambda^s \vec{\nabla} T^s_w\right) \cdot \vec{n}^g = &+ \sum_{k\in\Omega_G} \left(\rho_w \left(h_{s,k,w} V_{k,n,w} Y_{k,w}\right) + \rho_w U_{Stefan} \left(h_{s,k,w} Y_{k,w}\right)\right) \\ &+ \left(\sum_{k\in\Omega_S} h_{k,w} \dot{s}_k + \sum_{k\in\Omega_G} \triangle h^o_f \dot{s}_k \right) \\ &- \left(\left(\bar{\bar{\sigma}}^g \vec{u^g}\right)_{n,w} + p U_{Stefan} \right) \\ &+ \frac{\dot{m}}{2} \sum_{j\in\mathcal{D}} u^2_{j,w} \end{aligned} \tag{3.43}$$

The first term in the R.H.S of Equation Eq. (3.43) can be simplified by considering the mass balance at the interface given in Eq. (3.20). Indeed, if Eq. (3.20) is multiplied by the species sensible enthalpy $h_{s,k}$ and sums all over the gas-phase species, the resulting balance becomes :

$$\sum_{k\in\Omega_G} \left(\rho_w \left(h_{s,k,w} V_{k,n,w} Y_{k,w}\right) + \rho_w U_{Stefan} \left(h_{s,k,w} Y_{k,w}\right)\right) = \sum_{k\in\Omega_G} h_{s,k,w} \dot{s}_k \tag{3.44}$$

As a result, the first and second terms in the R.H.S of equation Eq. (3.43) are simplified as follows :

$$\begin{aligned} \sum_{k\in\Omega_G} \left(\rho_w \left(h_{s,k,w} V_{k,n,w} Y_{k,w}\right) + \rho_w U_{Stefan} \left(h_{s,k,w} Y_{k,w}\right)\right) + \left(\sum_{k\in\Omega_S} h_{k,w} \dot{s}_k + \sum_{k\in\Omega_G} \triangle h^o_f \dot{s}_k \right) \\ = \sum_{k\in\{\Omega_G\cup\Omega_S\}} h_{k,w} \dot{s}_k \end{aligned} \tag{3.45}$$

and the third term becomes :

$$\left(\left(\bar{\bar{\sigma}}^g\vec{u}^g\right)_{n,w} + pU_{Stefan}\right) = \left(\left(\bar{\bar{\sigma}}^g\vec{u}^g\right)_{n,w} + p\vec{u}^g\cdot\vec{n}^g\right) = \left(\bar{\bar{\tau}}^g\vec{u}^g\right)_{n,w} \tag{3.46}$$

Finally, injecting Eqs. (3.45, 3.46) into Eq. (3.43) and isolating the gas-phase wall-normal thermal diffusion flux yields :

$$\lambda^g\vec{\nabla}T_w^g\cdot\vec{n}^g = \sum_{k\in\{\Omega_G\cup\Omega_S\}} h_{k,w}\dot{s}_k - \left(\bar{\bar{\tau}}^g\vec{u}^g\right)_{n,w} + \frac{\dot{m}}{2}\sum_{j\in\mathcal{D}} u_{j,w}^2 + \lambda^s\vec{\nabla}T_w^s\cdot\vec{n}^g \tag{3.47}$$

Eq. (3.47) corresponds to the heat flux balance that accounts for the effect of surface chemistry. The balance enables to prescribe the proper heat flux at the boundary $\vec{q_w}^{BC}\cdot\vec{n}^g$ by isolating in Eq. (3.47) the heat flux q_j given in Eq. (2.12). Under the *Hirschfelder & Curtiss* approximation $\vec{q_w}^{BC}\cdot\vec{n}^g$ reads :

$$\begin{aligned}\vec{q}_w^{BC}\cdot\vec{n}^g = & \underbrace{-\sum_{k\in\Omega_S} h_k\dot{s}_k}_{\text{Surface heat release due to surface species}} - \underbrace{\sum_{k\in\Omega_G}\triangle h_f^o\dot{s}_k}_{\text{surface heat release due to gas-phase species}} \\ & - \underbrace{\rho_w\sum_{k\in\Omega_G} U_{Stefan}h_{s,k,w}Y_{k,w}}_{\text{sensible enthalpy transport by Stefan flux}} - \underbrace{\frac{\dot{m}}{2}\sum_{j\in\mathcal{D}} u_{j,w}^2}_{\text{Kinetic energy}} + \underbrace{\left(\bar{\bar{\tau}}^g\vec{u^g}\right)_{n,w}}_{\text{viscous heat}} - \underbrace{\lambda^s\vec{\nabla}T_w^s\cdot\vec{n}^g}_{\text{heat conduction in solid wall}}\end{aligned} \tag{3.48}$$

It is stressed that a special attention was given to the derivation to obtain a generic formulation that would allow the simulation of adiabatic and chemically inert walls is surface reaction rates tend to zero and if the heat conduction in the solid is neglected.

3.3 Numerical aspects

3.3.1 General approach

Accounting for surface reactions consists in describing the temporal evolution of the chemical activity at the surface by the resolution of surface kinetics on the hand, and characterizing the interplay between the gas-phase and surface reactions on the other hand. In this Section, the overall corresponding approach is described. It is performed with respect to the steps depicted in Figure 3.7. The inclusion of chemical

kinetics into the AVBP CFD code is addressed by introducing into the kinetic solver CLOE which is initially dedicated to the resolution of gas-phase kinetic schemes. For the purpose of addressing the heterogeneous chemistry found in catalytic converters, the kinetic solver was adapted during this thesis to allow accounting for surface chemistry via the introduction of the required set of equations and their resolution, as will be detailed in Subsection 3.3.3.

- STEP 1: First, the vector $\vec{\Pi}$ that includes the gas-phase species mass fractions at the wall ($Y_{k,w}^{hom}$), surface site fractions (θ_k) and wall temperature (T_w^{hom}) is defined as shown in Eq. 3.49. The index hom refers to the fact that the variable solely undergoes chemical reactions independently of transport.

$$\Pi_i = \begin{pmatrix} \Pi_1 \\ . \\ . \\ \Pi_{N_g} \\ \Pi_{N_g+1} \\ . \\ . \\ \Pi_{N_g+N_s} \\ \Pi_{N_g+N_s+1} \end{pmatrix} = \begin{pmatrix} \rho Y_{1,w}^{hom} \\ . \\ . \\ \rho Y_{w,N_g}^{hom} \\ \theta_1 \\ . \\ . \\ \theta_{N_s} \\ T_w^{hom} \end{pmatrix} \tag{3.49}$$

- Step 2: at each time step and every node of the wall, the i^{th} component of $\Pi_i(t)$ is sent to the kinetic solver CLOE to solve the surface reaction kinetics (Step 2a). In the meanwhile, the surface reaction rates ($\dot{s}_{k\in\Omega_s}$) are calculated in order to define the boundary conditions applied to the reactive wall (Step 2b).

- Step 3: The integration over a time step corresponding to dt_{min} is performed. Only the updated values of the site fraction are returned to the CFD code. The update of the mass fractions and the temperature is carried out by the CFD code. Nevertheless, the kinetic solver requires the values of the wall temperature and mass fractions in order to ensure a proper integration as will be shown in the next Subsection.

In what follows,the method ensuring the prescription of the proper boundary conditions accounting for surface reactions is presented at first. Second, the resolution of surface kinetics is dealt with.

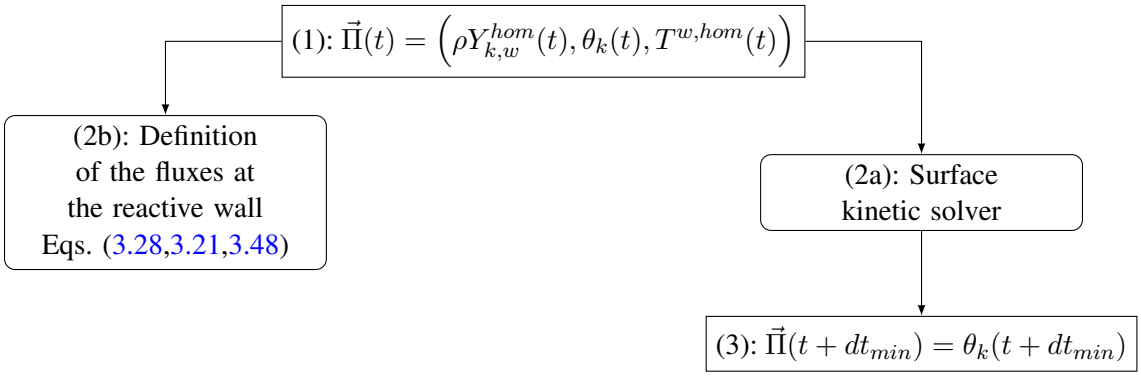

FIGURE 3.7: Coupling AVBP with the surface kinetics solver and boundary flux correction

3.3.2 Numerical implementation of the boundary conditions

A Dirichlet condition is applied to the velocity vector at the wall in order to impose the *Stefan* velocity as shown in Eq. (3.50).

$$\vec{u}_w^{cor} = U_{Stefan}\vec{n} \tag{3.50}$$

where $\vec{n}$ is the normal vector to the reactive wall, $\vec{u}_w^{cor}$ is the corrected velocity at the wall. The normal gas-phase species mass fraction gradients and the heat flux are numerically imposed at the reactive surface as shown in Eqs. (3.51, 3.52). First, the numerical scheme predicts the gradient of the k^{th} species mass fraction $\vec{\nabla}Y_{k,w}^p$ and the heat flux $\vec{q}_w^p$ at the reactive wall. These gradients are then modified by imposing the prescribed normal gradients and the normal heat flux $\vec{\nabla}Y_{k,w}^{BC} \cdot \vec{n}$ and $\vec{q}_w^{BC} \cdot \vec{n}$ respectively obtained from the mass and energy balance at the reactive interface given in Eqs. (3.22, 3.47).

$$\vec{\nabla}Y_{k,w}^{cor} = \vec{\nabla}Y_{k,w}^p + \left(\vec{\nabla}Y_{k,w}^{BC} \cdot \vec{n} - \vec{\nabla}Y_{k,w}^p \cdot \vec{n}\right)\vec{n} \tag{3.51}$$

$$\vec{q}_w^{cor} = \vec{q}_w^p + \left(\vec{q}_w^{BC} \cdot \vec{n} - \vec{q}_w^p \cdot \vec{n}\right)\vec{n} \tag{3.52}$$

where $\vec{\nabla}Y_{k,w}^{cor}$ and $\vec{q}_w^{cor}$ are the corrected species mass fraction gradient and heat flux, $\vec{\nabla}Y_{k,w}^p \cdot \vec{n}$ and $\vec{q}_w^p \cdot \vec{n}$ correspond to the normal component of the k^{th} species mass fraction and the heat flux predicted by the numerical scheme.

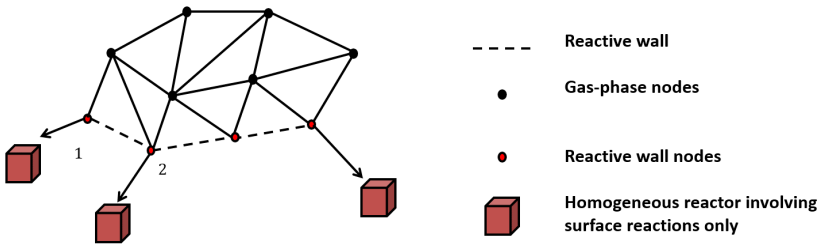

FIGURE 3.8: Physical view of the surface kinetics numerical resolution

3.3.3 Resolution of the surface kinetics

Figure 3.8 shows a physical view of the resolution of the surface kinetics. Physically speaking, each computational node of the wall mesh could be seen as an independent homogeneous reactor where gas-phase and surface species are involved in a set of surface reactions. In other words, surface chemistry is a local process separate for each reactive wall node and refers to an N_{nw} independent ODE systems comprising $N_g + N_s + 1$ unknowns where N_{nw} is the number of mesh nodes at the reactive wall.

The general form of the ODE system that is solved at the reactive wall nodes is written as follows:

$$\begin{cases} \vec{\Pi} = \left(\rho Y_{k,w}^{hom}, \theta_k, T_w^{hom}\right) \\ \dfrac{\partial \Pi_k}{\partial t} = R_k^{s,chem}(t) \quad \forall k = [1, .., N_s + N_g + 1] \end{cases} \tag{3.53}$$

where $R_k^{s,chem}$ is the chemical operator expressing the rate of change due to surface reactions. In addition to surface sites θ_k, the surface reaction rates depend on the temperature and gas-phase species as well. The temporal variation of T and $Y_{k,w}$ is required in the system in order to update their value at every sub-iteration in the case of implicit solvers such DVODE or DASAC. A proper resolution is thereby ensured. This results in a system having a size of $N_g + 1$:

$$\begin{cases} \vec{\Pi} = \left(\rho Y_{k,w}^{hom}, \theta_k, T_w^{hom}\right) \\ \dfrac{\partial \theta_k}{\partial t} = R_k^{s,chem}(t) = \dfrac{\dot{s}_k^{hom}}{\Gamma W_k} \quad \forall k \in \Omega_S \\ \dfrac{\partial \rho Y_{k,w}^{hom}}{\partial t} = R_k^{s,chem}(t) = \left(\dfrac{A}{V}\right)_w \dot{s}_k^{hom} \quad \forall k \in \Omega_G \\ \dfrac{\partial T_w^{hom}}{\partial t} = R_{N_g+N_s+1}^{s,chem}(t) = -\left(\dfrac{1}{c_{p,w}}\right) \left[\dfrac{\sum\limits_{k\in\Omega_G} h_{k,w} \left(\dfrac{A}{V}\right)_w \dot{s}_k^{hom}}{\rho} + \dfrac{\sum\limits_{k\in\Omega_S} h_{k,w} \dot{s}_k^{hom}}{\Gamma W_k} \right] \end{cases} \tag{3.54}$$

where $(A/V)_w$ stands for the local surface to volume ratio. $h_{k,w}$ is the total enthalpy at the wall expressed as follows:

$$h_{k,w} = h_{s,k,w} + \sum_{k\in[\Omega_G\cap\Omega_S]} \triangle h_{f,k}^o \dot{s}_k \tag{3.55}$$

If the reactive wall is supposed iso-thermal, the temperature does not need to be included thus making the system size equal to $N_g + N_s$ rather than $N_g + N_s + 1$. If the numerical method used by the kinetic solver does not involve any time sub-stepping or iterative methods such a first order Euler method, the temperature and species equations are no longer required. Hence the system size can be reduced to N_s instead of $N_s + N_g + 1$ thus becoming :

$$\begin{cases} \vec{\Pi} = (\theta_1, ..., \theta_k, .., \theta_{N_s}) \\ \dfrac{\partial \theta_k}{\partial t} = R_k^{s,chem}(t) = \dfrac{\dot{s}_k^{hom}}{\Gamma W_k} \quad \forall k \in \Omega_S \end{cases} \tag{3.56}$$

3.3.4 Limiting the time step by surface chemistry

In order to numerically capture the time variations related to surface reactions, the limitation of the integration time step dt_{min} by surface reactions might also required. The surface chemistry time step is therefore estimated using both gas-phase species and surface reaction rates $\dot{s}_k$. The following definitions are local as the time steps are determined at each node of the reactive wall:

$$\begin{cases} dt_{chem}^{surface,g} = \dfrac{\Gamma W_k}{\dot{s}_k} \ \forall k \in \Omega_G \\ dt_{chem}^{surface,s} = \dfrac{\Gamma W_k}{\dot{s}_k} \ \forall k \in \Omega_S \\ dt_{chem}^{surface} = min\left[dt_{chem}^{surface,g}, dt_{chem}^{surface,s}\right] \end{cases} \tag{3.57}$$

where $dt_{chem}^{surface,s}$ and $dt_{chem}^{surface,g}$ respectively refer to the characteristic time of consumption/production of surface coverages and gas-phase species through surface reactions. $dt_{chem}^{surface}$ is their minimum. The overall dt_{min} over which the integration of the governing equations is performed, is determined as follows:

$$dt_{min} = min\left[dt_{CFL}, dt_{F_o}^{min}, dt_{chem}^{surface}\right] \tag{3.58}$$

According to the estimation of $dt_{chem}^{surface}$ the following remarks should be taken into account:

- If surface chemistry is limiting and $dt_{chem}^{surface}$ is found too small resulting in a heavy computational time then the resolution of surface chemistry should be carried out using an implicit method (or explicit with sub-cycling) with an initial time step $dt_{min} = min\left[dt_{CFL},\ dt_{F_o}^{min}\right]$ which is used for the integration of transport as well.
- If surface chemistry is not limiting and $\dfrac{dt_{chem}^{surface}}{dt_{min}} > 10$ then the resolution of surface chemistry could be performed every n time steps where $n = \left[\dfrac{dt_{chem}^{surface}}{dt_{min}}\right]$. The underlying assumption is that the variations of gas-phase species and surface coverages due to surface reactions are not considered for a physical time that is equal to $n \times dt_{min}$. It is stressed that this approach might save a considerable CPU time but is likely to induce numerical instabilities.

3.4 Verification of the resolution of surface kinetics

In order to verify the inclusion of detailed gas phase and surface chemistry into AVBP, the coupling with the kinetic solver CLOE is applied to the simulation of a zero-dimensional heterogeneous reactor. It is composed of one computational cell whose boundaries are all set to be reactive walls, resulting in a simple closed volume reactor exhibiting gas phase and surface reactions, but no molecular or convective transport. The numerical results are compared with the ones obtained with a reference kinetic solver SENKIN of the CHEMKIN library [41]. Table 3.1 shows the initial conditions of the constant volume

reactor computations. The description and the numerical resolution method of the gas-phase chemistry are presented as well.

Mixture	ϕ	$\theta_{O(s)}(t=0)$	p(t=0), T(t=0)	Kinetic scheme	Integration method
CH_4/Air	0.37	1.0	1 atm and 1365 K	Reduced Aramco Mech 1.3 [42]	DVODE [40]

TABLE 3.1: Features of the homogeneous reactor computation. ϕ stands for the equivalence ratio. $\theta_{O(s)}(t=0)$, P(t=0) and T(t=0) are the initial $O(s)$ site fraction, pressure and temperature of the reactor.

The considered chemistry is representative of the lean catalytic combustion of a CH_4/Air mixture over Platinum Pt. $O(s)$ refers to the site fraction of the oxygen atom adsorbed over a Pt active site. $\theta_{O(s)}(t=0)=1$ means that the reactive surface is initially fully covered by oxygen atoms. The kinetic mechanism used to describe the gas-phase chemistry is similar to the one described in the previous Chapter. The kinetics of surface reactions are described using the mechanism of Deutschmann *et al.* [22, 48]. It uses 21 bidirectional and 3 unidirectional reactions with 7 gas-phase and 10 surface species involved. The implicit solver DVODE [40] is used for the resolution of both gas-phase and surface kinetics. Figure 3.9 shows the resulting time evolution of the gas-phase species mass fractions (CH_4, O_2 and OH), $O(s)$ site fraction $\theta_{O(s)}$ and temperature.

Notably, the time evolutions resulting from the present coupling (AVBP-CLOE) match very well the CHEMKIN results. This thereby verifies that the coupling with the kinetic solver properly ensures the resolution of surface chemistry and their kinetic interplay with the gas-phase.

In order to render the fact that surface reactions are exothermic under the present conditions, Figure 3.10 compares the gas-phase heat release per surface unit $(A/V)\times\dot{\Omega}_T$ with the heat release due to surface reactions $\dot{S}_T$ resulting fro the AVBP-CLOE computation (Similar lines were obtained with CHEMKIN). The level of $\dot{S}_T$ is clearly not negligible compared to its gas-phase counterpart. This proves the ability of the boundary condition derived in Section 3.2 to properly predict the temperature by taking into account the heat release rate through surface reactions.

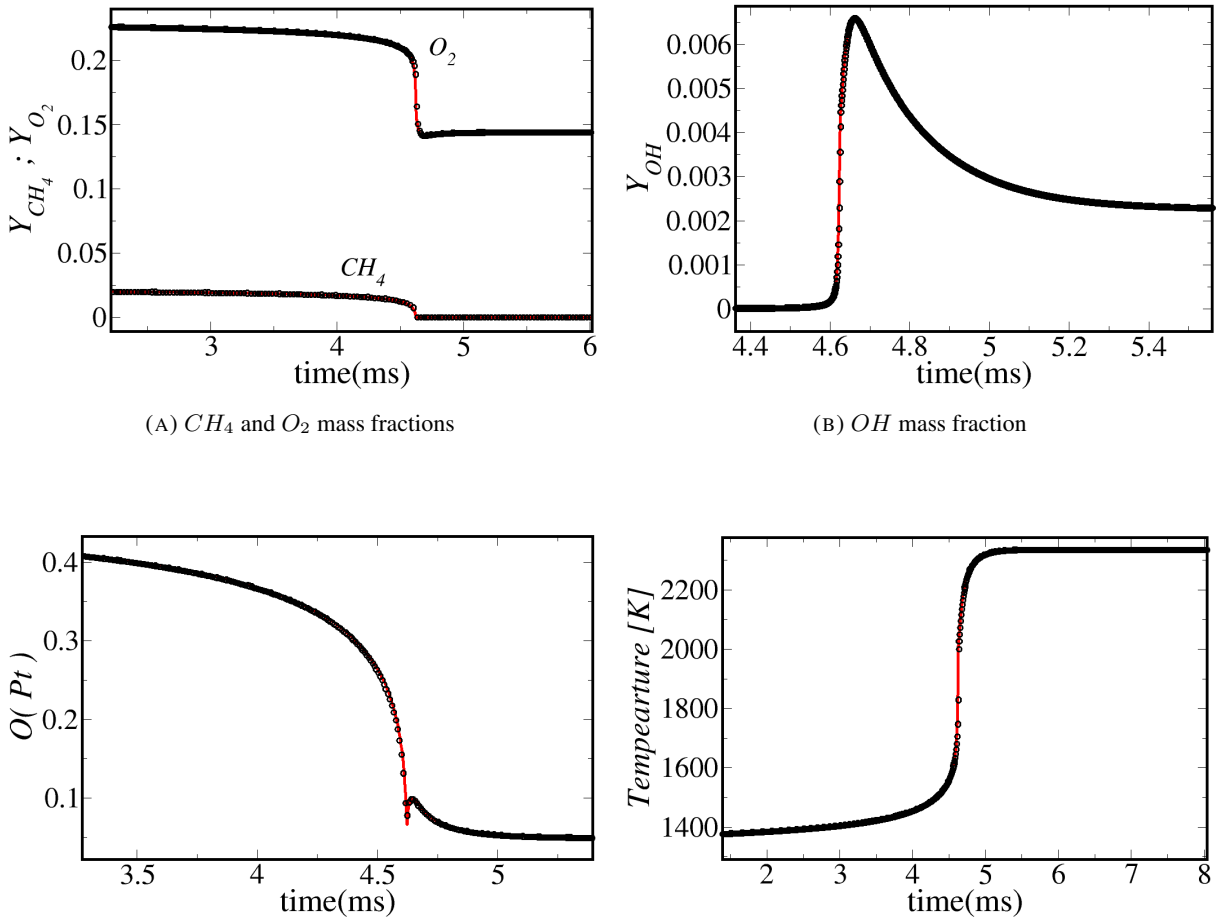

(A) CH_4 and O_2 mass fractions

(B) OH mass fraction

(C) $O(s)$ site fraction

(D) Temperature

FIGURE 3.9: Time evolution of the gas-phase species, $O(s)$ site fraction and temperature. Lines: AVBP-CLOE. Symbols: CHEMKIN

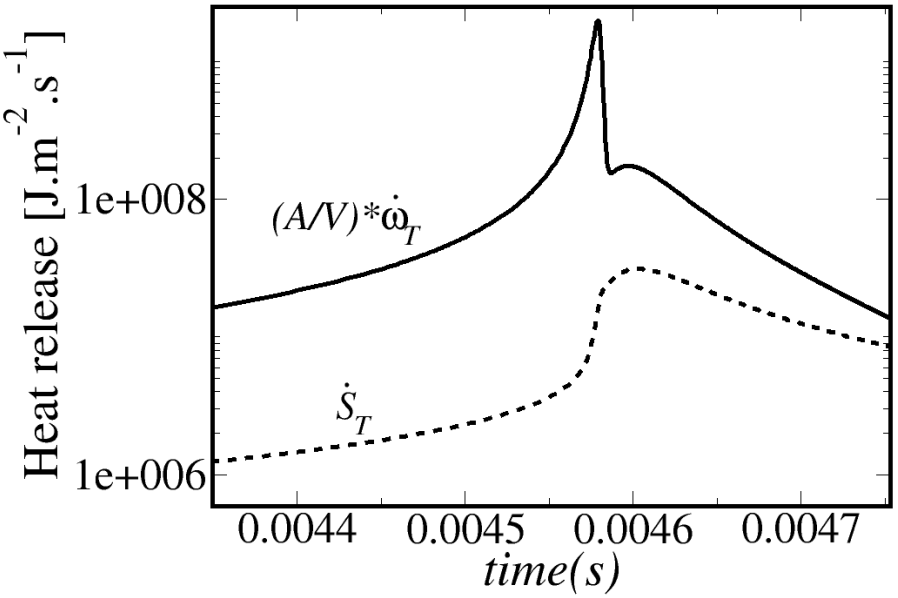

FIGURE 3.10: Comparison of the gas-phase and surface chemical heat release

Chapter 4

1D simulation: Ignition of a CO_2/O_2 quiescent mixture through gasification and oxidation of a carbonaceous surface

Note: This Chapter is a 1D application example that corresponds to the results of our published article in the International Journal of Heat and Mass transfer (IJHMT) [26]

introduction

Oxidation of carbonaceous surfaces is of major interest since it is involved in a wide range of energy production applications related to coal and biomass combustion and are of importance from the point of view of safety and environment [49]. For instance, oxy-fuel combustion is an efficient and cost-effective technology for the reduction of CO_2 emission from solid carbon based fuel fired furnaces such as coal char. To control operating temperatures, flue gas is typically recycled into the combustion chamber, forming O_2/CO_2 atmosphere. Solid carbon ignition in such an atmosphere represents an issue not only for combustion technology but also for safety [50]. Several numerical and analytical studies [51–54] have focused on the prediction of possible gas-phase ignition occurring in the vicinity of the reactive particles. The induced heat release may ruin the operating systems and provoke safety hazards.

Despite the lower oxygen diffusivity in CO_2 and the endothermicity of CO_2 gasification (Reduction of carbon conversion into carbon monoxide), the latter can actually lead to the enhancement of the overall carbon burning rate in oxy-fuel combustion [55, 56]. Under steady-state conditions the effect of CO_2 gasification on carbon conversion rate has been found to depend on O_2 concentration [57]. The interaction between CO_2 gasification and oxidation have been extensively studied [58, 59] especially at high pressure and high temperature [60] but remains poorly understood.

In O_2-enriched conditions, gasification can contribute significantly to carbon consumption [61]. Although the sequential occurrence [62] or respective importance [63] of homogeneous and heterogeneous ignition mechanisms have been evidenced experimentally, no detailed modeling work focused specifically, to our knowledge, on the interplay between CO production and consumption pathways under vitiated oxy-fuel combustion. The contribution of heterogeneous and homogeneous reactions to carbon ignition is known to depend on the gas-phase composition [60] as well as on carbon particle size [64] and surface temperature [65, 66]. Makino *et al.* [51] studied the temporal evolution of oxidation and gasification contributions using global kinetics and transport and formulated a criterion for the existence of a CO flame. Zou *et al* [67] addressed the homogeneous and heterogeneous ignition processes of pulverized coal in oxy-fuel combustion using an Eulerian-Lagrangian approach with devolatilization kinetic sub-models. The impact of volatiles combustion processes, ambient gas temperatures, coal particle size and O_2 concentrations on the ignition type were assessed. It was concluded that heterogeneous ignition is more likely to occur for small coal particles and high O_2 concentrations whereas homogeneous ignition launched by initial volatiles ignition is more likely to occur for large particles.

Many research groups still use simplified film models based on averaged diffusivity and global kinetics and neglect CO gas-phase conversion in the boundary layer. However, the predictability of simplified film models need to be further improved [68, 69]. Lewtak *et al.* [70] showed that the use of an equimolar counterdiffusion model overpredict the mass transfer towards the particle. A recent review [60] stressed the need to account for multi-species diffusion effect in carbon oxy-fuel combustion. The sensitivity of carbon consumption to *Stefan* flow was shown to depend on the relative contributions of gasification and oxidation reactions. *Stefan* velocity can reach significant values when the surface coverages undergo drastic change during transient processes [22] which may give rise to gas-phase ignition [17]. Thus it is important to take into account this additional velocity induced by reactive walls.

Theoretical studies have been carried out using global chemistry, highlighting the differences between transient and steady-state behavior [71], the impact of the relative importance of surface reactions on the shape of burning rate curve and the respective importance of homogeneous/heterogeneous chemistry and transport phenomena on particle ignition [52–54].

The aforementioned works reveal that transient homogeneous/heterogeneous carbon combustion data accounting for multi-species diffusion, surface and gas-phase micro-kinetics with proper species and energy boundary conditions taking into account the *Stefan* flux remain scarce. Hence, a one-dimensional transient heterogeneous case which consists of a quiescent CO_2/O_2 mixture initiated next to a carbonaceous reactive wall is performed in order to illustrate the interaction between molecular gas-phase diffusion and surface reactions. It consists of a quiescent CO_2/O_2 mixture initiated next to a carbonaceous reactive wall.

The structure of the present Chapter is as follows:

- First of all, an analytical solution is derived for a flow bounded by two reactive surfaces in Section 4.1. Analytical solutions are then compared with numerical numerical findings in order to validate the boundary conditions for mass and momentum.
- The numerical setup and modeling assumptions of the 1D application are described in Section 4.2.
- The transient dynamic of heterogeneous chemistry is analyzed in Section 4.3.
- Section 4.4 is dedicated to the assessment of the diffusion modeling.
- A parametric variation is carried out in Section 4.5 in order to evaluate the impact of the initial O_2/CO_2 ratio on the interplay between the gas-phase and surface chemistry.
- Finally, the convergence of the grid resolution is verified in Section 4.6.

4.1 Analytical solution for wall-bounded flow with carbonaceous wall gasification

Note: The analytical solution presented in the present Section is already reported by Cabrit et al. [24]. A special acknowledgment is also given to Moula et al. [72]. This Section was part of article published in the present thesis [26].

In this section the purpose is to derive an original analytical solution to validate the numerical species boundary condition for the heterogeneous surface reactions with frozen gas-phase. This solution can be used to understand the physics and easily analyze the influence of some physical parameters onto the studied phenomena. Moreover, analytical solutions are of wide interest for experimentalists or computational fluid dynamics users to validate their experimental/numerical procedure. Only the global approach

is described and the final solution is given. The complete development is provided as a supplementary material in Appendix C. It is sometimes possible to find the analytical solution of the system of partial differential equations that governs the physics of simple two-dimensional laminar flows. An example is the Poiseuille flow configuration which allows to give the analytical velocity/temperature profiles under the assumption of streamwise-developed steady flow [73]. Introducing the transpiring surface effects, Koh and Hartnett [74] have shown that the analytical solution can also be recovered for flow over permeable wedges. Hamza [21] also presented the solution of channel flow with transpiring and moving walls for biomechanics-fluid interest. Concerning reacting wall effects, Rosner [75] introduced a set of solutions for surface catalyzed problems. Duan and Martín [76] also mase use of an analytical solution for a diffusion-tube sidearm reactor in order to validate their numerical simulation of airflow over purely catalytic wall. To our knowledge, surface ablation has received little attention in the literature. Libby & Blake [61] developed an analytical solution for ablation but their case of study was purely diffusive. A special attention is given to the configuration set-up which allows to seek a steady-state solution. The idea consists in considering a channel problem of which the lower surface undergoes gaseous species production and solid carbon recession whereas the upper one encounters carbon deposition. Within this framework, the velocity and molar fraction profiles are derived and discussed. Global surface reactions and kinetic models are used, the purpose in this section being to seek numerical validation and not kinetic accuracy. The surface consumption has an effect on the flow since the products of the heterogeneous reactions include atoms that were originally embedded in the wall lattice. As a consequence, the surface geometry is changed according to the reaction rates at the surface. This feature makes the derivation of the solution more challenging, especially when a steady-state solution is sought for. As presented hereafter, the configuration set-up has to be properly thought to handle this undesirable effect. To simplify the derivation, one seeks for a solution that satisfies the following assumptions:

- two-dimensional laminar flow,
- steady state,
- channel flow developed in streamwise direction (periodic boundary conditions),
- non-reacting binary mixture (frozen state),
- constant *Schmidt* numbers,
- pure gasification (no pyrolysis or sublimation of the wall material),
- isothermal gasified surface with finite reaction rates,
- constant pressure and temperature.

In such a configuration, a special attention must be given to the chemical scheme retained for the heterogeneous surface reactions. Indeed, if the same scheme is applied to the two surfaces, this leads to a flow that similarly behaves at the wall surfaces. This means that the two convective wall normal velocity vectors induced by surface gasification are pointing towards opposite directions. This translates into an overall increase (or decrease) of mass that is not compatible with the steady state assumption. For this reason, one sets up a configuration in which one of the surface is consumed by a reaction while the reverse reaction takes place at the facing surface so mass increase or decrease in the domain is avoided. The set-up retained is summarized in Fig. (4.1). The flow is supposed to evolve in a streamwise periodic channel between two plates separated by the distance h. The wall normal direction is referenced by the letter y whereas x is used for the streamwise direction.

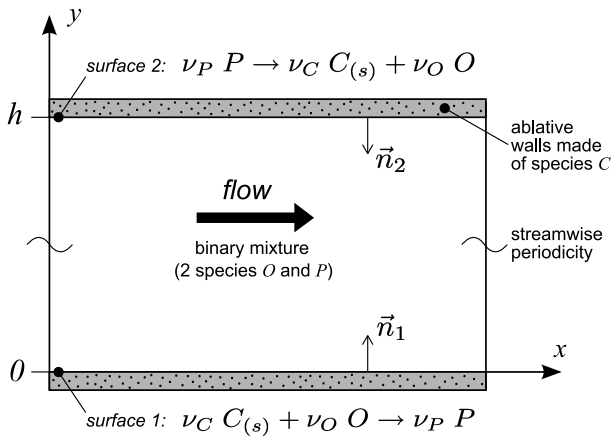

FIGURE 4.1: Sketch of the configuration.

Making use of the assumption of steady developed non-reacting flow, one can write mass/species/momentum conservation equations as:

$$\frac{\partial(\rho v)}{\partial y} = 0 \tag{4.1}$$

$$\frac{\partial}{\partial y}\left(\rho\left(v + V_{k,y}\right) Y_k\right) = 0, \quad k \in \{1, 2\} \tag{4.2}$$

$$\frac{\partial(\rho u v)}{\partial y} = \frac{\partial \tau_{xy}}{\partial y} + \mathcal{S} \tag{4.3}$$

$$\frac{p}{\rho} = \frac{R}{W} T \tag{4.4}$$

The momentum source term S is used for the following numerical and paractical reasons:

- Standard Inlet/Outlet boundary conditions imply the estimation of a pressure loss in the streamwise direction to include in the momentum conservation equation which is not an accurate approach for analytical solution derivation and not strictly conservative.
- Periodicity enables momentum conservation by imposing a momentum source thus being strictly conservative.

In the following, the letter C, O and P denote the solid wall species (which could be for instance solid carbon), the gaseous oxidizing species and the gaseous species produced by gasification, respectively. The associated stoichiometric coefficients are noted ν_C, ν_O and ν_P. According to these notations, the following chemical schemes are applied to the surface 1 (gasification):

$$\nu_C \, C_{(s)} + \nu_O \, O \rightarrow \nu_P \, P \tag{4.5}$$

and to the surface 2 (lieu of deposition):

$$\nu_P \, P \rightarrow \nu_C \, C_{(s)} + \nu_O \, O \tag{4.6}$$

In what follows, variables subscripted by letters C, O and P refer to the associated species and subscript numbers 1 and 2 refer to space location, $y = 0$ and $y = h$, respectively. The molar progress rate of reaction 1, $\mathcal{Q}_1$, can then be modeled as follows:

$$\mathcal{Q}_1 = \left(\frac{Y_{O,1}}{W_O} \rho_1 \right)^{\nu_O} K_1 = \left(X_{O,1} \frac{p}{RT} \right)^{\nu_O} K_1 \tag{4.7}$$

where K_1 represents the rate of reaction 1 which can be modeled by an *Arrhenius* law for instance. However, in the present framework it is not necessary to go deeper in the modeling of this coefficient because one assumes a constant temperature implying that K_1 can be merely seen as a parameter of the problem. Similarly, one can write the molar progress rate of reaction 2 as:

$$\mathcal{Q}_2 = \left(\frac{Y_{P,2}}{W_P} \rho_2 \right)^{\nu_P} K_2 = \left(X_{P,2} \frac{p}{RT} \right)^{\nu_P} K_2 \tag{4.8}$$

Moreover, the general formulation of species conservation balance at the reacting surfaces reads:

$$\left(\rho_j \vec{u} Y_k + \rho \vec{V}_k Y_k \right) \cdot \vec{n} = \dot{s}_k \tag{4.9}$$

The species conservation balance at surface 1 reads:

$$\rho_1 v_1 Y_{k,1} + \rho_1 V_{k,1} Y_{k,1} = \dot{s}_{k,1} \tag{4.10}$$

and at surface 2:

$$\rho_2 v_2 Y_{k,2} + \rho_2 V_{k,2} Y_{k,2} = -\dot{s}_{k,2} \tag{4.11}$$

where $\vec{n}$ is the vector normal to the wall and pointing toward the gas-phase. Summing over all the species and making use of the mass conservation constraints $\sum_k Y_k = 1$ and $\sum_k Y_k V_k = 0$, one obtains the two relations $\rho_1 v_1 = \sum_k \dot{s}_{k,1}$ and $\rho_2 v_2 = -\sum_k \dot{s}_{k,2}$. Furthermore, the continuity equation Eq. (4.1) imposes that $\rho(y)v(y)$ is constant (in the forthcoming the notation $\dot{m} = \rho(y)v(y)$ will be used). As a consequence, one finds that $\dot{m} = \sum_k \dot{s}_{k,1} = -\sum_k \dot{s}_{k,2}$ which leads to the relation $\mathcal{Q}_1 = \mathcal{Q}_2$ (the notation $\mathcal{Q} = \mathcal{Q}_j$ is thus retained for simplification). The two progress rates of the surface reactions are thus identical. The relation between the wall normal mass flow rate and the progress rate of reaction is thus expressed as:

$$\dot{m} = \mathcal{Q}\left(\nu_P W_P - \nu_O W_O\right) \tag{4.12}$$

When the species diffusion due to pressure gradients, temperature gradients (*Soret* effect) and volume forces are neglected, the binary diffusion between the two species O and P can be modeled by the classical relation [30]
$V_k Y_k = -\mathcal{D}_{OP}^{\text{bin}} \; \partial Y_k / \partial y$, where $\mathcal{D}_{OP}^{\text{bin}} = \mathcal{D}_{PO}^{\text{bin}}$ is the binary diffusion coefficient. Another formulation is obtained by considering equivalent diffusion coefficients, D_k, that represents the diffusion of species k into the mixture and expressed as $D_k = (1 - Y_k)/(\sum_{l \neq k} X_l / \mathcal{D}_{kl}^{\text{bin}})$. This leads to an equivalent diffusion model which now involves the species molar fractions instead of their mass fractions, $V_k X_k = -D_k \; dX_k/dy$. This presents a strong advantage for solving the system of equations. Note also that contrary to the binary coefficient, D_k is depending on the local concentration of each species which means that $D_k = D_k(y)$. According to the previous definitions, the following relation stands for the present mixture:

$$D_O W_O = D_P W_P \tag{4.13}$$

Moreover, the dynamic viscosity for gases is usually assumed to be solely temperature dependent which means that in the present isothermal framework μ is a constant. Since the *Schmidt* numbers, $Sc_k = \mu/(\rho D_k)$, are assumed to be constant, we find that $\rho(y) D_k(y)$ is also constant. This statement allows

to simplify the integration of the forthcoming partial differential equations. In order to determine the species concentration profiles, one may concentrate on the variable X_O and then deduce the concentration of species P by the relation $X_P = 1 - X_O$. At this step, it is important to consider molar fractions instead of mass fractions because it leads to a first order partial differential equation with constant coefficients. Indeed, making use of Eq. (4.2), integrating once and identifying with Eq. (4.10), rearranging in terms of molar fractions, and making use of $\rho(y)D_O(y) = \mu/Sc_O$ yields:

$$\eta X_O - \frac{\mu}{Sc_O\ \dot{m}} \frac{dX_O}{dy} = \frac{\nu_O W_P}{\nu_O\ W_O - \nu_P\ W_P} \tag{4.14}$$

with

$$\eta = \frac{W_P\,(\nu_O - \nu_P)}{\nu_O\ W_O - \nu_P\ W_P} \tag{4.15}$$

Since $\eta = 0$ for $\nu_O = \nu_P$, the integration of this differential equation leads to two solutions depending on the values taken by ν_O and ν_P:

$$\begin{aligned} &X_O(y) = \left(X_{O,1} - \frac{\nu_O}{\nu_O - \nu_P}\right) \exp\left[\eta\ \frac{Sc_O\ \dot{m}}{\mu}\ y\right] + \frac{\nu_O}{\nu_O - \nu_P} \\ &\text{for}\ \ \nu_O \neq \nu_P \\ &X_O(y) = -\frac{Sc_O\ \dot{m}}{\mu}\ \frac{W_P}{W_O - W_P}\ y + X_{O,1} \\ &\text{for}\ \ \nu_O = \nu_P \end{aligned} \tag{4.16}$$

where $X_{O,1}$ is the molar fraction of species O at surface 1. The value of this constant is determined thanks to the relation between $X_{O,1}$ and $X_{O,2}$ that comes from the identity $\mathcal{Q}_1 = \mathcal{Q}_2$ which according to Eqs. (4.7, 4.8) gives:

$$X_{O,1}^{\nu_O} \left(\frac{p}{RT}\right)^{\nu_O - \nu_P} \frac{K_1}{K_2} = (1 - X_{O,2})^{\nu_P} \tag{4.17}$$

Furthermore, injecting Eq. (4.7) into the wall normal mass flow rate Eq. (4.12) yields the dependency relation between $\dot{m}$ and $X_{O,1}$

$$\dot{m} = X_{O,1}^{\nu_O} \left(\frac{p}{RT}\right)^{\nu_O} K_1 \ (\nu_P W_P - \nu_O W_O) \tag{4.18}$$

Hence, Eq. (4.16) expressed for $y = h$ can be injected into Eq. (4.17), and with the use of Eq. (4.18) one obtains an equation in which $X_{O,1}$ is the only unknown. This manipulation allows determining the $X_{O,1}$ constant and Eqs. (4.15-4.18) form the analytical solution for the molar fraction of species O. The molar fraction of P is then given by the relation $X_P(y) = 1 - X_O(y)$. Concerning the determination of the streamwise velocity profile, one introduces the newtonian fluid relation $\tau_{xy} = \mu du/dy$ into Eq. (4.3) which gives $\rho v \ du/dy - \mu \ d^2u/dy^2 = \mathcal{S}$. Since μ is a constant under the approximation of constant temperature, and because $\rho(y)v(y) = \dot{m}$ is a constant according to the continuity Eq. (4.1), the latter differential equation is merely of second order with constant coefficients. Its integration with the boundary conditions $u(0) = u(h) = 0$ leads to the following solution:

$$u(y) = \frac{\mathcal{S}}{\dot{m}} \left[\frac{h}{\mathrm{e}^{\frac{\dot{m}}{\mu}h} - 1} \left(1 - \mathrm{e}^{\frac{\dot{m}}{\mu}y}\right) + y \right] \tag{4.19}$$

where $\dot{m}$ is determined from Eq. (4.18). The maximum streamwise velocity is expected to be observed at the wall normal distance:

$$y|_{u_{max}} = \frac{\mu}{\dot{m}} \ln \left[\frac{\mu}{h \, \dot{m}} \left(\mathrm{e}^{\frac{\dot{m}}{\mu}h} - 1\right) \right] \tag{4.20}$$

The comparisons of analytical and numerical solutions for the wall normal velocity component, the mass fraction of the oxidizing species and the streamwise velocity are presented in Figs. (4.2a-4.2b) for CO_2 gasification. It is noticed that the wall normal distance for which the maximum velocity is observed $y|_{u_{max}}$ is identical to the channel half-height $h/2$. Moreover, the fluid encouters the same wall shear stress at both surfaces, i.e, $\tau_{w,2}/\tau_{w,1} \approx 1$. These cases correspond to values of mass rates that are too low to modify the streamwise velocity profiles significantly (Table 4.2). As a result, these profiles are very close to the impermeable wall solution. The analytical solutions are identical to the numerical ones, showing that the boundary conditions taking into account the *Stefan* velocity are able to predict correctly the influence of surface reactions on gas-phase species and momentum given respectively in Figs. (4.3, 4.2b).

TABLE 4.1: Parameters of the test cases.

case	$Oxidizer\ (O)$	$Product\ (P)$	ν_O	ν_P	Sc_O	Sc_P	$K_1 = K_2\ (kg.m^{-1}.mol^{-1}.s^{-1})$ [61]	$P(atm)$
1	CO_2	CO	1	2	0.92	0.59	6.92×10^{-3}	1
2	CO_2	CO	1	2	0.92	0.59	5.2×10^{-2}	1
3	CO_2	CO	1	2	0.92	0.59	0.49	1

TABLE 4.2: Characteristic values of the test cases.

case	$\dot{m}$	$\frac{y\|_{u_{max}}}{h}$	$\tau_{w,2}/\tau_{w,1}$
1	3.87×10^{-4}	0.5	1
2	2.16×10^{-3}	0.5	1.01
3	8.88×10^{-3}	0.5	1.052

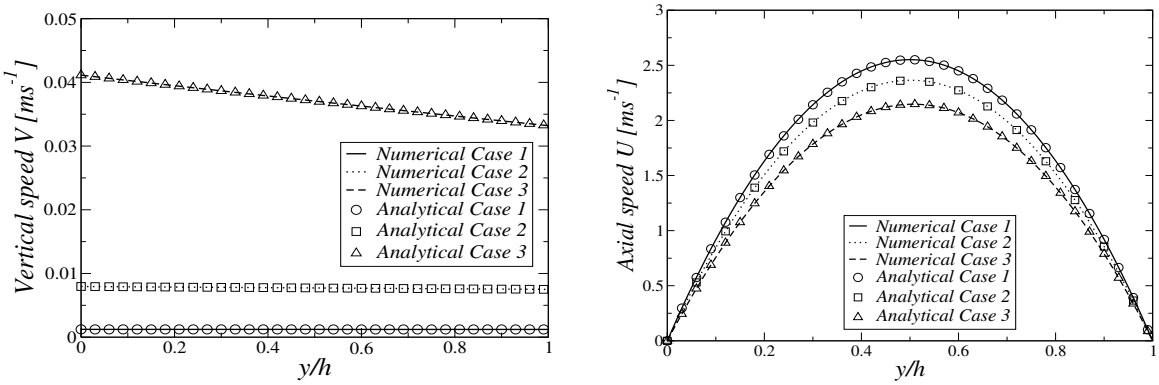

(A) Vertical velocity (B) Streamwise velocity

FIGURE 4.2: Analytical and numerical spatial profiles

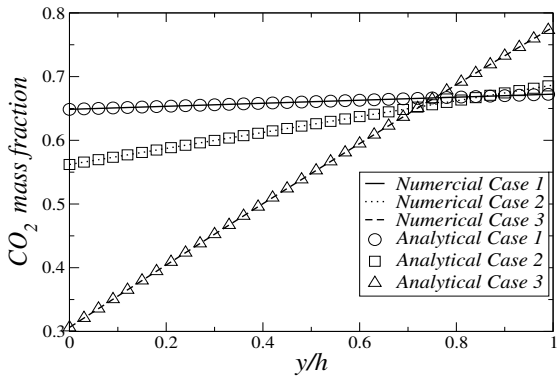

FIGURE 4.3: Analytical and numerical spatial profiles of species mass fractions

4.2 Setup of the numerical simulation

4.2.1 Sizing the numerical setup

The considered problem is purely 1D, variations occurring exclusively between the upper and lower surface and all fields being homogeneous in the y and z directions because of periodicity. The configuration studied is a parallelipipedic channel containing initially a quiescent and homogeneous O_2/CO_2 mixture. Solid carbon consumption and CO/CO_2 production through surface gasification and oxidation takes place at the lower wall, whereas the upper surface corresponds to an outlet ensuring a constant pressure within the whole channel. The channel height h is higher than the distance $l_{diff} = \sqrt{\tau_{chem}\left(\nu/\bar{Sc}\right)\mid_{t=0}}$ characterizing diffusion within a chemical time τ_{chem}. The latter is evaluated in a homogeneous adiabatic reactor provided with identical initial thermodynamic and thermal-chemical conditions as the present studied case. The corresponding value of τ_{chem} coincides with complete depletion of surface carbon, i.e, $\theta_{C(S)} = 0$. $\left(\nu/\bar{Sc}\right)\mid_{t=0}$ refers to the ratio of kinematic viscosity and the average Schmidt number of the mixture. According to this approach, the initial *Damköhler* number (Da) is much larger than unity which makes the combustion process overall diffusion-limited.

$$Da = \left(\frac{h}{l_{diff}}\right)^2 >> 1 \tag{4.21}$$

The surface over volume ratio A_{wall}/V ensures that the gas and surface reactions contributions to CO_2 and O_2 consumption and production are of the same order of magnitude which implies that the surface species consumption proceeds at a rate as fast as gas-phase chemistry. A_{wall} being the chemically active surface area of the lower wall (Figure 4.4), the ratio A_{wall}/V reads :

$$\frac{A_{wall}}{V} = \frac{a^2}{a^2 h} = \frac{1}{h} \tag{4.22}$$

Variables initialization is spatially homogeneous, Table 4.3 summarizes the initial concentrations and thermodynamic parameters for the reference case. The transport coefficients are determined using the EGLIB library [77].

TABLE 4.3: Initial conditions of the reference case

$T(t=0)$	$Y_{O_2}(t=0)$	$Y_{CO_2}(t=0)$	$\theta_C(t=0)$
$1600K$	0.63	0.37	1

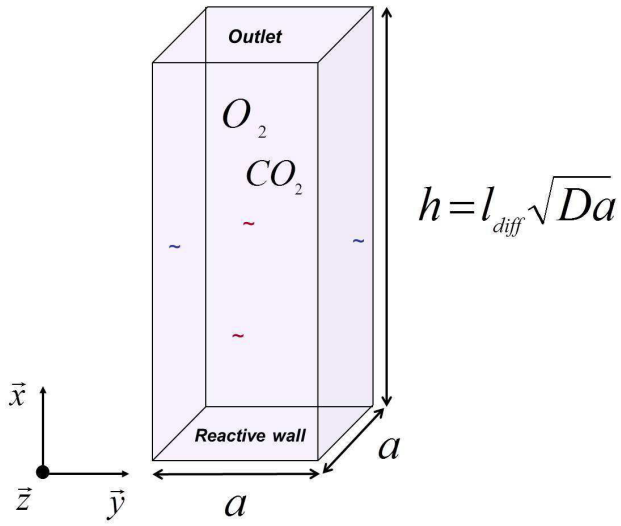

FIGURE 4.4: Schematic drawing of the setup

4.2.2 Boundary conditions

An adiabatic condition is applied to the lower reactive surface which means that the temperature of the reactive wall presents temporal variations based on the heat flux balance given in Eq. (3.47). The condition is called adiabatic in the sense that no thermal conduction is accounted for within the solid, which means that $\lambda^s \vec{\nabla} T_w^s \cdot \vec{n} = 0$. The latter expression implies that the prescribed normal heat flux at the wall becomes :

$$\begin{aligned} \vec{q}_w^{BC} \cdot \vec{n} = &- \sum_{k \in \Omega_S} h_k \dot{s}_k - \sum_{k \in \Omega_G} \triangle h_f^o \dot{s}_k \\ &- \rho_w \sum_{k \in \Omega_G} U_{Stefan} h_{s,k,w} Y_{k,w} \\ &- \frac{\dot{m}}{2} \sum_{j \in \mathcal{D}} u_{j,w}^2 + \left(\bar{\bar{\tau}} \vec{u}\right)_w \cdot \vec{n} \end{aligned} \tag{4.23}$$

The prescribed mass fraction gradient at the wall is given by Eq. (3.28). The upper face is an outlet surface that relaxes the pressure toward the targeted atmospheric pressure in a partially non-reflecting way using the NSCBC method [78, 79]. This allows to control waves reflections and avoids the propagation of non-physical fluctuations. No conditions are applied to the species mass fractions, heat flux and velocity at the outlet :

$$Y_k \mid_{outlet} = Y_k^p, \quad \vec{q} \mid_{outlet} = \vec{q}^p, \quad \text{and} \quad \vec{u} \mid_{outlet} = \vec{u}^p \tag{4.24}$$

Where Y_k^p, $\vec{q}^p$ and $\vec{u}^p$ are respectively the values of species mass fractions, heat flux and velocity predicted by the numerical scheme. Periodic boundary patches are imposed to the lateral faces. Regarding the mesh, starting from the wall to $x/l_{diff} = 0.865$, mesh cells have a size of $10\mu m$ which means that 1000 cells populate the near-wall region. For $0.865 < x/l_{diff} < \sqrt{D_a}$, a mesh coarsening has been carried out to reach a maximum cell size of $75\mu m$ at the outlet. As will be discussed in section 4.6, a grid convergence study is carried out to determine the proper grid resolution in the reactive near-wall region. Regarding the numerical scheme, a second-order cell-vertex implementation of the Finite Volume Lax-Wendroff convection scheme is used for time and space integration [33, 34, 80, 81]. It is associated in this study with a Finite Element diffusion scheme with a 2Δ operator that comes from a strict application of the Finite Element Galerkin method [82]. This approach has been used to save CPU time and because the mesh is considered fine enough for an acceptable second-order approximation. It also reminded that the diffusive terms are solved explicitly.

4.2.3 Gas-phase and surface kinetics description and validation

The surface-phase mechanism (Table 4.4) was extracted from a previously developed and validated semi-detailed kinetic mechanism [63, 83, 84]. The impact of backward reactions is expected to be negligible under typical oxy-combustion conditions and the validity of this hypothesis over a wider range of conditions is outside the scope of the present study. Two additional reactions representing the adsorption of CO_2 (S4) and oxygen radicals O (S5) upon carbon sites have been accounted for. The kinetic parameters of surface reaction (S1 to S3) related to char oxidation are similar to those recommended by Hurt *et al* [85], whereas those of CO_2 adsorption ($S4$) are in line with values proposed by Hecht *et al* [57]. The resulting detailed kinetic surface mechanism involves a lumped intermediate species, $C(O)$, standing for oxygenated surface species formed during oxidation and a single type of carbon site, $C(S)$, was chosen to describe solid carbon sites. The mechanism has been validated against continuously stirred tank reactor (CSTR) experiments by comparing predicted carbon conversion rates with the experimental data for char gasification and oxidation [86]. The simulations were carried out using Surface Chemkin kinetic solver [87]. Comparisons of the carbon conversion are shown in Figure 4.5corresponding to carbon O_2 oxidation and CO_2 gasification. The validation covers various concentrations of diluted O_2 and CO_2 using chemically inert molecular nitrogen N_2 as a balance dilution gas. Regarding the gas-phase mechanism, the three reversible elementary reactions of dry CO oxidation given in Table 4.5 were extracted from the GRI

2.11 mechanism. This reaction set was then validated against shock tube experiments of Brabbs *et al.* for CO_2 dissociation [88].

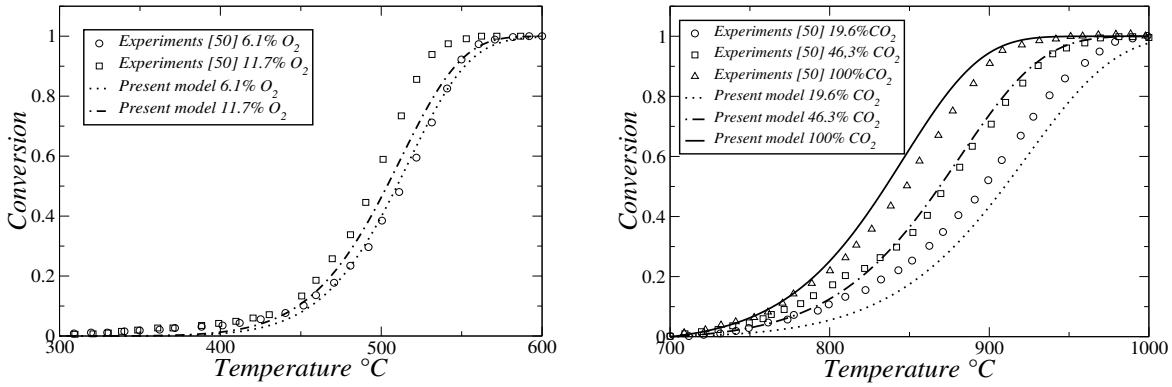

(A) O_2/N_2 environment (B) CO_2/N_2 environment

FIGURE 4.5: Carbon conversion in a O_2/N_2 and CO_2/N_2 environment. The volumetric flow rate is 100 SCCM (Standard Cubic Centimeter per Minute) and the heating rate is 10K/min.

TABLE 4.4: Surface reaction mechanism for the configuration of Fig. 4.4

Step	Reaction	α_j $\left(cm^{2(n-1)}.mol^{1-n}.s^{-1}\right)$	β_j	$E_j(kJ.mol^{-1})$	ref.
S1	$C(S)+\frac{1}{2}\,O_2 \rightarrow C(O)$	5.0×10^{6}	0.0	45	[63]
S2	$C(O) \rightarrow CO$	2.7×10^{6}	0.0	132	[63]
S3	$C(O)+\frac{1}{2}\,O_2 \rightarrow CO_2$	1.33×10^{5}	0.0	109	[63]
S4	$CO_2 + C(S) \rightarrow C(O) + CO$	1.0×10^{13}	0.0	225	[86]
S5	$O+C(S) \rightarrow C(O)$	$\left(\frac{\gamma}{\Gamma^m}\right)\sqrt{\frac{R}{2\pi W_O}}$	0.5	0.0	[89]

TABLE 4.5: Gas-phase reaction mechanism for the configuration of Fig 4.4

Step	Reaction	$\alpha_j\left(cm^{3(n-1)}.mol^{1-n}.s^{-1}\right)$	β_j	$E_j(kJ.mol^{-1})$.
R1	$2O+M \rightleftharpoons O_2+M$	1.2×10^{17}	-1.0	0.0
R2	$O+CO+M \rightleftharpoons CO_2+M$	6.02×10^{14}	0.0	12.55
R3	$O_2+CO \rightleftharpoons O+CO_2$	2.5×10^{12}	0.0	200.1

4.3 Transient history

The reference case (Table 4.3) is characterized by two gas-phase reaction zone configurations represented in the schematic of Figure 4.6. The first one corresponds to a wall-attached CO-reaction zone maintained by the competition between the CO/O_2 combustion and surface reactions, whereas the second one is characterized by the extinction of surface reactions and a gas-phase reaction zone evolving at a certain distance of the reactive wall. Therefore, two main combustion modes characterize the reference case and the switch between these modes occurs at $t_{switch} = 0.22s$ under the conditions used in this study. This time coincides with the depletion of surface carbon $(\theta_c = 0)$ and is the same order of τ_{chem}. As a consequence, time is normalized by the time corresponding to the combustion mode switch t_{switch}. The resulting normalized time being noted $\tau = t/t_{switch}$.

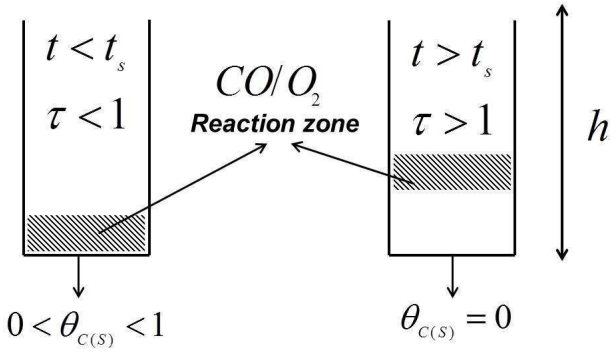

FIGURE 4.6: Gas-phase CO/O_2 reaction zone configurations

Figure 4.7a shows the time evolution of space averaged mass fraction of the k^{th} species at the reactive wall determined as shown in Eq. (4.25).

$$\langle Y_{k,wall} \rangle = \frac{\int_S Y_k(x=0)dS}{A_{wall}} \tag{4.25}$$

For $\tau \leq 1$, CO_2 and O_2 species present in the gas-phase diffuse to the carbonaceous wall, are adsorbed and converted on surface as shown by their respective decreasing mass fractions at the wall shown in Figure 4.7a. CO_2 and O_2 adsorption upon the reactive surface coincides with consumption of surface carbon and CO production through gasification. CO production by the reactive surface is described by the increasing profile of CO mass fraction (Figure 4.7a) and the decreasing profile of carbon site fraction θ_C (Figure 4.7b). CO diffuses to the gas-phase and reacts with O_2 thus producing CO_2. Carbon

monoxide consumption and carbon dioxide production through gas-phase combustion are illustrated by the respective rise and fall of CO_2 and CO concentrations for $0.97 \leq \tau \leq 1.0$. At $\tau = 1$, surface carbon consumption reaches completion which puts an end to surface reactions. Gas-phase CO_2/O_2 combustion is the only active chemical process which gradually fades.

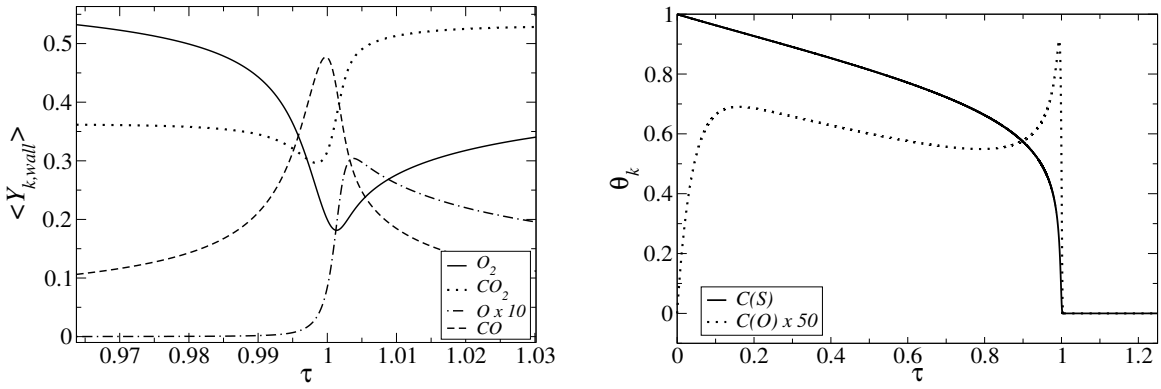

(A) Gas-phase species mass fractions at the reactive surface

(B) Surface coverages

FIGURE 4.7: Evolution of Gas-phase species at the wall and surface coverages versus normalized time τ

Wall-attached reaction zone

In order to quantify the competition between gas-phase and surface reactions, an index I_k for each k^{th} species is defined in Eq. (4.26):

$$I_k = \frac{|\langle \dot{s}_k \rangle|}{|\langle \dot{s}_k \rangle| + |\langle \dot{\omega}_k \rangle|} \tag{4.26}$$

where $\langle \dot{\omega}_k \rangle$ and $\langle \dot{s}_k \rangle$ are respectively the gas-phase and surface space averaged production/consumption rates that read:

$$\langle \dot{\omega}_k \rangle = \int_{\mathcal{V}} \dot{\omega}_k d\mathcal{V}, \qquad \langle \dot{s}_k \rangle = \int_{S} \dot{s}_k dS \tag{4.27}$$

I_k characterizes the contributions of surface and gas-phase reaction regardless of its sign (production/consumption). Figure 4.8 presents the evolution of I_{O_2}, I_{CO_2} and I_{CO} versus the normalized time τ. As can be noticed, the index I_k varies between 0 and 1 thus showing that the existence of a wall-attached reaction zone coincides with the competition between surface and gas-phase chemistry. As a matter of fact, I_{O_2},

I_{CO_2} and I_{CO} are higher than 0.5 for $\tau \leq 0.24, 0.7$ and 0.75 respectively, which means that surface-phase chemistry is as much involved into species consumption or production as the gas-phase one. I_{CO} and I_{CO_2} show a stiff decrease when τ tends to 1 because of the quick drop of surface carbon site fraction as shown in Figure 4.7. This is due to the thermal runaway caused by the exothermic surface carbon oxidation (S1 to S3) and gas-phase reactions. A slight increase can be noticed before I_{CO_2} decreases rapidly which is due to the production of CO_2 by reaction $S3$ (Table 4.4).

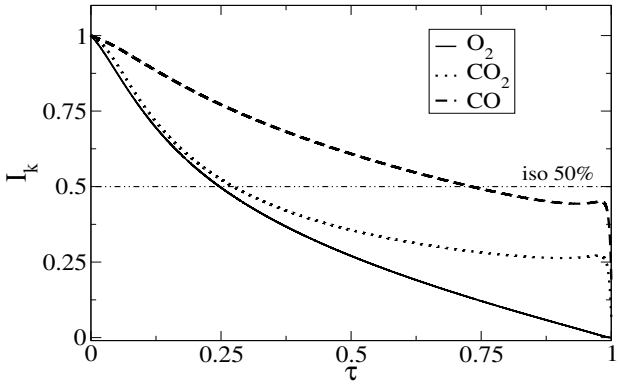

FIGURE 4.8: I_k versus τ

CO provided by the surface feeds a CO/O_2-combustion characterized by a reaction front at proximity of the reactive wall. Figure 4.9 presents the reaction zone identified by the gas-phase temperature (a) and the peaks of heat release (b). These peaks intensify and move slightly upward toward rich zones that are less O_2 diffusion limited but do not go beyond $x/l_{diff} = 0.215$. Note that the reaction zone thickness (non-zero values of $\dot{\omega}_T$) corresponds to regions where surface produced CO has diffused enough to react with O_2 thus covering a length that is the same order of the *a priori*-estimated characteristic diffusive length l_{diff} as τ tends to unity, i.e, as physical time t tends to one chemical characteristic time τ_{chem}. This CO/O_2-reaction zone configuration is analogous to the "attached CO-flame" mode described by Makino [90]. The reaction zone is continuously fed by CO provided by the surface ($\langle \dot{s}_{CO} \rangle > 0$), it remains attached to the wall despite the increase of O_2 gradient.

Figure 4.10 shows at two different times during the wall-attached reaction zone phase the evolution of normalized species spatial profiles. Normalized scalars noted $\widehat{\Phi}_k$ are defined as shown in Eq. (4.28).

$$\widehat{\Phi}_k = \frac{\Phi_k - \Phi_{k,min}}{\Phi_{k,max} - \Phi_{k,min}} \tag{4.28}$$

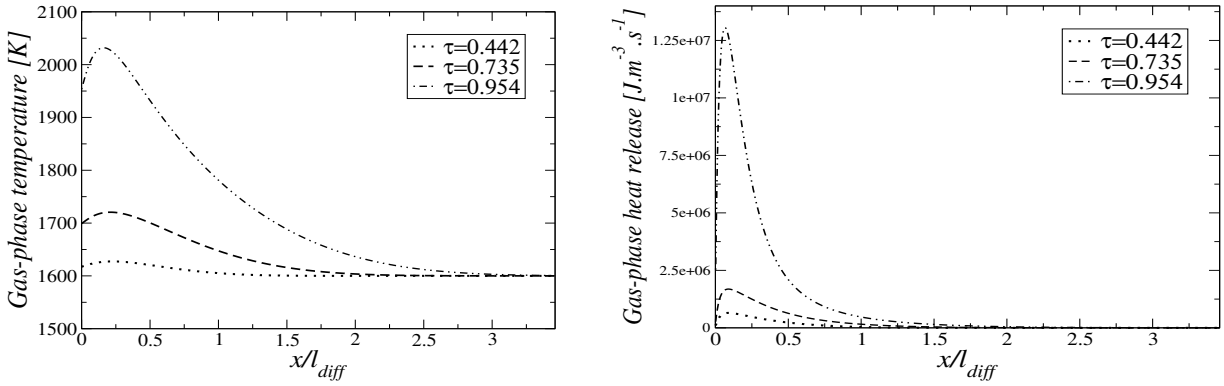

(A) Gas-phase temperature profiles

(B) Gas-phase heat release profiles

FIGURE 4.9: Temperature and gas-phase heat release profiles during the "attached CO-flame" mode

where $\Phi_{k,min}$ and $\Phi_{k,max}$ are respectively the minimum and maximum values of the scalar Φ_k at a given time τ.G as-phase combustion occurrence coincides with a decrease of O_2 in the reaction zone and the formation of a peak on CO_2 profile. At $\tau = 0.442$, the minimum of CO_2 concentration is at the wall because of its consumption by surface carbon. As CO/O_2 reaction becomes significantly active in the gas-phase, CO_2 production contributes to generate a peak in the corresponding concentration spatial profile at $x/l_{diff} = 0.425$ at $\tau = 0.954$ identifying the gas-phase reaction front.

The wall-attached reaction phase ($\tau \leq 0.06$) begins with an endothermic process during which CO_2 oxidizes carbon. CO_2 adsorption through surface reaction causes a drop in both wall (Figure 4.11a) and gas-phase temperatures (Figure 4.11b). Indeed, the temperature decrease is due to the endothermicity of CO_2 gasification of carbon. Figure 4.11a shows the decrease of the surface temperature during the endothermic phase ($\tau \leq 0.06$) causing an increase of the positive gas-phase temperature gradient at the reactive wall as described in Figure 4.11b. Meanwhile, CO mass fraction gradually increases at the wall, thus resulting in a sharper gradient as can be seen in Figure 4.11c.

Gas-phase reactions after surface carbon depletion

An overview of the gas-phase reaction zone displacement is shown in Figures 4.12a, 4.12b. As carbon reaches depletion, surface reaction rates decrease which induces a change in the reaction structure. At $\tau = 1.0$, surface chemistry is not active anymore ($\langle \dot{s}_k \rangle = 0$) as shown by Figure 4.8. Temperature in proximity of the wall reaches values higher than $3000K$ (Figure 4.12) favoring CO_2 gas-phase dissociation thus causing a detachment of the reaction front. Figure 4.12a shows negative heat release rates near the wall region related to O_2 and CO_2 dissociation by $R1$ and $R2$ (Table 4.5). CO is not generated anymore by the reactive surface so that the reaction zone loses its attachment to the surface. The resulting reaction zone moves toward the outlet. Figure 4.12b shows spatial profiles of the gas-phase temperature for different

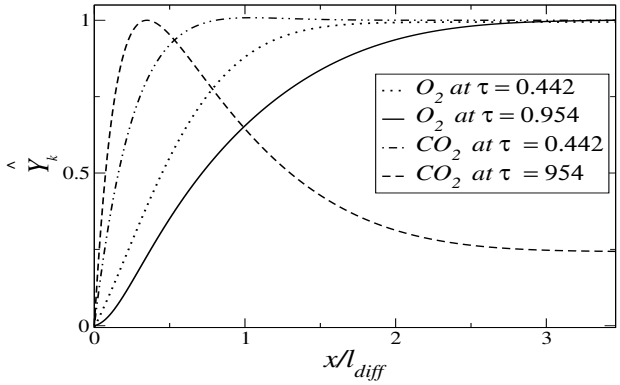

FIGURE 4.10: Spatial profiles of $\widehat{Y}_{O_2}$ and $\widehat{Y}_{CO_2}$

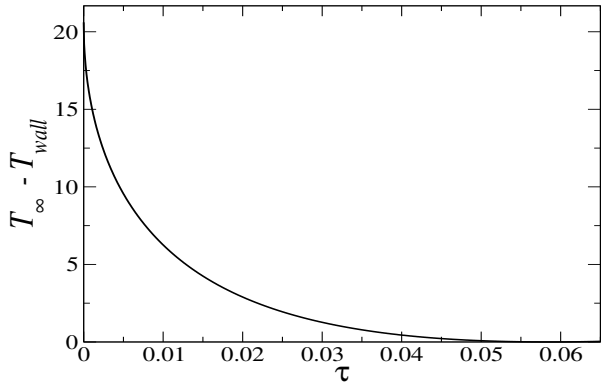

(A) Wall temperature

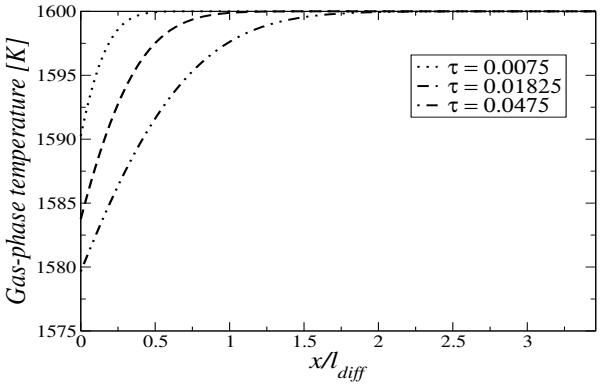

(B) Gas-phase temperature

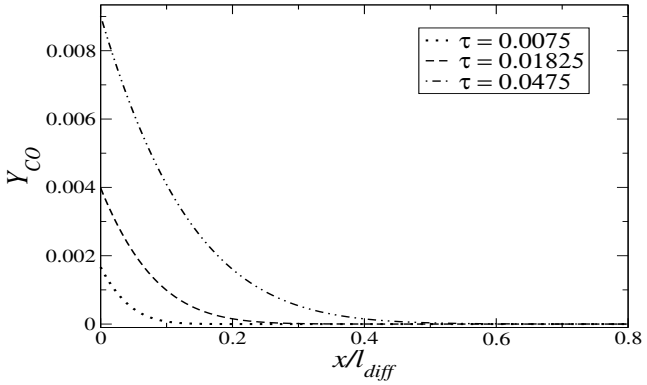

(C) Gas-phase CO profile

FIGURE 4.11: Evolution of the local wall temperature, gas-phase temperature and CO species profile during the endothermic phase

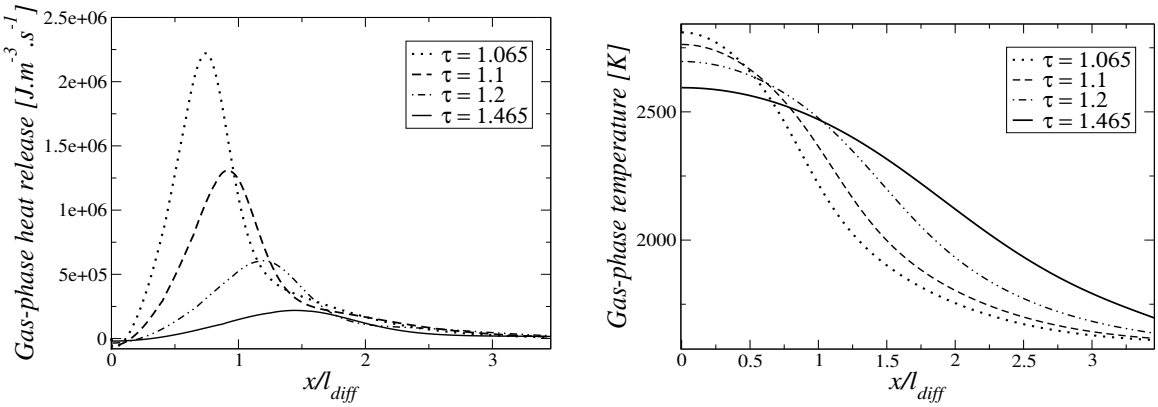

(A) Gas-phase heat release profiles

(B) Gas-phase temperature profiles

FIGURE 4.12: Gas-phase heat release and temperature profiles after surface carbon depletion

times during the phase where the reaction zone is detached from the wall. Unlike gas-phase temperature profile in Figure 4.9a that presents a peak, temperature profiles have a maximum at the wall resulting from the high temperature history of the phase during which the reaction zone was attached to the reactive wall. The heat-release is not high enough to induce a peak in the temperature profile.

As shown in Figure 4.12a, the heat release peak moves upward and decreases in amplitude with time. Indeed, at $\tau > 1.0$, CO diffuses in the whole domain and mixes with O_2 thus creating a partially premixed reactant field where the reaction zone propagates toward O_2-rich regions. The magnitude and the displacement velocity of the heat release profiles peak drop because the further the flame gets from the reactive wall, the less conducive are the conditions to sustain the gas-phase combustion. As described in Figure 4.13, CO concentration decreases as the distance to the wall increases, while rich O_2 regions do not compensate for CO diffusion limitation. The zones where $\dot{\omega}_T(x) \leq 0$ for a distance between 0 and $x/l_{diff} \approx 2.5$ (Figure 4.12a) result from O_2 dissociation into O radicals and CO_2 dissociation into CO and O described respectively by $R1$ and $R2$ given in Table 4.5.

According to the numerical results, heterogeneous carbon ignition through CO_2 and O_2 adsorption can be considered as instantaneous due to the high temperature and O_2 concentration. Under these extreme conditions, the resulting CO production and diffusion contribute to trigger the gas-phase combustion with O_2. During the competition between the heterogeneous and homogeneous reaction, the reaction zone is adjacent to the reactive wall. Carbon depletion leads to a propagation of the reaction front with a decreasing intensity away from the wall toward the channel zone that is less chemically limited .

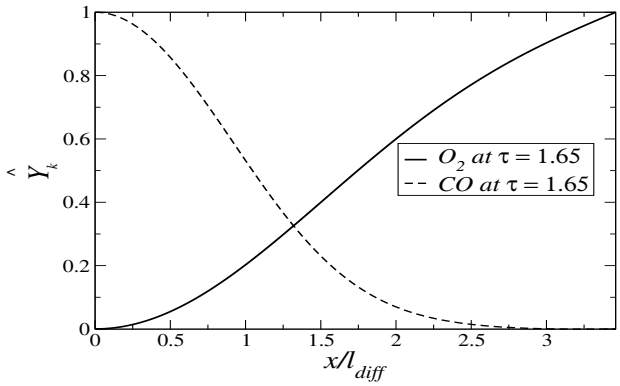

FIGURE 4.13: Spatial profiles of $\widehat{Y}_{O_2}$ and $\widehat{Y}_{CO}$

Model	Mole fraction and pressure gradients	*Soret*
Present modeling $\vec{V}_k$	*Hirschfelder & Curtiss* approximation	Neglected
a priori estimation $\vec{V}_k^{EGlib}$	$\sum_{j\in\Omega_G} D_{k,j}^{EGlib}\left(\vec{\nabla}X_j + (X_j - Y_j)\frac{\vec{\nabla}p}{p}\right)$	+ $\sum_{j\in\Omega_G} D_{k,j}^{EGlib}\left(\chi_j^{EGlib}\frac{\vec{\nabla}T}{T}\right)$

TABLE 4.6: Diffusion velocities used to calculate the mass fluxes $\rho Y_k \vec{V}_k$: Present modeling versus *a priori* estimation

Model	*Fourier*	Sensible enthalpy diffusion	*Dufour*
Present modeling $\vec{q}$	$-\lambda\vec{\nabla}T$ +	$\rho\sum_{k\in\Omega_G} h_{s,k}Y_k\vec{V}_k$	Neglected
a priori estimation $\vec{q}^{EGlib}$	$-\lambda^{EGlib}\vec{\nabla}T$ +	$\rho\sum_{k\in\Omega_G} h_{s,k}Y_k\vec{V}_k^{EGlib}$ +	$p\sum_{k\in\Omega_G}\chi_k^{EGlib}\vec{V}_k^{EGlib}$

TABLE 4.7: Diffusion heat fluxes: Present modeling versus *a priori* estimation

4.4 *a priori* evaluation of complex transport

Tables 4.6 , 4.7 summarize the differences between the modeling of our present simulation and the *a priori* estimated terms for heat and mass diffusion. In the case of multi-species flows, the diffusive velocity flux $\vec{J}_k$ are decomposed into several terms that consist in mole fraction, pressure and temperature (*Soret*) gradients, whereas the heat flux $\vec{q}$ includes temperature gradient, enthalpy transport through species diffusion and the *Dufour* term. In the present modeling, only mole fraction gradients are considered for the diffusive velocity flux through the *Hirschfelder & Curtiss* while the *Dufour* term is neglected in the heat flux. Therefore, the impact of the *Hirschfelder & Curtiss* approximation for the multi-species diffusion [30, 91] and the importance of the *Dufour* and *Soret* terms are assessed by post-processing the numerical data using

a complex transport library (EGlib library [77]). $D_{k,j}^{EGlib}$ represents the binary diffusion matrix, χ_j^{EGlib} correspond to the thermal diffusion ratios and λ^{EGlib} refers to the *a priori* assessed thermal conductivity coefficient.

Since the studied case is 1D, only components in the x direction (Figure 4.4) are plotted. Figure 4.14 shows the comparisons of the spatial profiles of the diffusion mass flux (*Soret* effect not included) and the *Soret* diffusion term for each gas-phase species during both reaction phases, i.e, wall-attached reaction zone phase and gas-phase reactions phase respectively at $\tau = 0.65$ and $\tau = 1.65$. Negative mass fluxes tend to compensate for low concentrations by diffusing toward the wall, whereas positive fluxes are due to species diffusing toward the outlet. Note that for all species the present mass diffusion model based on *Hirschfelder & Curtiss* approximation is always underestimated compared to the *a priori* EGLIB based mass diffusion. The pressure gradient being negligible in our case, this overestimation can be attributed to the hypothesis of constant *Schmidt* numbers used by our code to estimate non-binary mass diffusion coefficients. The relative error is around 5 percent which is fairly acceptable. Concerning the *Soret* effect which is not taken into account by our model, *a priori* calculations show that for CO_2 and O_2 species, the corresponding term is very small compared to mass diffusion in our case as shown by Figures 4.14a, 4.14b, 4.14c, 4.14d while it is negligible for CO species as given in Figures 4.14e, 4.14f. As a result, species concentration gradients play in our case a much more important role for species diffusion than the temperature gradient.

Heat fluxes linked to *Fourier*, sensible enthalpy diffusion and *Dufour* diffusion are also calculated *a priori* thanks to the EGlib library fed by the present modeling solution obtained under the *Hirschfelder & Curtiss* approximation. The estimation of the heat flux given by the EGLIB library enables to estimate the error related to the *Hirschfelder & Curtiss* approximation for species diffusion, moreover, the assumption of constant *Prandtl* numbers is made in our code to calculate the thermal conduction coefficient λ appearing in the *Fourier* diffusion term while the *Dufour* effect is not taken into account during the calculations. Hence, this section aims at verifying its importance.

Figure 4.15 compares the spatial profiles of sensible enthalpy diffusion, *Fourier* and *Dufour* diffusion for both reaction phases, i.e, wall-attached reaction phase and gas-phase reaction phase at $\tau = 0.65$ and $\tau = 1.65$. Regarding the sensible enthalpy transport through species diffusion, our modeling logically overestimates it since it overpredicts already the mass diffusion flux. The overestimation of the *Fourier* diffusion heat flux can be attributed to the hypothesis of constant *Prandtl* number used by our code to estimate thermal conductivity coefficient. Though, the relative error is around 6.5 percent which is satisfying. This analysis points out also that the *Fourier* and sensible enthalpy diffusion are of the same order of magnitude. Concerning the *Dufour* effect, which is not taken into account in our code, *a posteriori*

calculations show in our case that it is negligible as given in Figure 4.15. The system energy is thus much more sensitive to temperature gradients and species enthalpy diffusion than species diffusion.

4.5 Parametric study

A parametric study is carried out by varying initial O_2 and CO_2 concentrations. In order to characterize the effect of the initial ratio $(X_{O_2}/X_{CO_2})\mid_{t=0}$ on the combustion mode switch. Moreover, the influence on surface and gas-phase chemistry competition, i.e, $I_k(\tau) = 0.5$ is studied. Figure 4.16 shows the evolution of τ_{switch} and $\tau_{1/2,k}$ versus the molar ratio $(X_{O_2}/X_{CO_2})\mid_{t=0}$ for each species.

The parameters τ_{switch} and $\tau_{1/2,k}$ stand respectively for the physical time corresponding to the combustion mode switch and the physical time below which $I_k \leqslant 0.5$ both normalized by their values for the reference case corresponding initially to $X_{O_2} = 0.7$, i.e, $(X_{O_2}/X_{CO_2})\mid_{t=0}= 2.33$. As O_2 initial concentration increases, exothermic surface oxidation is enhanced which increases carbon combustion rate thus resulting in a decrease of τ_{switch} as the $(X_{O_2}/X_{CO_2})\mid_{t=0}$ ratio increases. $\tau_{1/2,O_2}$ then rises because richer O_2 mixtures favor surface oxidation reactions (Table 4.4, reactions S1 to S3) which in turn enhances the surface rate $\dot{s}_{O_2}$. As a consequence, the competition between O_2 adsorption by surface carbon and its consumption by the gas-phase combustion is extended to a wider time range.
On the contrary, as the initial molar ratio $(X_{O_2}/X_{CO_2})\mid_{t=0}$ is increased, $\tau_{1/2,CO_2}$ drops because less CO_2 species is available for surface gasification reaction (Table 4.4 reactions $S4$) which reduces the surface rate $\dot{s}_{CO_2}$. The resulting competition between CO_2 consumption by the reactive surface and its production through gas-phase combustion becomes shorter.

4.6 Grid convergence

A global criterion was written in order to estimate the proper grid resolution in the near-wall region. The criterion gave a cell height of $h_{min} = 15\mu m$ and was established according to the following equality : $dt_{schem,min} \approx dt_{Fo,min}$. With $dt_{Fo,min} = Fo\left(h_{min}^2/\nu\right)$.
The resulting minimum cell height is $h_{min} = \sqrt{(\nu/Fo)\, dt_{schem,min}}$. $dt_{schem} = min\left(\dfrac{\Gamma W_k}{\dot{s}_k}\right)$ corresponds to the minimum surface chemistry time step estimated thanks to homogeneous calculations and $dt_{Fo,min}$ is an *a priori* estimation of the diffusive minimum time step which is the limiting time step in

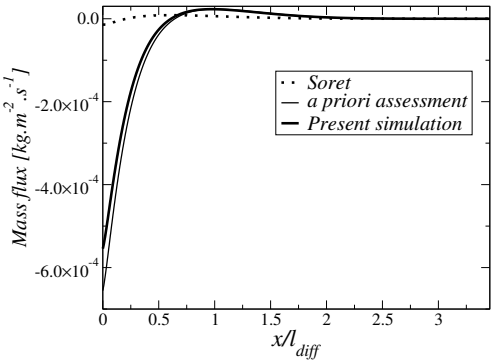

(A) Mass fluxes for CO_2 species

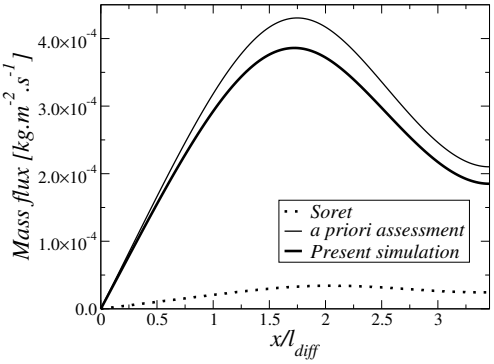

(B) Mass fluxes for CO_2 species

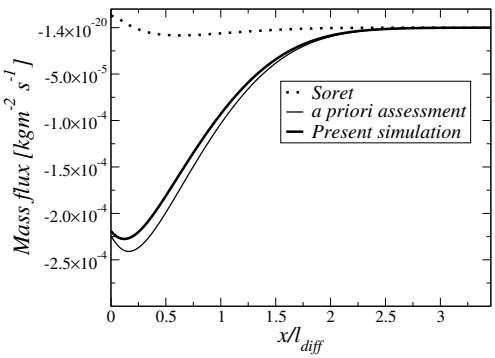

(C) Mass fluxes for O_2 species

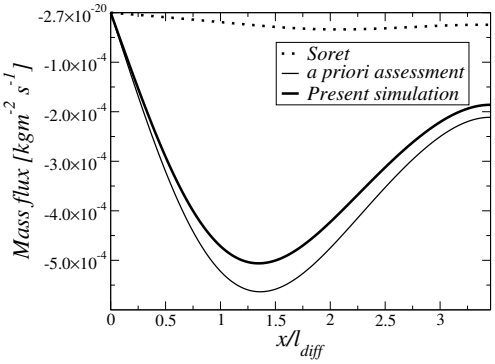

(D) Mass fluxes for O_2 species

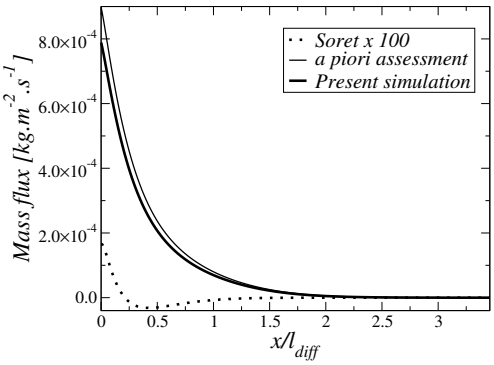

(E) Mass fluxes for CO species

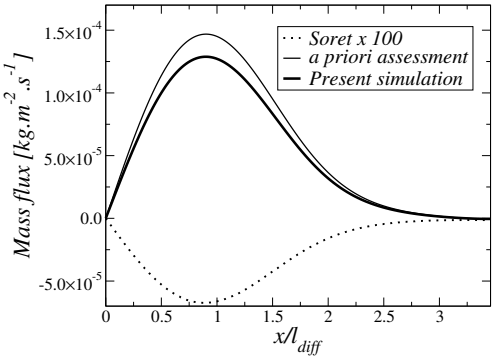

(F) Mass fluxes for CO species

FIGURE 4.14: Comparison of *a priori* assessment versus the present simulation : *Soret* term versus diffusion induced by molar fraction and pressure gradients at $\tau = 0.65$ (left) and $\tau = 1.65$ (right)

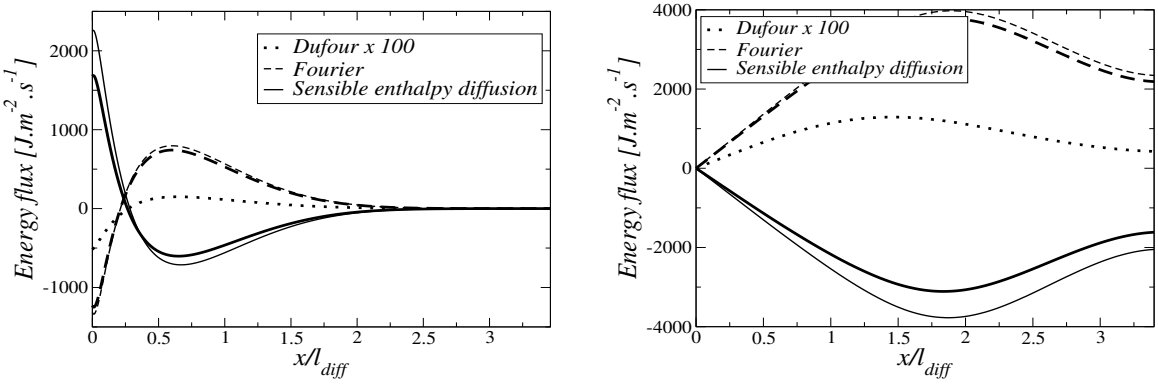

(A) Energy fluxes at $\tau = 0.65$

(B) Energy fluxes at $\tau = 1.65$

FIGURE 4.15: Comparison of *a priori* assessment (thin lines) versus the present simulation (thick lines).

our case. A constant grid resolution was applied for the diffusive length with a cell height corresponding to h_{min} and a mesh coarsening has been carried out between $x/l_{diff} = 0.865$ and the outlet. Nevertheless, a grid convergence was necessary to determine properly the mesh size. The grid convergence was performed for 4 different meshes by solely varying the diffusive length mesh size between $h_{min} = 15\mu m$ and $h_{min} = 5\mu m$. Figure 4.17 shows near-wall gradients of CO_2 species mass fractions and gas-phase temperature at a time where gradients are strongest, i.e, at $\tau = 0.955$. It shows that the grid convergence was reached at $7\mu m$. The relative differences between the $7\mu m$ grid resolution and the present mesh of $10\mu m$ are around 0.1% only. Therefore, the $10\mu m$ resolution was chosen because it is judged fine enough to resolve the stiffest gradients at the reactive wall and the gas-phase reaction zone thickness with reasonable numerical limiting time steps.

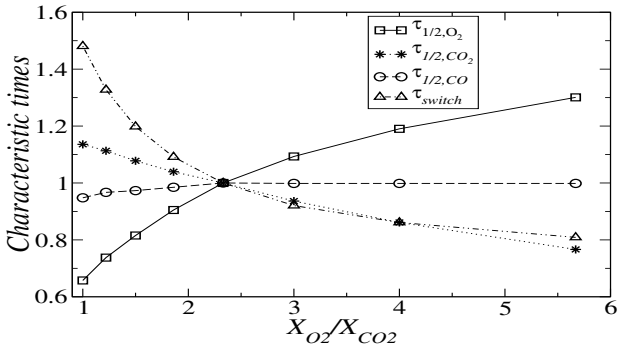

FIGURE 4.16: Characteristic times versus initial molar ratio $(X_{O_2}/X_{CO_2})\ |_{t=0}$. The case $(X_{O_2}/X_{CO_2})\ |_{t=0}= 2.33$ is taken as a reference

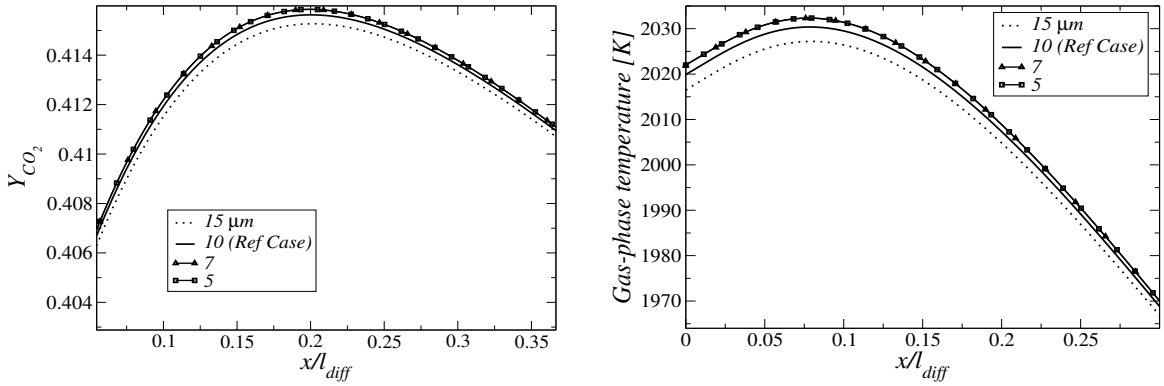

(A) Gas-phase CO_2 species mass fraction profiles

(B) Gas-phase temperature profiles

FIGURE 4.17: Grid convergence for four different near wall resolutions at $\tau = 0.955$

4.7 Conclusions

A boundary condition for the impact of surface reactions on the heat flux at the reactive wall was applied. An original analytical solution developed has been derived by Cabrit *et al.* for a flow bounded by two reactive surfaces. A special attention has been given to the numerical setup so that compatibility with a steady-state is achieved. This approach enables to compare analytical solutions with stationary numerical predictions thus validating numerical species boundary condition for the heterogeneous surface reactions.

Numerical simulation accounting for multi-species diffusion and micro-kinetics taking into account the *Stefan* flux were subsequently performed to study carbonaceous wall combustion under oxy-fuel conditions. Transition from endothermic gasification to surface carbon oxidation and gas-phase ignition were evidenced thanks to the analysis of the time-dependent surface and gas-phase species production rates and transient histories of surface species concentrations as well as spatial profiles of gas-phase species, heat release and temperature. The reference case that consists in a quiescent mixture containing 70 percent of O_2 and 30 percent of CO_2 in volume is characterized by two gas-phase reaction zone configurations. The first one corresponds to a wall-adjacent CO-reaction zone maintained by the competition between the CO/O_2 combustion and surface reactions. CO surface desorption contributes to the continuous feeding of the reaction zone which in turn produces CO_2 that diffuses to the surface and adsorbs on surface carbon thus providing an additional CO formation pathway. Once carbon has been totally consumed the reaction zone moves toward the outlet while its intensity is progressively dumped. Therefore, there is a strong interaction between the surface and gas-phase kinetics depending on the chemical conditions. Note that this reaction zone occurring at a certain distance of the reactive wall is observed despite the absence of volatiles in the gas-phase.

The impact of the *Hirschfelder & Curtiss* approximation for the multi-species diffusion and the importance of the *Dufour* and *Soret* terms were assessed by post-processing the numerical data thanks to a complex transport library (EGlib library). *A priori* post-processing of the present simulation showed that species concentration gradients have a much more important contribution to the diffusion velocity than the temperature gradient (*Soret* effect) whereas the system energy is much more sensitive to temperature gradients (*Fourier*) and sensible enthalpy diffusion that are of the same order of magnitude. The *Dufour* effect being also negligible, the *Hirschfelder & Curtiss* approximation is satisfying since the relative error between the fluxes predicted by the present modeling and the ones estimated by the EGLIB library is around 6 percent. The discrepancies can be attributed to the hypothesis of constant *Schmidt* and *Prandtl* numbers used to estimate non-binary mass diffusion coefficients and thermal conduction coefficient respectively.

Eventually, the effect of initial concentrations of O_2 and CO_2 on characteristic times of gas and surface reactions and times corresponding to the switch between the two gas-phase reactions structures has been assessed. As the $(X_{O_2}/X_{CO_2})\mid_{t=0}$ ratio increases, the switch between the two modes of gas-phase reactions occurs earlier and the competition between CO_2 consumption by the reactive surface and its production through gas-phase combustion becomes shorter. In contrast, the surface consumption of O_2 was seen to compete gas-phase combustion for a wider time range.

Chapter 5

2D simulation of catalytic combustion in a meso-scale planar channel

introduction

The approach developed in the present work accounting for gas-phase and surface chemistry was verified as described in Chapter 2 and 3 using homogeneous reactor calculations. It was in particular shown that the boundary conditions predicted properly the time evolution of species and temperature. In the Chapter 4, both boundary conditions for momentum and mass transfer were validated by comparing the results of 1D numerical simulations with analytical solutions. Nonetheless, the assumption of neglecting gas-phase reactions was made to simplify the derivation.

Therefore, 2D simulation of gas-phase combustion of a lean premixed CH_4/air mixture in a catalytic meso-scale channel with planar walls are presented in this Chapter. First, numerical results are compared to experimental data provided at steady-state by Dogwiler *et al.* [27] for validation. Second, a transient analysis is carried out to provide insight into the ignition dynamics encountered within catalytic channels. Finally, the stabilizing effect of the catalytic walls on gas-phase combustion is emphasized by numerically deactivating surface reactions.

It should be stressed that the experimental set-up of Dogwiler *et al.* [27] was relevant for gas-turbines applications using CST (Catalytically Stabilized Thermal combustion) [14]. Although the configuration is not strictly representative of monolithic channels encountered in automotive catalytic converters, the experiment provides valuable data for the validation of the present modeling.

The structure of the present Chapter is as follows:

- The experimental setup of Dogwiler *et al.* [27] is briefly depicted in Section 5.1 at first.
- The numerical methodology and modeling assumptions are provided in Section 5.2.
- In Section 5.3, validations are carried out at steady-state for different inlet conditions by comparing numerical results with experimental data.
- Section 5.4 is dedicated to the investigation of the possible sources of discrepancies.
- The transient dynamic of heterogeneous chemistry is analyzed in Section 5.5.
- In Section 5.7, stability effects of surface reactions are highlighted.

5.1 Experimental configuration

The data used to validate our numerical simulations are taken from the study of Dogwiler *et al.* [27]. They experimentally investigated the gas-phase ignition of lean premixed methane-air mixtures in a planar channel flow configuration with Pt coated interior walls. Figure 5.1[1] respectively shows schematics of the optical arrangement (Fig 5.1a) and the central planar (Fig 5.1b) of the experimental set-up. It has been widely used in several campaigns. Only the main features are given here. For further details, please refer to [27, 92–95] :

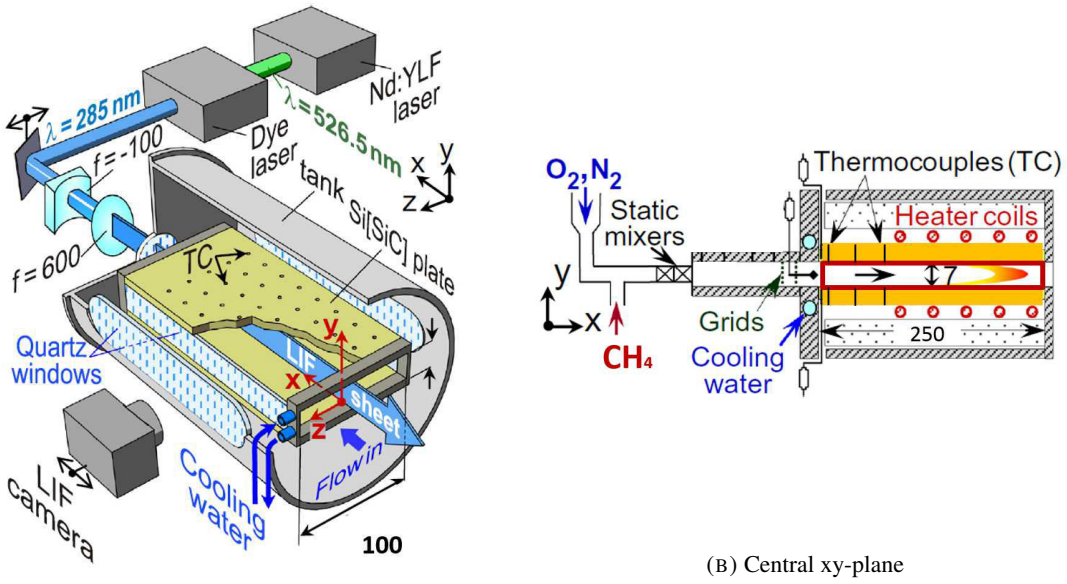

(A) Optical arrangement

(B) Central xy-plane

FIGURE 5.1: Schematics of the experimental set-up of Dogwiler *et al.*. All distances are in mm. TC stands for thermocouples.

- As shown in Figure 5.1a, the reactor is rectangular and consists of two 250 mm long (x-direction) and 100 mm wide (z-direction) ceramic plates that are placed 7 mm apart (y-direction).
- The horizontal ceramic plates are highlighted by orange rectangles in Figure 5.1b. The inner surfaces of the ceramic plates were made catalytically active thanks to a 2 μm thick Pt-layer sputtering. The Pt-coating was performed allover their length and width ($0 \leq x \leq 250$ mm and -50 mm $\leq z \leq$ +50 mm with $z = 0$ denoting the xy symmetry plane). Lateral walls of the channel ($z = \pm 50mm$) were left chemically inert.

[1] *Images were taken from Brambilla et al. [92]. Although, the catalytic plates are 50 mm longer and 4 mm wider, the experimental set-up is similar, as pointed out by Mantzaras in [6]*

- The temperature of the catalytic walls was controlled and monitored in the experiment thanks to a heating/cooling arrangement. Longitudinal wall temperature profiles, ranging from 1280 K to 1365 K, could be achieved.
- The preheated CH_4/air mixture was introduced into the channel from the left side with respect to Figure 5.1b. In order to ensure nearly uniform entry flow velocity and temperature, the mixture flowed through a straightening system placed upstream of the channel entrance.
- The flow is laminar with inlet Reynolds numbers (based on the 7-mm channel height) up to 390. The reactor operated under atmospheric conditions.
- OH-LIF was performed to measure the levels of hydroxyl radical (OH) resulting from the gas-phase reactions. 2D maps of the OH molar concentration are provided in the xy symmetry plane (Figure 5.1a). Measurements of spatial profiles of OH concentration are available as well, along the channel center-line ($y = 3.5$ mm and $z = 0$).

5.2 Methodology and modeling assumptions

5.2.1 Domain of interest and boundary conditions

The 2D domain of interest for the present simulations is highlighted by a red rectangle shown in Figure 5.1b. The devices present in the experiments and located upstream the highlighted box were not included in the simulations. Figure 5.2 shows the resulting 2D computational domain, that was chosen to be symmetric with respect to the channel half-height (y-direction). The justification for this simplifying assumption will be discussed in Section 5.7.

The region emphasized in red is the lower part of the domain of interest shown in Figure 5.1b, with a Pt-coated planar catalytic wall located at $y = 0$. The two blue regions located up-and downstream the domain of interest were added for numerical reasons: The convergent located upstream the line $x = 0$, enables to yield nearly uniform inlet velocity and temperature profiles at $x = 0$, as in the experiment. The divergent located downstream the domain of interest was added in order to achieve imposing atmospheric pressure at the right end of the domain of interest located at $x = L_c + L_{PO}$, while at the same time, avoiding non-physical reflexions resulting from flow perturbations reaching the outflow of the computational domain.

Since the catalytic plates are 100 mm wide (i.e. in the z-direction shown in Figure 5.1a), which is more than ten times the channel height (H), the reactor is considered wide enough so that the flow between

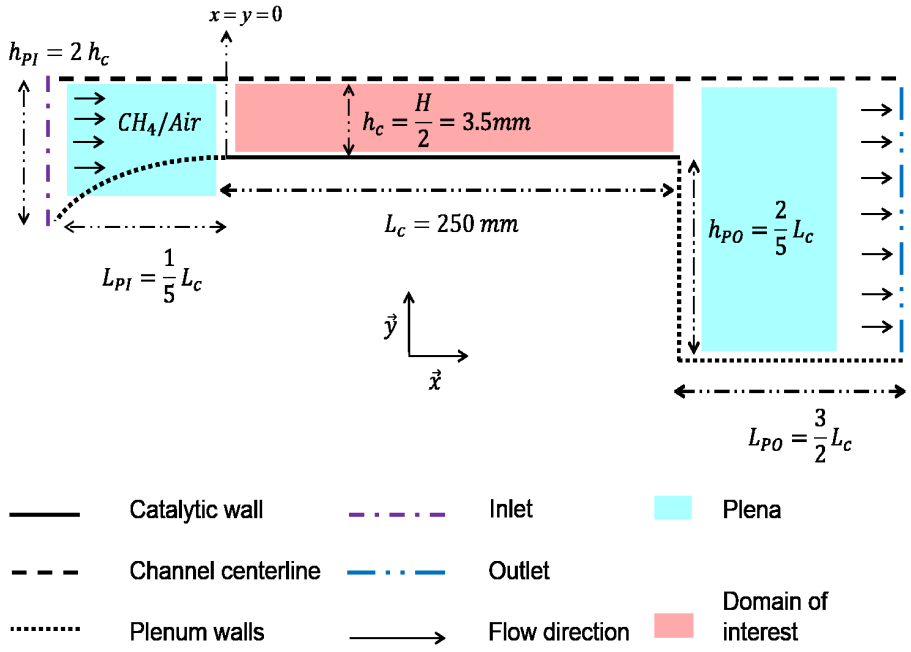

FIGURE 5.2: Numerical setup of the catalytic channel. Plena are added for the numerical imposition of I/O boundary conditions.

the catalytic plates can be considered as two-dimensional. These observations justify the 2D assumption made to model the experiment.

As shown in Table 5.1, Dogwiler *et al.* [27] studied three different cases (labelled in what follows as (a), (b) and (c)) by varying the inlet the velocity, temperature and equivalence ratio while the pressure and wall temperature were kept constant. Table 5.2 shows the different types of boundary conditions used in the present study with the corresponding imposed scalars or fluxes.

Case	ϕ	$Y_{CH_4}\|_{inlet}$	$Y_{O_2}\|_{inlet}$	$Y_{N_2}\|_{inlet}$	$(u_x)\|_{inlet}[m \cdot s^{-1}]$	$T_{inlet}[K]$	R_e	$P[atm]$
a	0.37	0.021	0.228	0.751	1	750	186	1
b	0.37	0.021	0.228	0.751	2	729	390	1
c	0.31	0.018	0.229	0.753	1	754	186	1

TABLE 5.1: Inlet conditions for each case. ϕ, $(U_x)|_{inlet}$ and T_{inlet} respectively stand for the equivalence ratio, axial velocity and temperature of the incoming mixture. $Y_{CH_4}|_{inlet}$, $Y_{O_2}|_{inlet}$ and $Y_{N_2}|_{inlet}$ respectively refer to the CH_4, O_2 and N_2 species mass fractions at the inlet. R_e denotes the inlet Reynolds number based on the inlet velocity and channel height (H)

Inlet and outlet boundary conditions are respectively applied to the convergent entrance ($x = -L_{PI}$) and divergent exit ($x = L_c + L_{PO}$) using the NSCBC method [78, 79]. The temperature (T_{inlet}), species mass fractions ($Y_{CH_4}|_{inlet}$, $Y_{O_2}|_{inlet}$ and $Y_{N_2}|_{inlet}$) and velocity ($\vec{u}|_{inlet}$) are prescribed at the inlet. The velocity

Boundary	Numerical condition	Imposed scalars or fluxes
Inlet	Inlet NSBC [78, 79]	Y_k, T and $\vec{u}$
Outelt	Outlet NSCBC [78, 79]	P
Catalytic wall	Isothermal reactive (Eq. 5.1)	T, $\vec{u}\cdot\vec{n}$ and $\vec{\nabla}Y_{k,w}\cdot\vec{n}$
Plena walls	Adiabatic and free-slip	$\vec{u}\cdot\vec{n}$ and $\vec{q}\cdot\vec{n}$
Channel centerline	Symmetry	No imposition.

TABLE 5.2: Type of boundary conditions used for the present study with the corresponding imposed scalars or fluxes.

imposed at the inlet boundary is calculated in order to reproduce the mass flow rate from the experiment with respect to mass conservation, i.e, $u_x|_{inlet}\times(h_c/h_{PI})$ is imposed at the convergent entrance. Pressure is the only enforced value at the outlet boundary as it remains subsonic. The NSCBC method relaxes the values predicted by the numerical scheme toward the targeted conditions in order to control possible reflections of the waves thus avoiding the propagation of non-physical perturbations.

In order to render the fact that the temperature of the catalytic walls was controlled and monitored in the experiments, an iso-thermal boundary condition was numerically imposed using the longitudinal experimental temperature profile experimentally measured and shown in Figure 5.3. The wall temperature profile is enforced by the means of a conservative relaxation method which relaxes the temperature predicted by the numerical scheme at the wall toward the targeted temperature profile.

The effect of surface reactions on the mass and momentum fluxes at the wall, is taken into account by respectively prescribing, at the catalytic wall, the expressions of Eq. (5.1) to the gas-phase species mass fraction gradients and velocity. The predicted fluxes at the wall are then corrected using the definitions of Eq. (5.1) with respect to the weak formulations indicated in Eqs. (3.54-56). Standard free-slip and adiabatic wall conditions are applied to the walls of the plena. Also, during the non-reactive computations performed to establish the flow, standard impermeable wall conditions are used for the catalytic wall.

$$\begin{cases} \vec{\nabla}Y_{k,w}^{BC}\cdot\vec{n}^g = \dfrac{Y_{k,w}}{D_k\rho_w}\displaystyle\sum_{l\in\Omega_G}\dot{s}_l + \dfrac{Y_{k,w}}{D_k}\vec{V}_w^{correc}\cdot\vec{n}^g + Y_{k,w}W_w\left(\sum_{l\in\Omega_{gas}}\dfrac{1}{W_l}\vec{\nabla}Y_{k,w}\cdot\vec{n}^g\right) \\ \quad -\dfrac{\dot{s}_k}{\rho_w D_k} \\ \rho U_{Stefan} = \left(\displaystyle\sum_{k\in\Omega_G}\dot{s}_k\right) \end{cases} \tag{5.1}$$

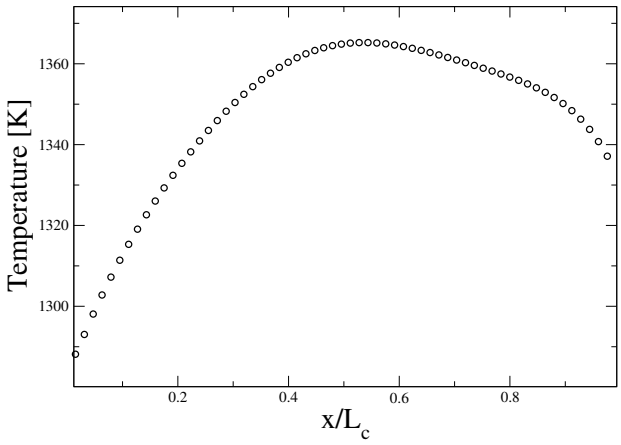

FIGURE 5.3: Experimental wall temperature profile used to impose the iso-thermal wall condition on the catalytic wall.

5.2.2 Calculation strategy

Figure 5.4 illustrates the calculation strategy followed for the present simulations. It comprises the following steps:

- First, the non-reactive steady flow is established by running with switched off chemical reactions during a physical time τ_{init} ranging from 0.125 s to 0.25 s, that corresponds to one flow through time. The flow field is initialized using simple homogeneous solutions which are depicted in Table 5.3.
- Restarting from the obtained steady chemically inert flow, chemistry is then numerically switched on (except in the plena), and the simulation is run for a physical time $\tau_{reac} = 115$ ms, that is long enough to cover all the phases of the transient combustion described below.

Variables	$T(x,y)$ [K]	$u_x(x,y)$ $[m \cdot s^-1]$	$u_y(x,y)$ $[m \cdot s^-1]$	$P[atm]$	$\theta_{O(Pt)}$	$Y_k(x,y)$
Values at $t = 0$	$T_{wall}(x)$	0	0	1	1.0	$Y_k\|_{inlet}$

TABLE 5.3: Initial solution for the non-reactive computations. $T_{wall}(x)$ stands for the wall temperature profile plotted in Figure 5.3. $\theta_{O(Pt)}$ refers to the site fraction of the adsorbed O species by the P_t active sites.

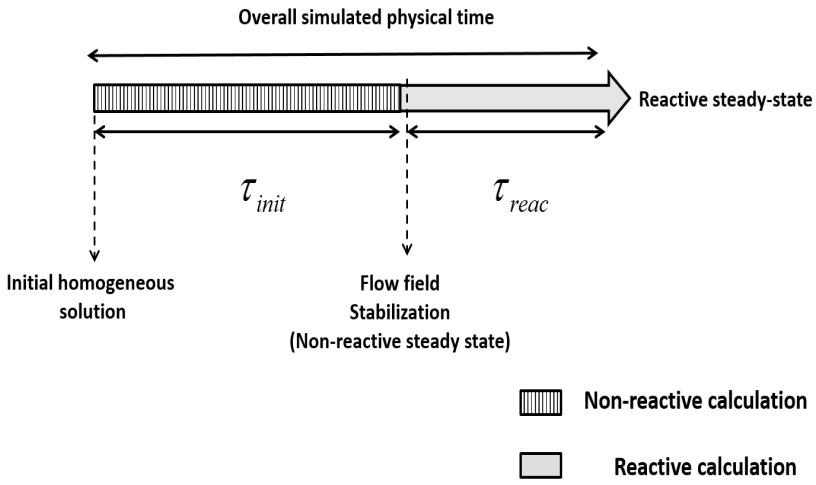

FIGURE 5.4: Illustration of the calculation methodology

5.2.3 Meshing strategy

Two grid resolutions are adopted. The first coarser grid is dedicated to the establishment of the flow field under non-reactive conditions. The second grid is refined and adjusted in order to adapt to chemical and surface reactions.

Establishment of the flow field:
As indicated in Table 5.4, the domain of interest highlighted in red in Figure 5.1b is descretized using a triangular mesh with 15 cells in the height and 1000 cells in the length. The mesh is significantly coarsened in both plena because they do not belong to the domain of interest.

Grid	Discretization	Grid size
$\triangle x$	$L_c/1000$	250 μm
$\triangle y$	$h_c/15$	233 μm

TABLE 5.4: Grid resolution used to establish the flow field in the domain of interest.

Reactive cases:
A meshing strategy is adopted for the following reasons :

- The transverse resolution is difficult to define *a priori* because no proper criterion was derived in literature when surface chemistry is active. As will be shown in Section 5.7, transverse effects

of surface reactions are necessary to stabilize the flame under the present conditions. Hence, 1D flame calculations that would allow to *a priori* estimate the longitudinal grid resolution could not be properly achieved because transverse effects are complicated to account for in one-dimensional modeling [96–98].

- Table 5.5 provides *a priori* estimations of the time steps due to the different involved phenomena. It is shown that the acoustic time step is limiting when the grid resolution of the non-reactive case is used. Since chemical time steps do not *a priori* depend on the mesh size, acoustic and diffusive time steps are the most likely to be limiting if a finer mesh is used. Giving the fact that the code is explicit, carrying out a full transient calculation with a mesh-dependent time step would lead to a tremendous CPU cost. The estimations given in Table 5.5 are *a posteriori* verified as will be shown in Section 5.6.

Phenomenon	Convection/Acoustics	Diffusion	Gas-phase chemistry	Surface chemistry
Notation	dt_{CFL}	dt_{Fo}	dt_{chem}^{Gas}	dt_{chem}^{Surf}
Expression	$CFL\frac{\triangle x}{\|\|\vec{u}\|\|+\|c\|}$	$dt_{F_o}=F_o\frac{(\triangle x)^2}{\nu}$	$min\left[\frac{\rho}{\dot{\omega}_k}\right]$	$min\left[\frac{\Gamma W_k}{\dot{s}_k}\right]$
Estimation	$\approx 1\times10^{-7}$	$\approx 5\times10^{-5}$	$\approx 1\times10^{-5}$	$\approx 1\times10^{-5}$

TABLE 5.5: *a priori* estimations of the time steps. dt_{Fo} and dt_{CFL} are estimated using a cell size equal to $h_c/15 = 230$ μm. Fourier (Fo) and CFL numbers are respectively equal to 0.1 and 0.7. c refers to the sound speed. Gas-phase and surface chemistry time steps are estimated using homogeneous reactor calculations performed under the present conditions. Γ is the P_t site density.

As the mesh resolution could not be *a priori* set, it was *a posteori* checked so that it resolves the gas-phase reaction front on at least 10 and 6 nodes in the axial and transverse directions respectively. Two different mesh resolutions (labelled MESH (I) and MESH (II) in what follows) were used to ensure a sufficient spatial resolution of the reaction zone in the different phases of the transient ignition and stabilization processes :

The overall meshing strategy is summarized in Figure 5.5. Mesh (I) presents the finest resolution and could be exclusively used since it should capture all the variations of the gas-phase reaction zone. However, it is only used to resolve the stiffest dynamics coinciding with the activation of both gas-phase and surface reactions. Once the gas-phase reaction zone becomes thick enough to be resolved on a coarser mesh, i.e. at a physical time approximately equal to 3 times the ignition time (t_{interp}), variables are interpolated to mesh (II) which is dedicated to the stabilization process. The steady-state can therefore be reached with an affordable CPU cost as will be shown in Section 5.6.

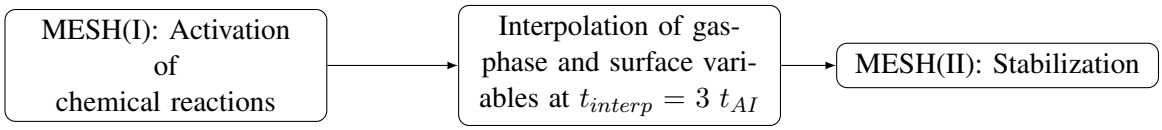

FIGURE 5.5: Summary of the meshing strategy, t_{interp} and t_{AI} respectively stand for the interpolation time and the physical time at which chemical reactions are activated.

Table 5.6 gives the grid size used for both meshes and the reaction front thickness to local grid size ratio. The thickness of the gas-phase reaction front is noted L_f and is taken as the thickness of the longitudinal profile (x-direction) of the gas-phase heat-release at the channel center-line ($y = 3.5$ mm).

Mesh Notation	$\triangle x(\mu m)$	$\triangle y(\mu m)$	$L_f/\triangle x$	$L_f/\triangle y$
Mesh (I)	25	25	$10 \leq L_f/\triangle x \leq 30$	$10 \leq L_f/\triangle y \leq 30$
Mesh (II)	250	230	$L_f/\triangle x = 6$	$L_f/\triangle y = 6.5$

TABLE 5.6: Grid resolutions used for the reactive cases.

5.2.4 Chemical schemes and their resolution

For gas-phase chemistry, the Saudi Aramco mechanism 1.3 (Aramco Mech 1.3) [42, 43] was chosen. It addresses the oxidation kinetics of hydrocarbon and oxygenated fuels using 250 species and more than a thousand of reactions. As solving such a large scheme in our simulations would yield unpractical CPU times, a reduced skeletal scheme was formulated that would render accurately the chemistry found under the conditions of Dogwiler *et.al* [27].

As combustion of CH_4 is considered, $C3/C4$ based hydrocarbon species are first suppressed so that only $C1/C2$ chemistry is kept. Second, an Error-Propagation based Direct Relation Graph (DRGEP) methodology [99] is adopted under the conditions of interest resulting in a skeletal mechanism that includes 39 bidirectional and 1 unidirectional reactions, involving 16 species.

Regarding surface reactions, the reaction mechanism of Deutschmann *et al.* [22, 48] is employed. It uses 21 bidirectional and 3 unidirectional reactions with 7 gas-phase and 10 surface species involved. Platinum species (Pt) refers to the catalytic active sites while 9 other surface species represent the species adsorbed by P_t or resulting from surface-to-surface reactions. The catalyst site density (Γ) is taken equal to $2.72 \times 10^{-5}\ cm^2 \cdot mol^{-1}$ simulating a polycrystalline platinum surface which is most likely to resemble to the experimental catalytic coating site density according to Dogwiler *et al.*[27]. The mechanism is provided with the thermochemical data needed to calculate the equilibrium constants for the 3 bidirectional reaction constants.

Table 5.7 summarizes the modeling of chemical reactions with the associated time integration methods used in the present study. The time integration method of chemistry is chosen with respect to the stiffness features of the kinetic mechanisms:

- Gas-phase chemistry is solved using a simple explicit 1^{st} order Euler method because the limiting time step of the CFD simulation is small enough to ensure stability of the time integration method;
- Surface chemistry kinetics was found to be stiff and could only be handled by using an implicit solver. The VODE [40] solver is chosen because it requires shorter CPU times than the other implicit solvers.

Chemistry	Mechanism	Number of reactions	Number of species	Integration method
Gas-phase	Reduced Aramco Mech 1.3	39 bidirectional & 1 unidirectional	16	Explicit 1^{st} order Euler
Catalytic wall	Deutschmann *et al.* [22, 48]	21 bidirectional & 3 unidirectional	7 gas-phase & 10 surface species	Implicit VODE

TABLE 5.7: Features of the gas-phase and surface mechanisms used for the present study

5.3 Validation of the steady-state solutions

The steady-state solutions obtained for the 3 cases (a),(b) and (c) are validated by comparing the numerical results with the experimental data by Dogwiler *et al.* [27]. Figures 5.6 to 5.8 compare 2D OH-PLIF measurements with the computed 2D maps of OH concentration for the three cases. Similar flame shapes are obtained: The symmetric "V" shapes and the sweep angles are reproduced in an acceptable manner for all cases by the present numerical modeling. The V-flames are due to lower axial velocities at the catalytic wall which results in a penetration of the flame further upstream in the vicinity of the wall.

Comparable predictions of the positions where the flames are stabilized and levels of OH concentration are noticed as well. The flame of case (b) stabilizes further downstream and is more stretched because the inlet velocity is two times higher. OH concentration of case (c) presents lower levels than cases (a) and (b) because of a leaner inlet mixture. Although, predicted flame wakes are more spread with higher OH concentration levels at the flame center.

In order to quantify the axial stabilization of the flames, Table 5.8 compares the axial distance from the inlet of the catalytic channel and the axial point where the OH concentration reaches its maximum. The

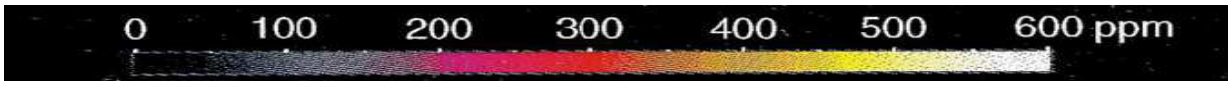

Experimental

(A)

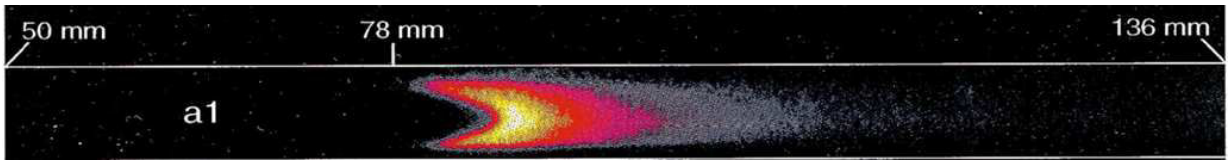

Modeling

(B)

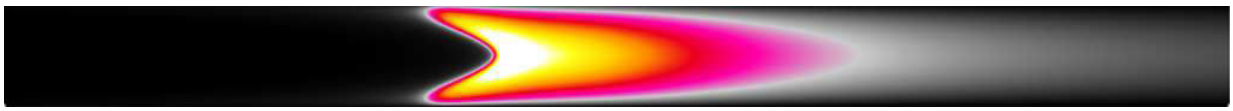

FIGURE 5.6: 2D OH concentration maps for case (a)

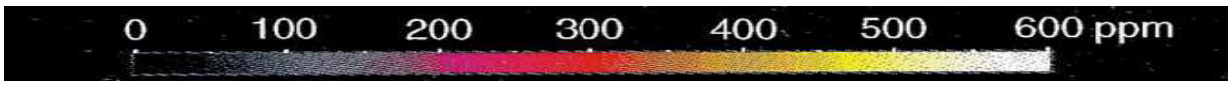

Experimental

(A)

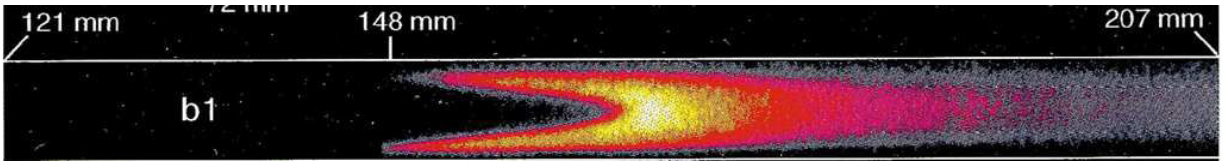

Modeling

(B)

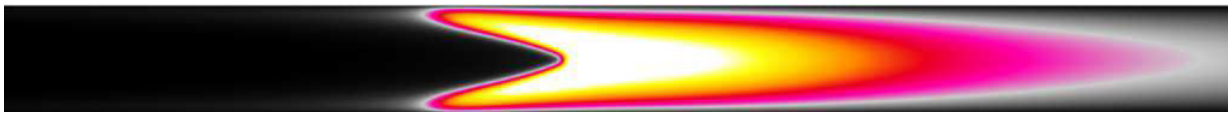

FIGURE 5.7: 2D OH concentration maps for case (b)

relative differences for all cases are smaller than 3%, thus validating the accuracy of the presented simulation approach for the steady state-conditions. The normalized error indicates that the order of magnitude of the error is equivalent to one channel half-height (h_c) for cases (b) and (c).

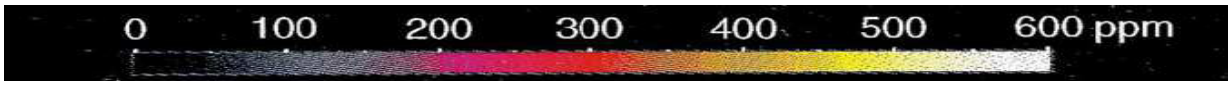

Experimental

(A)

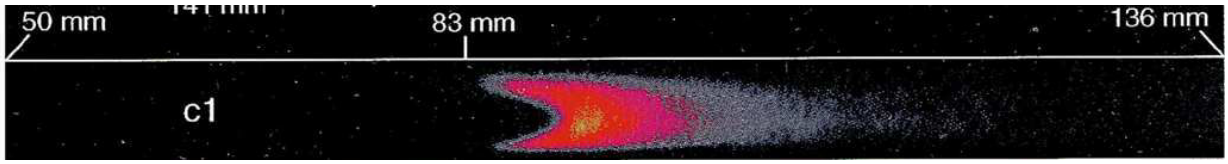

Modeling

(B)

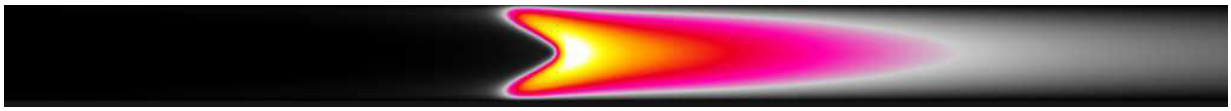

FIGURE 5.8: 2D OH concentration maps for case (c)

Case	x_{stab}^{exp}[mm]	x_{stab}^{num} [mm]	Relative difference (%)	$\frac{\lvert x_{stab}^{exp} - x_{stab}^{num} \rvert}{h_c}$
a	86.25	86.1	0.2	0.04
b	162.5	166.8	2.5	1.23
c	91.5	90.35	1	0.33

TABLE 5.8: Comparison of the predicted stabilization positions of the flames (x_{stab}^{num}) with the experiment (x_{stab}^{exp}). $\frac{\lvert x_{stab}^{exp} - x_{stab}^{num} \rvert}{h_c}$ is the normalized error.

Figure 5.9 compares the computed axial OH-profiles on the channel center-line with experimental findings. Table 5.9 gives the error made by the numerical modeling in predicting OH concentration with respect to the spatial profiles plotted in Figure 5.9. The discrepancies are quantified by comparing the OH peaks and the thickness of OH profiles, noted L_{OH}. It is defined as the distance between the two highest profile gradients.

The error made regarding the maximum OH levels is globally around 50% whereas the order of magnitude of the discrepancies of L_{OH} approximately corresponds to 3 times the channel half-height.

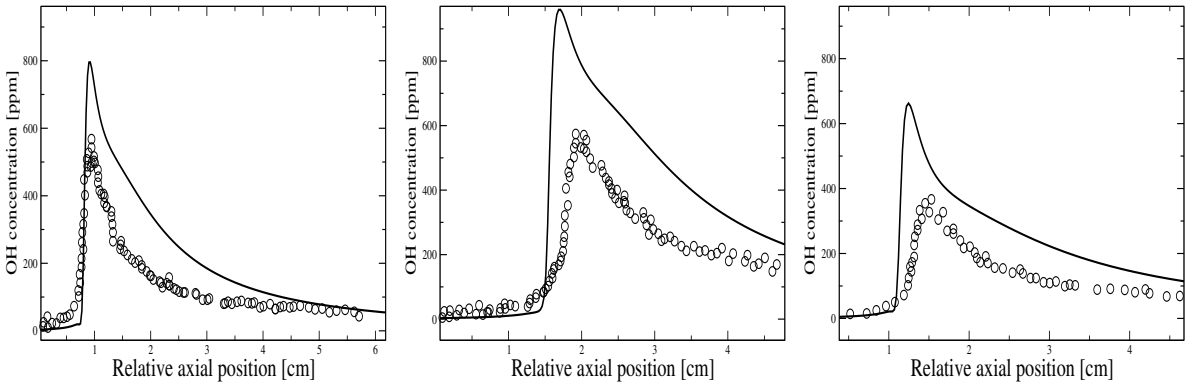

(A) Case (a) (B) Case (b) (C) Case (c)

FIGURE 5.9: Comparison of axial OH profiles along the channel center-line for cases (a, b, c). Symbols : Experiments. Lines : Calculations

Case	Relative difference of maximum axial OH levels (%)	Relative difference of OH profile thickness (%)	$\frac{\lvert L_{OH}^{exp} - L_{OH}^{num} \rvert}{/h_c}$
a	38	25	2.95
b	62	30	2.25
c	75	15	3.2

TABLE 5.9: Comparison of the predicted maximum OH levels and flame thickness with the experiment. L_{OH}^{exp} and L_{OH}^{num} respectively refer to the experimental and predicted values.

5.4 Investigation of the possible sources of discrepancies

The influence of non-chemical parameters and modeling assumptions is investigated in what follows to identify source of errors for case (a) only :

5.4.1 Effect of wall temperature and inlet conditions

The wall temperature and inlet conditions are subject to measurement uncertainties. Figure 5.10 shows the sensitivity of axial OH profiles along the channel center-line to a $\pm 10\%$ variation of the inlet temperature, inlet equivalence ratio and wall temperature.

Uncertainties on the equivalence ratio have a negligible impact on the OH profile, whereas uncertainties in both inlet and wall temperature noticeably impact the flame position and OH peaks. Although, OH peaks are more sensitive to wall temperature uncertainties. As the flame stabilizes upstream or downstream, the temperature across the gas-phase reaction front and the local catalytic activity undergo variations. This

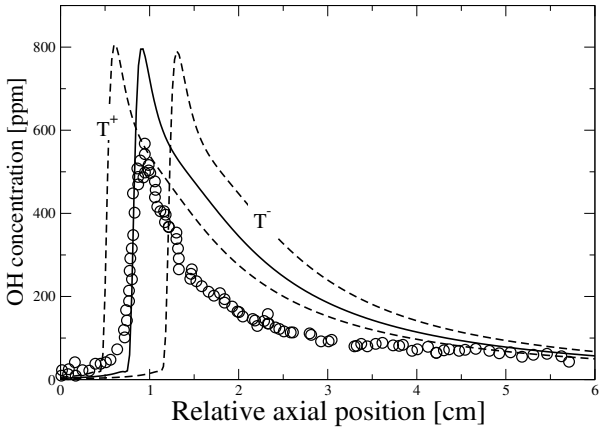

(A) Inlet temperature

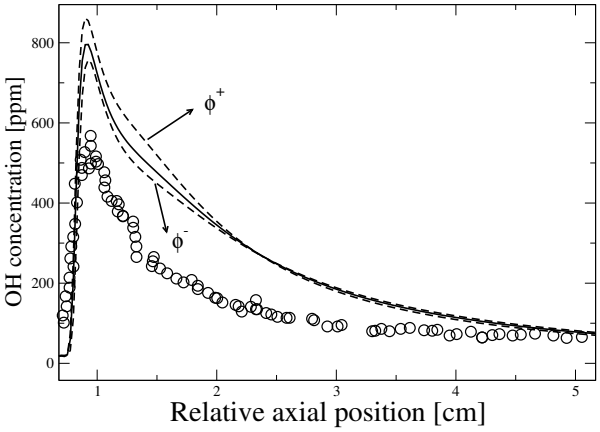

(B) equivalence ratio

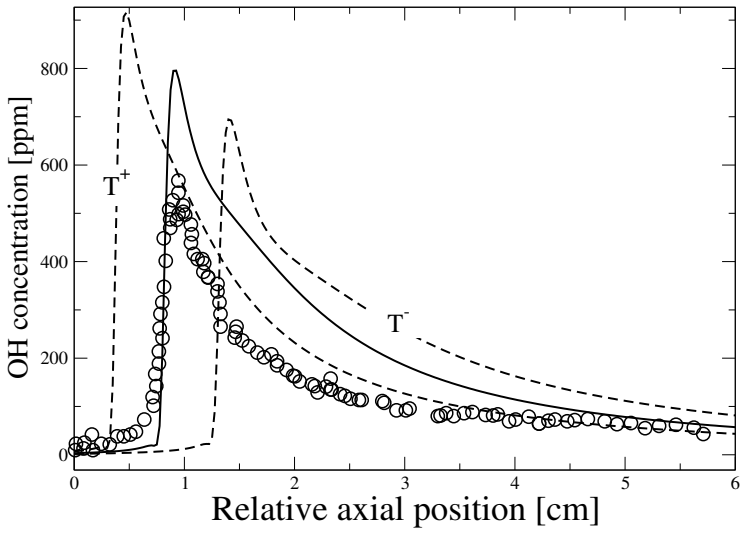

(C) Wall temperature

FIGURE 5.10: Effect of the inlet conditions and wall temperature on the OH concentration profile at the channel-centerline. Symbols: experiment. Lines: Computations.

results in the modification of the OH concentration peak because the latter is sensitive to both, local gas-phase temperature and OH adsorption/desorption levels of the reactive wall.

A $\pm 10\%$ variation of the wall temperature and inlet conditions results in profiles that are not likely to match with the experimental profiles because the flame is shifted and OH peaks are modified while the reaction front thickness remains the same. It can be concluded that the observed discrepancy in terms of

OH profiles between experiments and our simulations cannot be related to effects of uncertainties in inlet or wall conditions.

5.4.2 Influence of the grid resolution

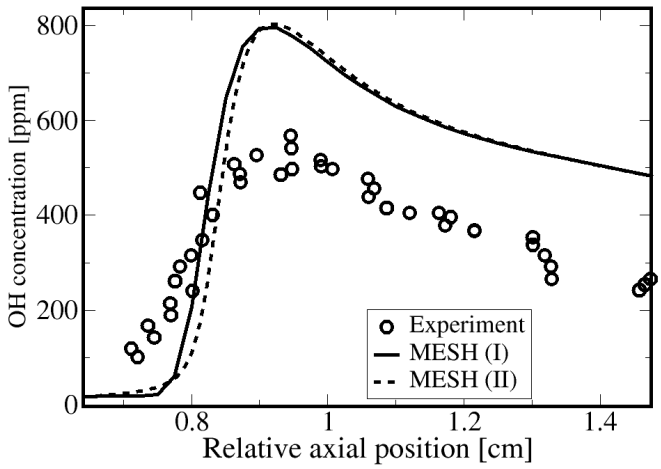

FIGURE 5.11: Effect of the grid on the axial OH profiles in the channel center-line

The steady-state numerical simulations were performed using Mesh (II) which is described in Table 5.6. In order to evaluate the impact of the mesh resolution on the observed discrepancies between experiments and simulation, the much finer MESH (II) was used to compute the steady-state solutions, as shown by Figure 5.11.

5.4.3 Assessment of the modeling assumptions

The influence of the numerical scheme and the kinetic solver used for the resolution of gas-phase reactions are evaluated at first. Second, the *Hirschfelder & Curtiss* approximation used to model diffusion velocities is assessed using the complex transport EGlib library [77].

5.4.3.1 Verification of the numerical scheme and the gas-phase kinetic solver

First, the 3-step time integration GRK numerical scheme is tested in place of the Lax-Wendroff scheme for the time integration in AVBP, and the results are shown in Figure 5.12a. Second, gas-phase chemistry

is resolved using the implicit VODE solver instead of the explicit 1^{st} order Euler method and the results are shown in Figure 5.12.

The GRK numerical scheme (Fig 5.12a) results in a lower OH level and profile thickness but the differences can be considered negligible. Using the implicit solver for the gas-phase reactions does not result in any modification of the channel center-line profiles.

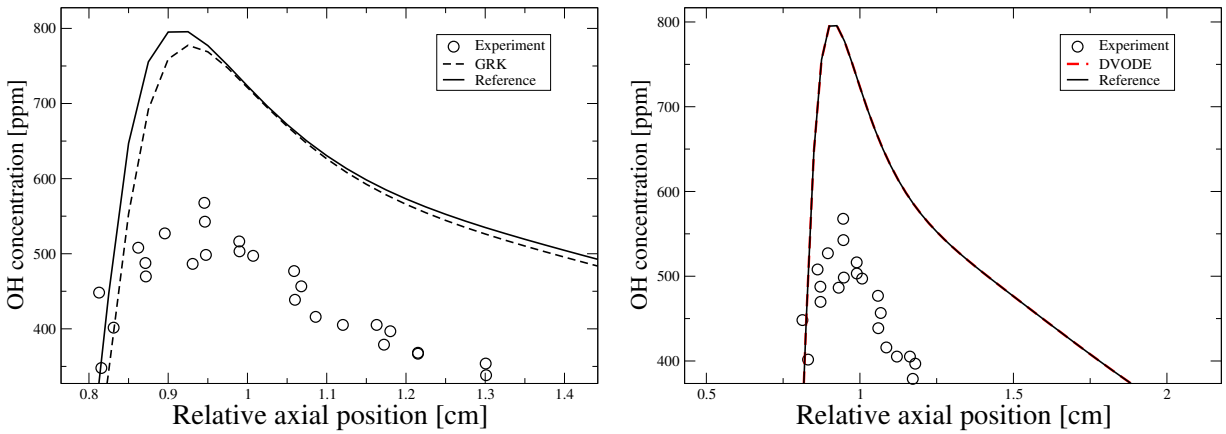

(A) Numerical scheme (B) Kinetic solver

FIGURE 5.12: (a) the time integration scheme of the CFD code AVBP and (b) the ODE solver used for the gas-phase chemistry.

5.4.3.2 Assessment of the *Hirschfelder & Curtiss* approximation

The configuration of the flow is laminar, molecular transport plays thereby a key role in transfers which might influence the OH concentration levels. Therefore, in order to assess the present modeling of diffusion described in Chapter 2, the following comparison is made: The heat and mass fluxes resulting from the constant transport coefficients and the *Hirschfelder & Curtiss* assumptions made in the present modeling, are compared to their corresponding exact expressions *a priori* estimated, i.e. by post-processing the steady-state results of the numerical simulations thanks to a complex transport library (EGlib library [77]).

Tables 5.10 and 5.11 summarize the multi-species complex transport expressions for the diffusive mass and heat fluxes. The differences between the assumptions made in the present modeling and the exact expressions (*a priori* estimation) are highlighted. $D_{k,j}^{EGlib}$ represents the binary diffusion matrix, χ_j^{EGlib} correspond to the thermal diffusion ratios and λ^{EGlib} refers to the *a priori* assessed thermal conductivity coefficient. Figure 5.13 describes the *a priori* estimation approach which consists of the following steps :

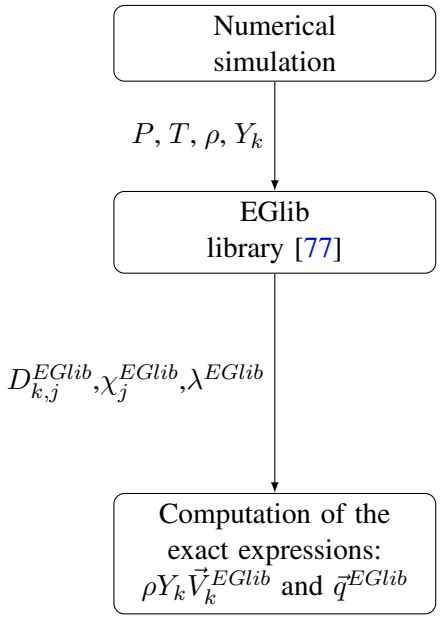

FIGURE 5.13: Summary of the *a priori* estimation of the heat and mass fluxes exact expressions

Model	Mole fraction and pressure gradients	*Soret*
Present modeling $\vec{V}_k$	*Hirschfelder & Curtiss* approximation	Neglected
a priori estimation $\vec{V}_k^{EGlib}$	$\sum_{j\in\Omega_G} D_{k,j}^{EGlib}\left(\vec{\nabla}X_j + (X_j - Y_j)\frac{\vec{\nabla}p}{p}\right)$	$+ \sum_{j\in\Omega_G} D_{k,j}^{EGlib}\left(\chi_j^{EGlib}\frac{\vec{\nabla}T}{T}\right)$

TABLE 5.10: Diffusion velocities used to calculate the mass fluxes $\rho Y_k \vec{V}_k$: Present modeling versus *a priori* estimation

Model	*Fourier*	Sensible enthalpy diffusion	*Dufour*
Present modeling $\vec{q}$	$-\lambda\vec{\nabla}T$	$+ \rho \sum_{k\in\Omega_G} h_{s,k} Y_k \vec{V}_k$	Neglected
a priori estimation $\vec{q}^{EGlib}$	$-\lambda^{EGlib}\vec{\nabla}T$	$+ \rho \sum_{k\in\Omega_G} h_{s,k} Y_k \vec{V}_k^{EGlib}$	$+ p \sum_{k\in\Omega_G} \chi_k^{EGlib}\vec{V}_k^{EGlib}$

TABLE 5.11: Diffusion heat fluxes: Present modeling versus *a priori* estimation

- First the EGlib library is fed with the reactive flow field resulting from the numerical simulations;
- Exact transport coefficient are then computed as explained by Ern and Giovangigli in [77];
- Fluxes are finally reconstructed using the exact expressions of Tables 5.10 and 5.11.

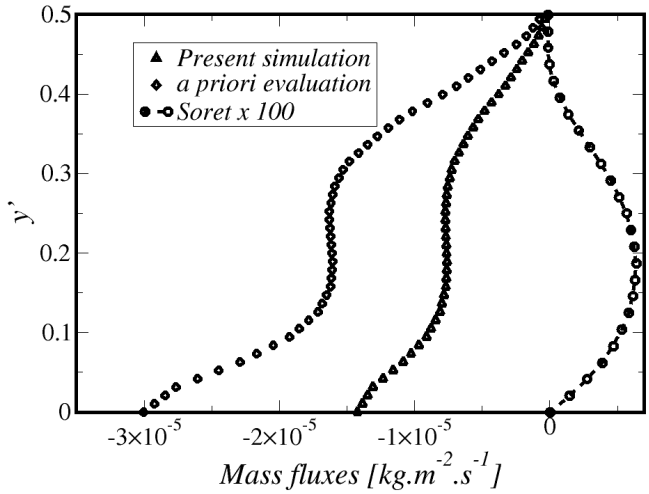

FIGURE 5.14: Comparison of *a priori* estimation versus the present simulation : *Soret* term versus diffusion induced by mole fraction and pressure gradients at the steady-state. y' is the normalized channel height y/H.

Surface chemistry mainly interacts with the gas-phase transport orthogonally to the reactive wall. Therefore only transverse profiles of fluxes are analyzed in Figures 5.14 and 5.15 at the axial position where OH reaches its maximum. Stiffest gradients are found at this position thus coinciding with maximum wall transfers. Figure 5.14 shows the comparisons of the transverse profiles of the diffusion mass flux (*Soret* effect not included) and *Soret* diffusion term for OH species. The following observations can be made :

- The *Soret* effect is negligible compared to the diffusion due to species gradients as it is 100 times lower with zero values at the wall.
- The present modeling predicts lower OH mass fluxes due to species gradients in both the gas phase and at the wall than the one estimated using the exact expressions. The *Hirschfelder & Curtiss* assumption can be designated as the source of error. It is stressed that the present modeling is performed with Schmidt numbers taken equal to 0.7 for all species.

Heat fluxes are plotted in Figure 5.15. The following features are noted:

- Dufour effect is totally negligible at the considered atmospheric pressure compared to sensible enthalpy diffusion and *Fourier* transport as it is 1000 times lower.

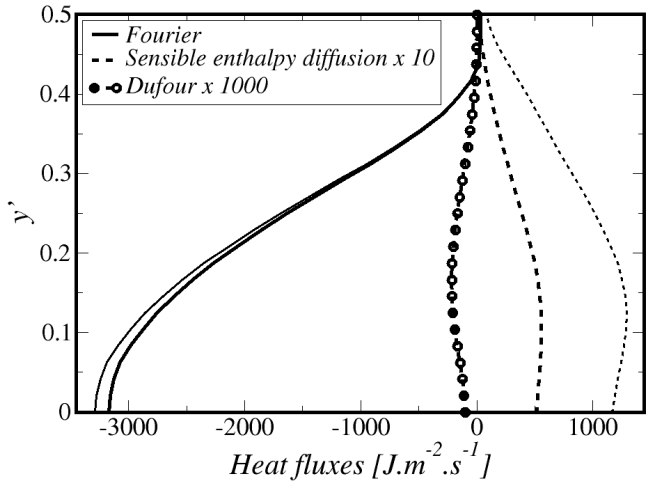

FIGURE 5.15: Comparison of *a priori* evaluation (thin lines) versus the present simulation (thick lines). y' is the normalized channel height y/H.

- Sensible enthalpy presents lower levels by one order of magnitude, along the channel height, compared to the *Fourier* term. Therefore, transverse heat diffusion is mainly due to temperature gradients. The discrepancies observed for mass diffusion impact the heat fluxes of sensible enthalpy thus resulting in a gap between the present modeling and the *a priori* estimated one.

- The present modeling for the *Fourier* transport present lower values at the wall compared to the one given by the complex library, thus suggesting that the *Hirschfelder & Curtiss* assumption is not fully satisfied near the reactive surface. The present modeling is performed with a constant Prandtl number taken equal to 0.7 which results in a unity Lewis number.

To conclude, the approximation made when describing the diffusive transport phenomena may contribute to the discrepancy observed between the predicted and measured OH concentration. The *a priori* estimation shows that accounting for complex transport leads to higher OH mass fluxes and temperature gradients to the wall. This is likely to lead to higher OH adsorption levels by the catalytic walls which would decrease the overall OH levels. This might explain the over-prediction of OH concentrations resulting from the present numerical simulations.

Also, given the fact that pressure is constant and that the *Soret* and *Dufour* terms are negligible, the differences between the present modeling and the exact expressions are mainly attributed to the error made in predicting diffusion due to species gradients.

5.4.4 Uncertainties related to chemical kinetics

Although the gas-phase kinetic schemes used in this study were validated over a wide range of conditions [22, 42, 48], validations did not directly concern conditions identical to the present ones. Especially, the reduction of the gas-phase kinetic scheme decreases its range of validity.

It is also highly probable that a reduced gas-phase kinetic scheme over-predicts radical concentrations, as some radicals are eliminated in the reduction process and therefore element conservation forcefully implies over-prediction of the rest of the radicals. As a result, a 1D flame comparison of the OH concentration predicted with the detailed and the reduced chemistry is performed using the PREMIX solver of the CHEMKIN library. The resulting OH mole fractions are plotted versus the distance from the inlet in Figure 5.16. A C1/C2 version was used for the detailed chemistry for CPU time convenience.

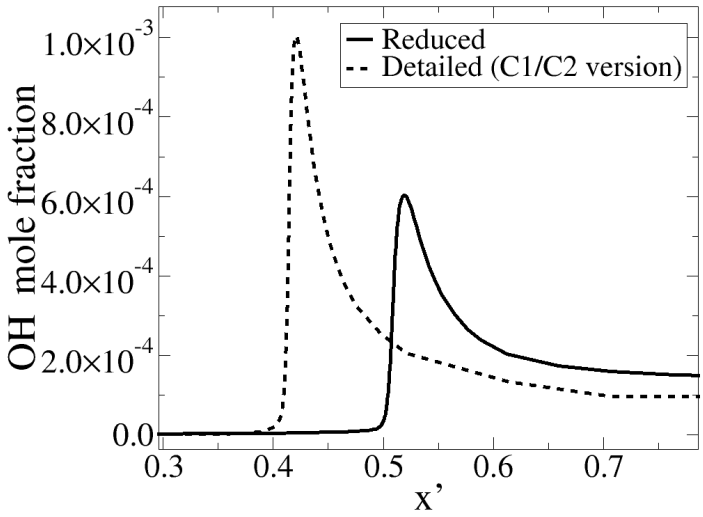

FIGURE 5.16: 1D flame computations: comparison of the OH mole fraction predicted with the detailed and the reduced chemistry

It is observed that the detailed kinetic scheme results in a higher OH mole fraction compared to the one obtained with the reduced kinetic scheme. This indicates that the over-prediction of the OH levels observed in the 2D computations are not likely to be related to the reduction of the gas-phase kinetic scheme as the use of a detailed mechanism would have probably led to higher concentrations. Nonetheless, the impact of the uncertainties related to the kinetics requires to be quantified through a sensitivity analysis in further computations.

5.4.5 Uncertainties related to radiative heat transfers

Considering the high surface to volume ratio encountered within the presented channel and the high wall temperature that ranges from 1285 K to 1365 K, neglecting the radiative heat transfers in the energy equation could have an impact on the predicted temperature and OH levels. In order to assess the impact of this assumption the radiative heat transfer is *a priori* estimated and compared to the sensible heat flux and the heat release due to gas-phase chemical reactions using the expression given in Table 5.12. The heat fluxes are averaged in the transverse direction and plotted versus the distance from the channel inlet in Figure 5.17.

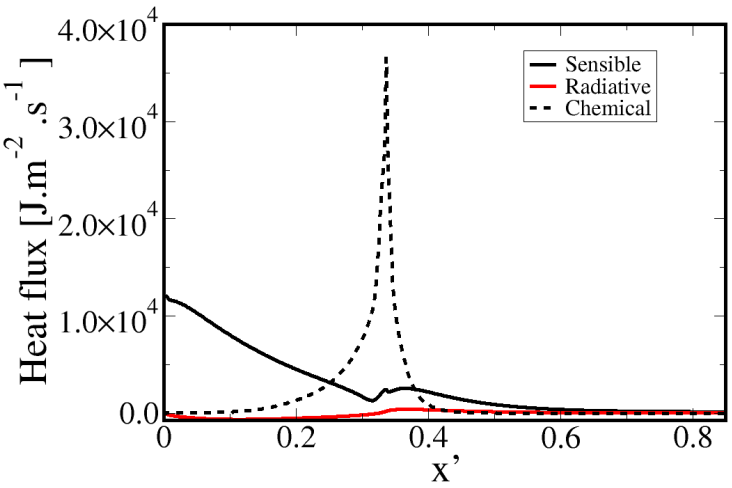

FIGURE 5.17: Comparison of the *a priori* radiative heat flux with the chemical and sensible terms.

Sensible	Chemical	Radiative
$-\lambda\vec{\nabla}T + \rho \sum_{k\in\Omega_G} h_{s,k}Y_k\vec{V}_k$	$\rho \sum_{k\in\Omega_G} \Delta h^o_{f,k}Y_k\vec{V}_k$	Barlow *et al.* [100]

TABLE 5.12: Expressions of the heat fluxes

Figure 5.17 shows that the radiative transfer is negligible compared to the chemical and sensible heat fluxes along the whole channel length. This *a priori* shows that accounting for the radiative transfers is not likely to impact the predicted temperature. As the OH concentration is sensitive to temperature, OH concentration should not be impacted as well. Consequently, the discrepancies between the predicted and the measured OH concentration levels in the flame region are not due to the fact that the radiative term was neglected. Nevertheless, the radiative term should be *a posteriori* accounted for in further computations in order to assess the present observation.

5.4.6 Conclusions of the investigation

Several possible sources of error were investigated in order to explore possible reasons for the differences observed in the OH concentration profiles at the center-line of the channel, which can be summarized as follows:

- Possible uncertainties of wall temperature and inlet conditions do not explain the observed differences between the modeling and the experiment. It must be emphasized that actual measurement uncertainties were not quantified in the study of Dogwiler *et al.*.
- Refining the grid resolution has no impact on the steady-state also confirming *a posteriori* that the reaction front is already well resolved on the coarsest mesh.
- The time integration scheme of the CFD code and the gas-phase kinetic solver were not found to noticeably impact the OH center-line profiles.
- Accounting for complex transport might result in lower levels of OH because the mass and heat transfers of OH species to the reactive wall are under-estimated by the present modeling. However, *Soret* and *Dufour* terms would have to be implemented and the simulations should be run with the resulting exact approach. Moreover, adapted boundary conditions of reactive walls need to be derived in this context.

5.5 Activation of gas-phase reactions

The first phase we propose to discuss is the one exhibiting the initialization of gas phase reactions due to auto-ignition chemistry. The normalized temperature field θ_T is plotted at $t = 0$ in Figure 5.18. $\theta_T = (T - T_{min}) \,/\, (T_{max} - T_{min})$ where T_{min} and T_{max} respectively refer to the maximum and minimum temperature at $t = 0$. The observed profiles correspond to a thermal boundary layer with a maximum temperature established downstream the channel. This is due to the isothermal wall that initially presents a higher temperature.

Normalized transverse profiles of OH mass fraction and heat release rate are plotted in Figure 5.19 where the transverse temperature is established ($x = 0.9\ L_c$) and for different instants ranging from 0.05 t_{AI} to 0.25 t_{AI}. τ refers to the normalized time and equals t/t_{AI}. Figure 5.19a shows that the OH transverse profiles present mass fractions that are higher at the wall. This results from the surface OH desorption by the Pt active sites. It is noticed in Figure 5.19b that the transverse profiles of the gas-phase heat release

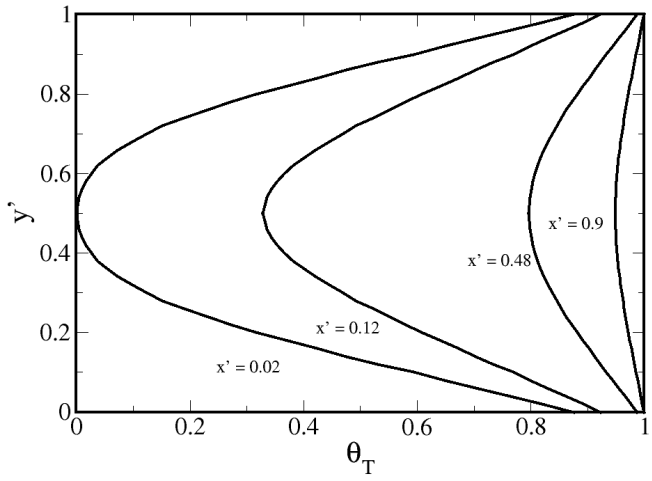

FIGURE 5.18: Temperature profiles along the channel length at $t = 0$

rate present similar positive gradients at the wall. Radical species desorption thereby leads to the activation of gas-phase reactions. Gaseous chemistry is therefore initially activated in the downstream vicinity of the catalytic plate as surface reactions are activated.

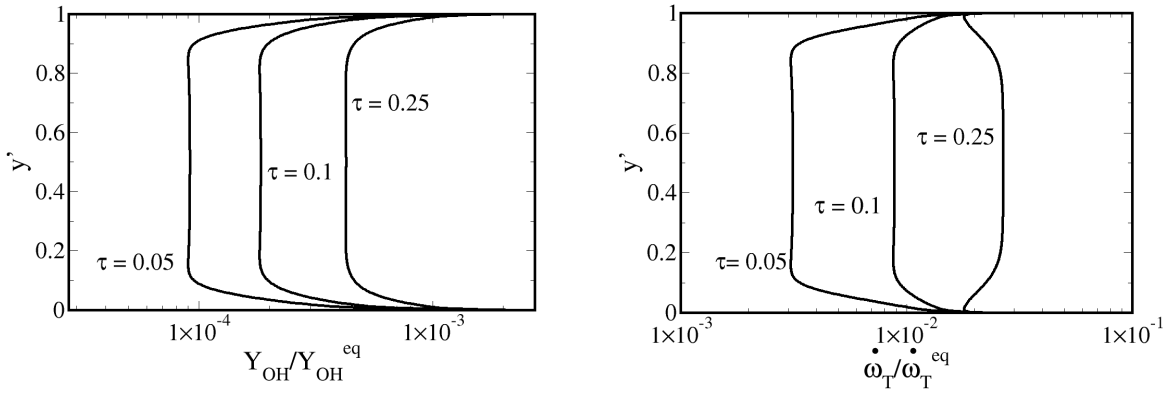

(A) Transverse profiles of the normalized OH mass fraction (Log scale)

(B) Transverse profiles of the normalized gas-phase heat release rate (Log scale)

FIGURE 5.19: Transverse profiles of the normalized OH mass fraction and gas-phase heat release rate at $0.05\ t_{AI} \leq t \leq 0.25\ t_{AI}$.

Normalized transverse profiles of OH mass fraction and heat release are plotted in Figure 5.19 for $x = 0.9$ L_c and for different instants ranging, from 0.05 t_{AI} to 0.25 t_{AI}. The overall trend corresponds to the increase with time of both OH mass fraction and gas-phase heat release in the gas-phase and at the wall, as chemical reactions take place in the whole transverse direction. Nevertheless, Figure 5.19a shows that

the OH transverse profiles present mass fractions that are higher at the wall. This results from the surface OH desorption by the Pt active sites. It is noticed in Figure 5.19b that the transverse profiles of the gas-phase heat release present similar positive gradients at the wall. Radical species desorption thereby leads to the activation of gas-phase reactions. Gaseous chemistry is therefore initially activated only in the vicinity of the reactive wall.

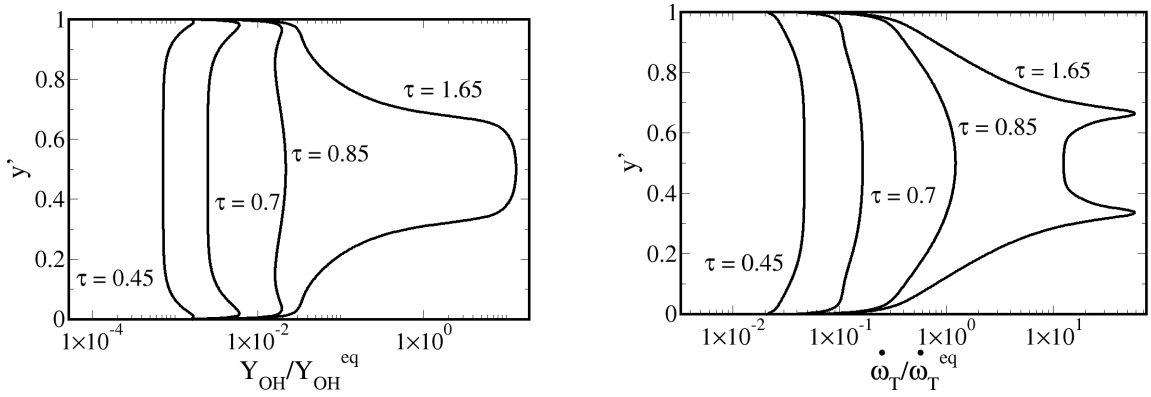

(A) Transverse profiles of the normalized OH mass fraction (Log scale)

(B) Transverse profiles of the normalized gas-phase heat release(Log scale)

FIGURE 5.20: Transverse profiles of the normalized OH mass fractions and gas-phase heat release rate at $0.45\ t_{AI} \leq t \leq 1.65\ t_{AI}$

Figure 5.20 shows the normalized transverse profiles of OH mass fraction and heat release at $x = 0.9$ L_c and for different instants ranging from 0.45 t_{AI} to 1.65 t_{AI}. Negative wall gradients of both OH mass fraction and gas-phase heat release are observed. This is because the near-wall OH and gas-phase heat release resulting from the activation of surface reactions progressively diffuse in the upper transverse direction. At 1.65 t_{AI}, both transverse profiles present a difference of 2 orders of magnitude between the wall and the channel center.

In order to explain this gap, the characteristic times of gas-phase species diffusion and chemistry are compared by *a priori* estimating the Damköhler number $Da|_{AI} = t_{diff}^{spec}/t_{AI}$ under the conditions taken downstream the channel at $t = 0$. It is defined as the ratio between the ignition time t_{AI} and the characteristic time of species diffusion in the transverse direction ($t_{diff}^{spec} = h_c^2/(\nu Sc)$. $t_{AI} = 4.5$ ms is determined using homogeneous reactor computations and refers to the time for which OH reaches 50% of its maximum value. The resulting $Da|_{AI}$ equals to $\simeq 13$. This means that the characteristic time of species diffusion in the transverse direction is much larger than the ignition time of gas-phase reactions.

This could explain why gas-phase chemistry ignites at the channel center regardless of the influence of

the catalytic activity at the surface. Simulation of combustion with deactivated surface reactions, performed under similar conditions, shows that gas-phase reactions are also activated downstream, although the ignition time is slightly higher. This implies that the activation of combustion in the catalytic channel is governed by the auto-ignition of gas-phase chemistry with a limited role of surface reactions in the ignition process under the present conditions.

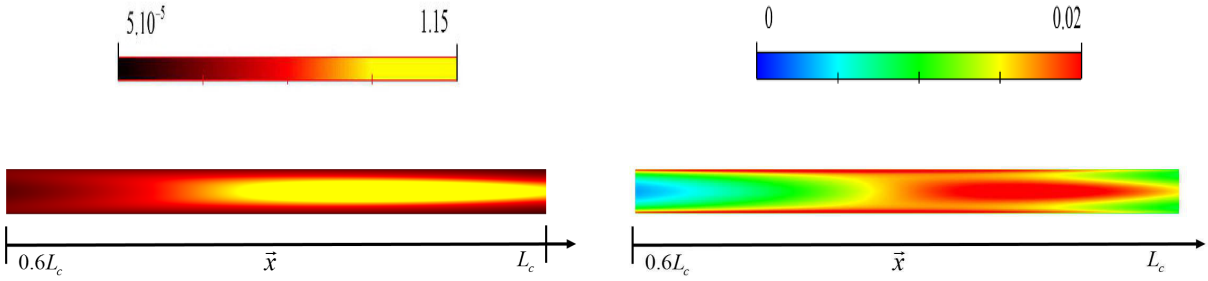

(A) $\frac{\dot{\omega}_T}{\dot{\omega}_T^{eq}}$ (B) $\frac{Y_{OH}}{Y_{OH}^{eq}}$

FIGURE 5.21: 2D Normalized gas-phae heat release rate (left) and OH concentration maps (right) at $t = 1.5\ t_{AI}$

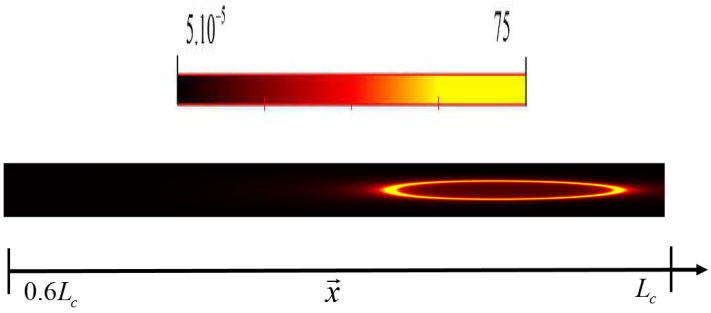

FIGURE 5.22: 2D field of the normalized gas-phase heat release rate at $t = 1.65\ t_{AI}$

2D fields of the normalized gas-phase heat release rate and OH mass fraction are provided in Figure 5.21 at t_{AI}. It shows that the highest rates of heat release and OH mass fractions form a kernel downstream. A few instants later (at 1.65 t_{AI}), the gas-phase heat release presents the shape of a ring as shown in Figure 5.22 which is represented by the two dominating peaks in the gas-phase heat release transverse profiles, plotted in Figure 5.20b. This renders the fact that a flame is forming which results from the auto-ignition of the gas-phase.

5.6 Grid resolution quality and CPU cost

As mentioned in Section 5.4, two mesh were used. Mesh (I) was first used in order to capture the reaction front during the ignition and propagation process. Mesh (II) was used for the stabilization phase characterized by a wider reaction front. In order to define the time range corresponding to each phase, the position of the flame in the channel is tracked. to this purpose, we define X_f as the axial center-line distance between the inlet of the catalytic channel and the axial point where the OH concentration reaches its maximum normalized by the anchoring position. This yields $X_f = 1$ as the flame stabilizes. The temporal evolution of X_f is plotted in Figure 5.23. At approximately $t = 3\ t_{AI}$ the slope of X_f decreases as the flame slows down to stabilize at $t = 12 \times t_{AI}$. Therefore the ignition and propagation phase is the process occurring for $t \leq 3\ t_{AI}$. the stabilization process refers to $t \geq 3\ t_{AI}$.

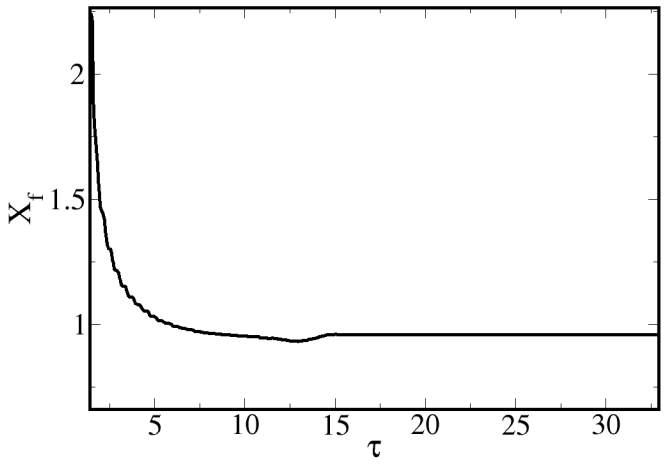

FIGURE 5.23: Temporal evolution of the reaction front position X_f

Figure 5.24 gives the mass fraction profiles of some minor species (CH_3O, CH_2O and O) in the axial direction at the channel center-line. Regarding transverse resolution, Figure 5.25 shows mass fractions of OH and O species plotted in the transverse direction of the reaction front. It is clearly observed that the profiles are resolved on on at least 10 nodes in both directions.

It may seem that Mesh (II) needs refinement in the transverse direction particularly as shown by Figure 5.25c. but it was shown in Section 5.3 that using a finer mesh had no impact on the steady-state features of the flame (Fig 5.11). Figure 5.26 shows the evolution of the different time steps. Computations are limited by the CFL time step. It is in particular, 10 times lower for the ignition process (Fig 5.26a) than for the stabilization phase (5.26b) because of the mesh size. As a consequence, the first phase is much more expensive as highlighted in Table 5.13.

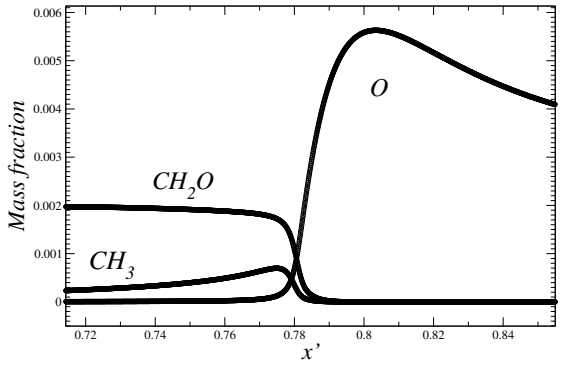

(A) AI

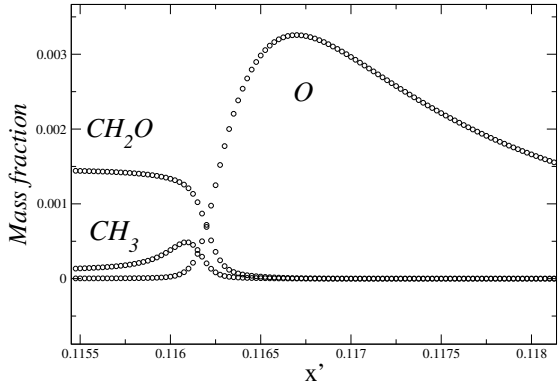

(B) Propagation

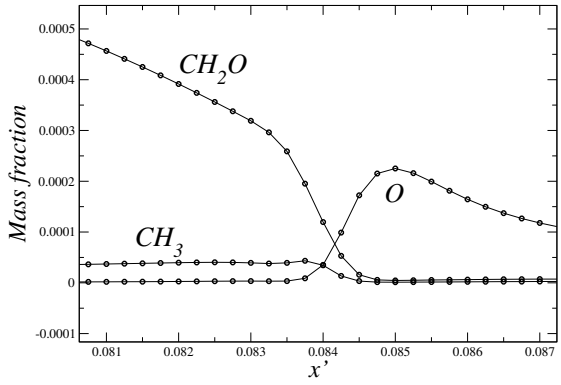

(C) Stabilization

FIGURE 5.24: Axial profiles of certain stiff species along the reaction front

Performing a full transient simulation, using MESH (I), would therefore result in a cost that is estimated to $72h \times (12t_{AI}/3t_{AI}) = 288h$. In other words, such a computation would cost 12 days over 256 processors which is tremendous. This thereby justifies the meshing strategy of the present study. Table 5.13 also

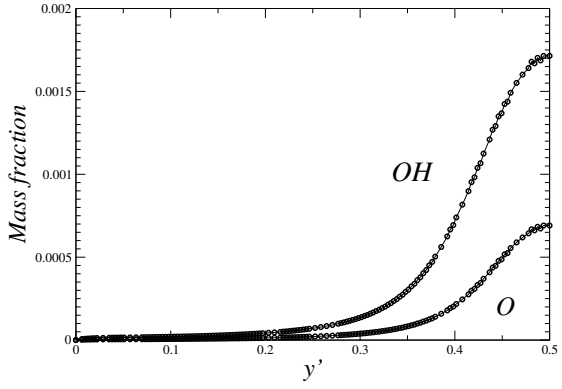

(A) AI

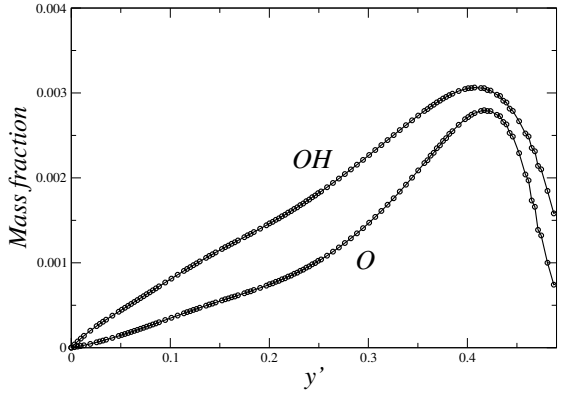

(B) Propagation

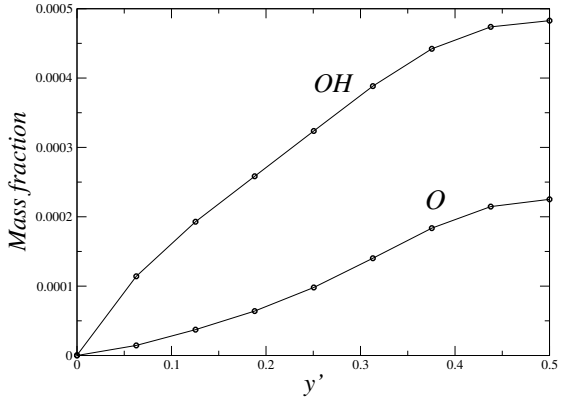

(C) Stabilization

FIGURE 5.25: Transverse profiles of radical species along the channel height

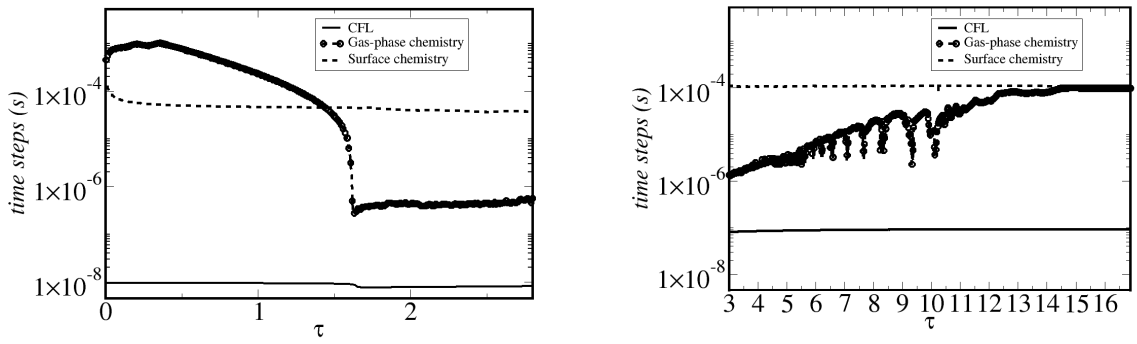

(A) AI and propagation

(B) Stabilization phase

FIGURE 5.26: Comparison of the time step : CFL time step versus time steps based on gas-phase and surface reactions.

indicated that surface chemistry is twice more expensive in the first phase. Indeed, surface kinetics are very stiff during ignition. As a result, the implicit solver induces an additional cost but this is not particularly related to the grid resolution.

Phase	time range	limiting time step	nodes	Procs	CPU time	G cost	S cost
AI + Propagati	$t \leq 3\, t_{AI}$	$CFL \approx 1 \times 10^{-8}$	1.2×10^6	256	72 h	40%	20%
Stabilization	$3\, t_{AI} \leq t \leq 12\, t_{AI}$	$CFL \approx 1 \times 10^{-7}$	30.000	16	11 h	40%	10%

TABLE 5.13: CPU cost of the calculation under the conditions of case (a). G cost and S cost respectively stand for the CPU time consumed by gas-phase and surface chemistry. A similar cost is observed for case (b) and (c).

5.7 Comparison with an inert-wall channel

The stabilizing effect of the catalytic walls on gas-phase combustion is emphasized by numerically deactivating surface reactions. These tests are solely performed under the conditions of case (a). The steady-state results of both inert-wall and catalytic wall simulations are compared. In order to capture possible asymmetric features of the flame, the simulations are carried out in a complete geometry.

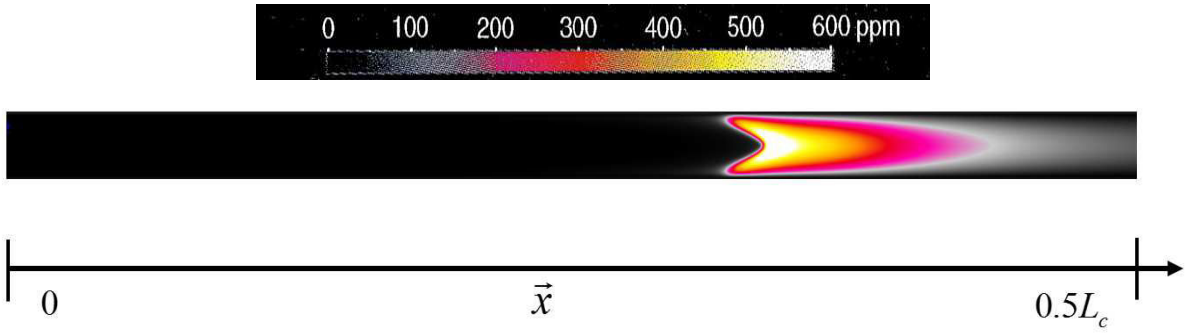

FIGURE 5.27: OH concentration map for the catalytic channel at steady-state ($t = 25\ t_{AI}$)

Figure 5.27 shows steady-state OH concentration maps of the catalytic wall simulation. As observed in the experiment and modeled under the symmetry assumption in the present study, flame features which consist of the symmetric V-shape, sweep angles and OH concentration levels, are well conserved. This confirms yet again the symmetry assumption.

The temporal evolution of the reaction front position (X_f) taken at the flame leading edges, for both inert and reactive wall channels, are plotted in Figure 5.28. The inert wall case presents an oscillating evolution with a constant amplitudes, whereas the temporal evolution of the catalytic case reaches a steady-state. It is also observed that the reaction front anchors much further upstream when surface reactions are deactivated, i.e, at $x = 0.125L_c$ while the flame stabilizes at the expected location in the catalytic channel, i.e, at $x = 0.34L_c$. The order of magnitude of the difference between the two stabilization locations is 8.5 times the channel total height.

In order to show the transient behavior of the inert-wall case, OH concentration maps of the inert-wall simulation are shown in Figure 5.29 at 23 t_{AI} and 26 t_{AI}. A slant-shape flame is observed in the vicinity of channel inlet with a leading edge oscillating between the lower half (Fig 5.29a) and the upper half of the channel (Fig 5.29b). Also, OH levels are much higher compared to the catalytic case because OH species is no longer adsorbed by the wall since surface reactions are deactivated.

Deactivating surface reactions therefore results in an oscillatory asymmetric slant-shape flame that anchors in the vicinity of the inlet, under the present conditions. Although this might lead to shorter conversion

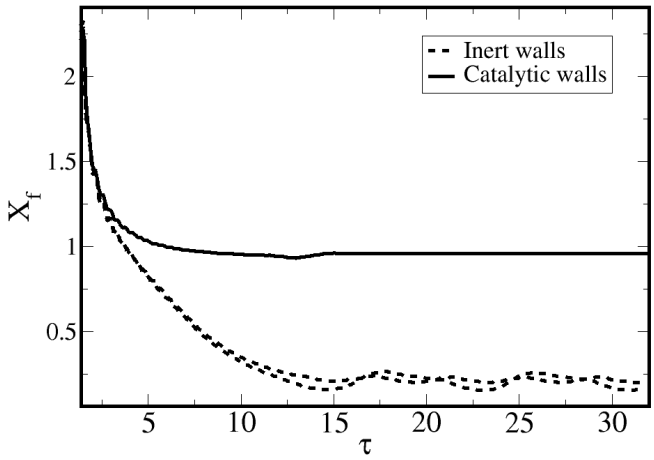

FIGURE 5.28: Temporal evolution of the normalized reaction front position X_f taken at $y = 0.5\ h_c$ and $1.5\ h_c$: Channel with inert walls versus catalytic channel.

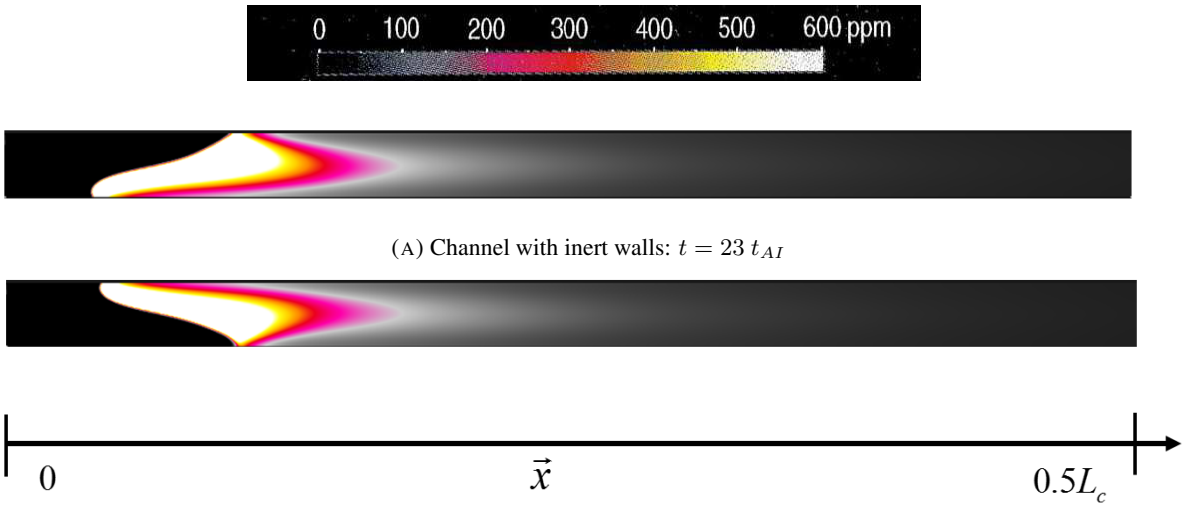

(A) Channel with inert walls: $t = 23\ t_{AI}$

(B) Channel with inert walls: $t = 26\ t_{AI}$

FIGURE 5.29: OH concentration maps for the channel with inert walls

distances which is practical for possible system downscaling, instabilities and asymmetries are undesirable as it might ruin the operating system and yield performance inhomogeneities.

Such behaviors are representative of possible hydrodynamic [101] or thermal-diffusive instabilities [102–104] encountered in laminar meso-scale channels with isothermal or non-adiabatic walls. The shape and transient behavior observed in the inert case are in line with the experiment of Dogwiler *et al.* [27] although performed under different conditions. Here, the same conditions are adopted for both cases to provide a proper comparison and illustrate numerically that surface reactions restore the symmetric features of flames undergoing asymmetric instabilities as reported in numerical studies of Pizza *et al.* [105]. The investigation of the underlying phenomena of the observed instabilities and the stabilizing effect of surface reactions is out of the scope of this study. Nonetheless, the numerical modeling of the present study shows its capability of reproducing such features.

5.8 Conclusions

In this Chapter, 2D simulation of gas-phase combustion of a lean premixed CH_4/air mixture in a catalytic meso-scale channel with planar walls were presented. First, the results were validated at steady-state by comparing the numerical results with experimental data of Dogwiler *et al.* [27]. The study of the influence of non-chemical parameters and modeling assumptions enabled to identify the possible sources of discrepancies. Second, some insight was provided into the ignition and flame propagation processes within catalytic channels. Finally, deactivating surface reactions enabled to emphasize the stabilizing effect of the catalytic walls on gas-phase combustion. The conclusions are listed as follows :

- The comparisons of the steady-state results (Section 5.3) with the experiments [27] have shown that the present numerical modeling was capable of reproducing the main features of the flames under different inlet conditions: The V-shaped flames and the sweep angles were reproduced with an acceptable manner. Comparable predictions of the flame anchoring position and levels of OH concentration were obtained as well. However, the numerical modeling overpredicted the flame thickness and the OH concentration peak at the channel center-line by approximately 50 and 20 % respectively.
- The investigation of the discrepancies (Section 5.4) enabled to point to the following potential sources of error :
    - The *a priori* estimation has shown that the wall heat and mass transfers of OH were underpredicted by the present modeling. therefore, accounting for a more complex modeling of

diffusion is likely to reduce the OH levels but the *Soret* and *Dufour* terms would have to be implemented and the simulations should be run with the resulting exact approach. Moreover, adapted boundary conditions of reactive walls need to be derived in this context. This was not feasible in the time framework of the present study given the CPU time described in Subsection 5.6.

- The uncertainties related to the kinetic mechanisms are likely to yield non-negligible differences between the modeling and the experiments. Sensitivity analysis to both gas-phase and surface kinetics should thereby be performed in order to estimate the resulting impact on the numerical predictions. It is stressed that this was not possible in the time framework of the present study.
- The transient analysis (Section 5.5) allowed to show that the flame results from gas-phase auto-ignition downstream the channel. The influence of surface reactions was found of minor importance on the gas-phase ignition phase.
- Deactivating surface reactions (Section 5.7) resulted in an oscillatory asymmetric slant-shape flame that anchors much further upstream compared to the catalytic channel which was also observed in the experiments of Dogwiler *et al.* [27]. The numerical modeling of the present study has thereby shown its *a priori* ability of reproducing the possible instabilities encountered in meso-scale channels with inert walls and the stabilizing effects of surface reactions.

Despite the observed differences, the present modeling has shown its capability of capturing the main features of the flame within catalytic meso-scale channels with planar walls. These observations enabled to validate the modeling and resolution of both gas-phase and surface kinetics on the hand, and the use of boundary conditions to represent the interplay between the gas-phase transport and the reactive wall on the other hand.

Chapter 6

Impact of non-planar walls on combustion in a meso-scale channel

Introduction

The numerical strategy described in Chapter 2 and 3 and validated in Chapter 5, is now used to study the potential impact of obstacles and segmented coating on the anchoring positions of the flame and fuel conversion within catalytic meso-scale channels.

To this purpose, the catalytic channel with planar walls presented in Chapter 5, is modified by the introduction of cavities and obstacles on the catalytic walls under the conditions of case (a). Transient numerical investigations are thereby performed in order to provide some insight on the underlying process leading to the steady-state flame stabilization and fuel conversion performance. Figure 6.1 shows the part of the channel highlighted by the red box, where the obstacles or cavities are introduced.

The structure of the present Chapter is as follows:

- A state of the art is discussed at first in Section 6.1 in order to position the targeted objectives of the present study.
- The numerical setup and modeling assumptions are described in Section 6.2.
- The influence of obstacles, cavities and type of Pt-coating on the anchoring position of the flame and CH_4 conversion rate are presented at steady-state in Section 6.3.

- In order to explain the results, the transient dynamics of the flame propagation are analyzed under the considered configuration in Section 6.4.
- Conclusions and perspectives are finally discussed in Section 6.5.

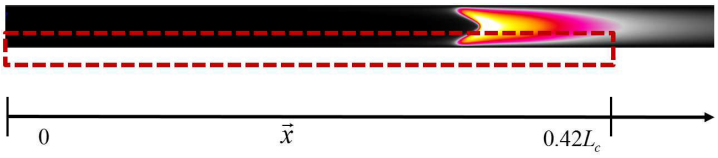

FIGURE 6.1: Part of the channel modified by introducing obstacles and cavities.

6.1 State of the art

Numerical investigations of the introduction of obstacles or cavities in catalytic meso-scale channels have mostly been reported for application representative of gas-turbines applications using CST (Catalytically Stabilized Thermal combustion). Nonetheless, the corresponding findings have proved to exhibit interesting properties for the considered applications of the present thesis. Li et al. [106, 107] have numerically shown that cavities could enhance the heat and mass transfers inside the cavities, thus resulting in a better conversion of reactants and efficiency in catalytic applications. Also, the low velocity zone within the concave regions have proved to increase the blow-off and blow-out limits of the flames so that higher energy density operating range could be achieved. The introduction of wall cavities were combined to segmented catalytic coating to avoid gas-phase and surface reactions competition. This behavior was observed in former studies of Di Benedetto *et al.* [108, 109] for planar channels using steady-state modeling. Ran *et al.* [110] have shown numerically that the introduction of one obstacle or a cavity could possibly allow a system downscaling and catalyst loading reduction, as a consequence of a reaction front that anchors closer to the inlet which result in shorter conversion distances.

However, it should be stressed that the above mentioned numerical studies of Li *et al.* [106, 107] on catalytic walls with obstacles focus on state-state 2D modeling of gas-phase transport. The underlying dynamic yielding the flame to stabilize closer to the inlet is explained through a steady-state analysis which does not provide, to our sense, a full comprehension of the flame anchoring process. Moreover, the effect of the presence of multiple obstacles and cavities was not compared. A comparison is made however by Ran *et al.*[110] but the study focuses on the introduction of one single cavity. Although full and alternative coating with concave cavity is reported in literature by Li *et al.* using a steady-approach, multi-segmented coating approach applied to obstacles has not been reported to our knowledge. Moreover, a lack of clarity

could also be noted regarding the derivation and validation of the boundary conditions used to account for the reactive walls.

Regarding automotive catalytic device applications [4, 15, 111], numerical approaches focusing on the introduction of local protuberances in the shape of obstacles are mostly based on steady-state approaches and assume that the gas-phase chemistry is frozen. The present study thereby aims at providing a better understanding of the underlying process leading to the steady-state flame stabilization and fuel conversion performance over different catalyst coating and obstacles/cavities configurations using transient numerical investigations which comprise a detailed description of the heterogeneous kinetics and the interplay between the gas-phase transport and the reactive wall.

6.2 Numerical modeling and assumptions

The modeling assumptions and computation strategy are similar to the ones described in Section 5.2. The major differences in terms of geometry and meshing strategy are given.

6.2.1 Setup of the simulations

Figures 6.2 and 6.3 show schematics of the two studied geometries. The obstacles and cavities are located in the upstream part of the channel only (Fig 6.1) in order to disturb the flame during the stabilization phase. d/h_c refers to the blocking ratio. The value of 25% was *a posteriori* chosen so that an interaction with the flame could be observed. In order to ensure optimal conversion rates, the gap to width ratio (referred by g/w) and the ratio w/d are inspired from the study of Li *et al.* [106, 107]. As described in Figure 6.4, the obstacles and cavities respectively restrict and increase the channel section by 25%.

Figures 6.5 and 6.6 depict the two types of Pt-coating investigated in the present study for both channels with obstacles and cavities:

- Full coating, for which Pt covers the whole wall length as shown in Figures 6.5a and 6.6a.
- Segmented coating, for which Pt only covers the top edges of obstacles (Fig 6.5b), or the edges located between the cavities (Fig 6.6b) .
- As shown in Table 6.1, segmenting the catalyst in the channel with obstacles means that 30% of the channel length of interest is coated, whereas 66.7% of the upstream half-part of the channel is coated in the case of cavities.

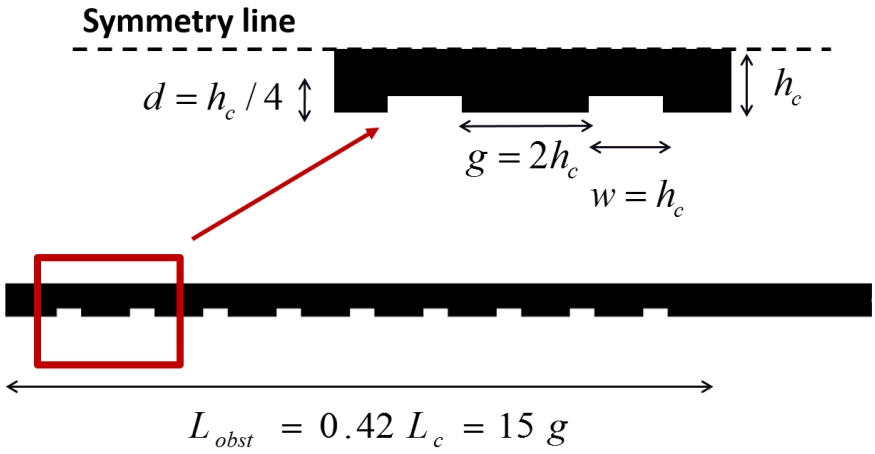

FIGURE 6.2: Schematic of the catalyst channel with obstacles

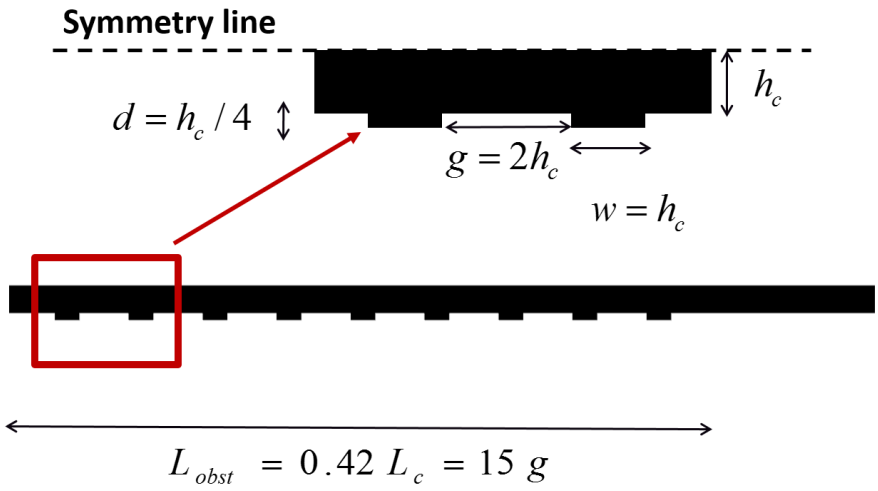

FIGURE 6.3: Schematic of the catalyst channel with cavities

FIGURE 6.4: Reduction and increase of the planar-walls channel section by the respective introduction of obstacles and cavities. Middle : planar-wall channel, left: obstacles, right: cavities

(A) Full Pt-coating (OF) (B) Segmented Pt-coating (OS)

FIGURE 6.5: Studied Pt-coatings for the channel with obstacles. The green segments highlight the edges covered with Pt.

(A) Full Pt-coating (CF) (B) Segmented Pt-coating (CS)

FIGURE 6.6: Stidued Pt-coatings for the channel with cavities: The green segments highlight the edges covered with Pt.

Case	Pt-coating ratio (%)
OS	30
OF	100
CS	66.7
CF	100

TABLE 6.1: Pt-coating ratio for the channels with obstacles and cavities: coated length divided by the channel length of interest (0.42 L_c)

Only symmetric channels are considered in the present study in order to save CPU time. Nevertheless, under the conditions of case (a), the symmetry assumption can be justified by the fact that the flame is most probably not sensitive to thermal-diffusive instabilities as reported by Pizza *et al.* [105]. Moreover, as observed in the experiments of Wan *et al.*[112], cavities are likely to maintain symmetric features of the flame.

6.2.2 Meshing strategy

The transient ignition phase is not of interest as it occurs much further downstream the channel as was explained in the previous Chapter. When the flame comes across the first obstacles or cavities, i.e. at $t \approx 4\ t_{AI}$, the gas-phase reaction front is considered wide enough to be resolved with a coarser mesh than MESH (I) described in Subsection 5.2.3. Consequently, a single coarser mesh is used to perform the whole transient simulations. Table 6.2 gives the grid size used for both types of Pt-loading while Figure 6.7 illustrates the resolution of the gas-phase reaction front in the vicinity of an obstacle.

As the mesh resolution could not be *a priori* set, it was *a posteori* checked that it allowed to resolve the gas-phase reaction front with 15 and 12 nodes in the axial and transverse directions respectively. The resulting mesh enables to discretize the obstacles height and the cavities depth with 12 nodes.

Pt-coating	$\triangle x(\mu m)$	$\triangle y(\mu m)$	$L_f/\triangle x$	$d/\triangle y$
Full	70	70	$L_f/\triangle x = 20$	$d/\triangle y = 12$
Alternative	70	70	$L_f/\triangle x = 15$	$d/\triangle y = 12$

TABLE 6.2: Grid resolutions used for the two types of Pt-coating. L_f refers to the axial thickness of the reaction front. It is taken as the depth of the gas-phase heat-release longitudinal profile (x-direction) at the channel center-line ($y = 3.5$ mm)

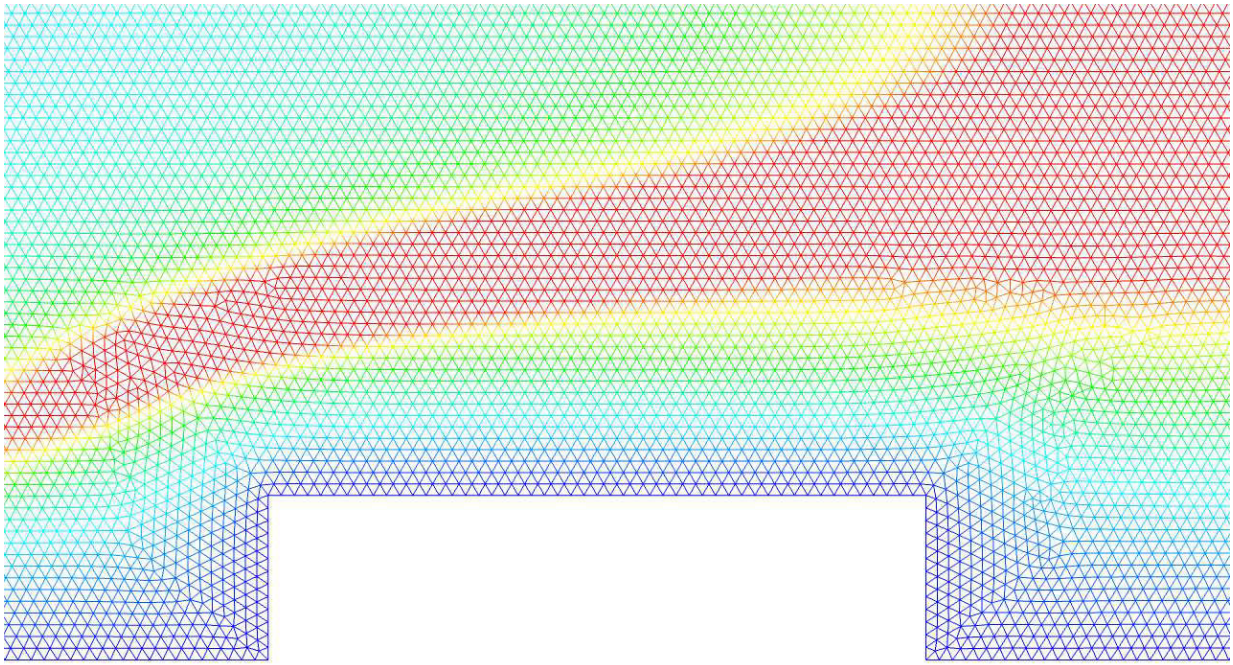

FIGURE 6.7: Spatial resolution of the gas-phase heat release rate near an obstacle

6.3 Impact on steady-state solution

6.3.1 Flame anchoring position

Figure 6.8 shows a comparison of the OH concentration maps for the studied cases with obstacles and cavities. The channel with planar walls is taken as reference. The observations are listed as follows:

- Impact of the obstacles and cavities :

  - (OS) and (CS): It is observed in Figures 6.7b and 6.7d that for both obstacles and cavities ,the segmented coating results in a flame that stabilize further upstream compared to the planar-wall channel (Figure 6.7a). However, the impact of obstacles is more notable compared to the cavities.
  - (OF) and (CF): Figures 6.7c and 6.7d show for both channels with obstacles and cavities that the continuous coating results in a flame that slightly stabilizes further downstream compared to the planar-wall case (Figure 6.7a). In particular, the obstacles yield an anchoring position closer to the position of reference compared to the cavities.

- Impact of the Pt-coating :

  - (OS) *vs.* (OF): Figures 6.7b and 6.7c indicate that applying a segmented coating to obstacles results in a flame that stabilize much further upstream compared to the continuous coating.
  - (CS) *vs.* (CF): Similarly, Figures 6.7d and 6.7e show that segmenting the coating in channels with cavities yields a flame anchoring position further upstream compared to the continuous coating. However, the difference between the two types of coating is less pronounced compared to the cases with obstacles ((OS) *vs.* (OF)).

- Finally, Figure 6.7b indicates that the case with obstacles and segmented Pt-coating (OS) exhibits the flame anchoring position that is the closest to the inlet.

The observed differences are quantified in Table 6.3 by comparing the positions at which the flames are stabilized normalized by the channel length and half-height. Noticeably, the channel with obstacles and segmented coating (OS) allows the flame to stabilize at a position that is $3 \times h_c$ closer to the inlet compared to the anchoring position for the planar-wall case. The same type of Pt-loading applied to the channel with cavities (CS) has a similar impact but is less pronounced. Compared to the planar-wall case, the CS case exhibits a flame that anchors one channel half-height further from the inlet whereas the impact of cavities and full coating (CF) is negligible.

The effect is moderate under the present conditions ($|x_{stab} - x_{stab}^{ref}|/L_c < 5\%$) but a significant impact could possibly be expected for a further optimized obstacle geometry or coating. The observations indicate that coating only the interior walls in a segmented manner allows the flame to stabilize further upstream. These findings could indicate that an OS solution could lead to more compact designs for catalytic converters, the anchoring of the flame closer to the inlet requiring a shorter coated section as compared to the one for the planar or cavity cases.

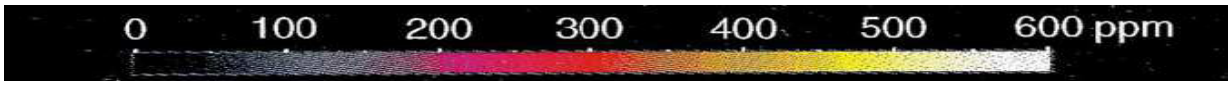

Reference: planar walls (case (a))

(A)

Obstacles and segmented coating (case OS)

(B)

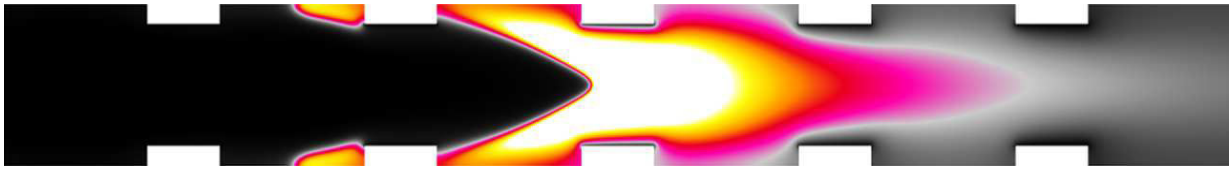

Obstacles and full coating (case OF)

(C)

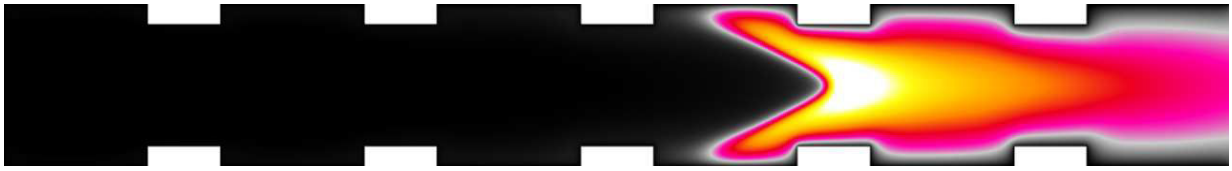

Cavities and segmented coating (case CS)

(D)

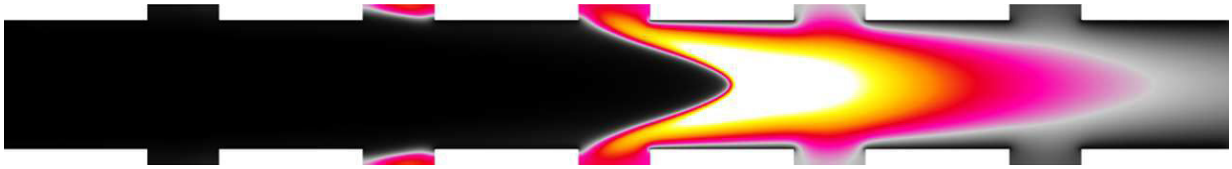

Cavities and full coating (case CF)

(E)

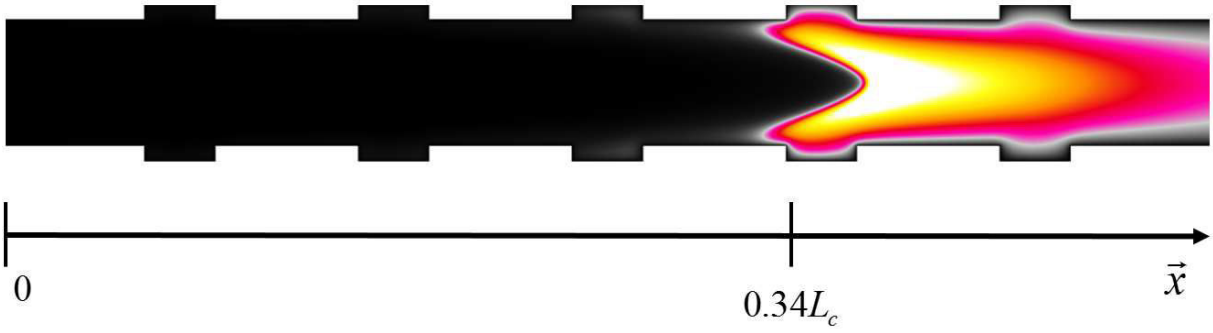

FIGURE 6.8: Comparison of the OH concentration maps: Effect of obstacle, cavities and coating type on the anchoring position.

Case	$\frac{x_{stab} - x_{stab}^{ref}}{L_c}$ (%)	$\frac{x_{stab} - x_{stab}^{ref}}{h_c}$(%)
OS	-4	-314
OF	+1.2	+86
CS	-0.8	-57
CF	+2.4	+17

TABLE 6.3: Comparison of the predicted stabilization positions of the flames for the catalytic channels with obstacles and cavities. x_{stab} is the axial distance between the inlet of the catalytic channel and the axial point where the OH concentration reaches its maximum. x_{stab}^{ref} refers to the planar wall case (a).

6.3.2 Fuel conversion rates

We define here the methane conversion rate, referred in what follows as MCR :

$$MCR = 100 \times \left(Y_{CH_4}|_{inlet} - \bar{Y}_{CH_4}(x)\right) / Y_{CH_4}|_{inlet} \tag{6.1}$$

$\bar{Y}_{CH_4}$ is the average methane mass fraction integrated along the channel height. The conversion distance is defined as the distance between the channel inlet and the position in the channel where MCR = 100. Figure 6.9 shows the MCR profiles. The the red lines indicate where the corners of the obstacles and cavities are located. The observations are listed as follows :

- Figure 6.9a shows in $0 \leq x \leq 0.26L_c$ that the MCR of both types of Pt-coating over obstacles is lower compared to the planar-wall channel before reaching the flame. At this part of the channel channel, the segmented coating particularly exhibits the lowest MCR values. Notably, the MCR of both OS and OF cases increases over the top edge of the obstacles as the obstacle corners are reached.
- Figure 6.9b shows in $0 \leq x \leq 0.26L_c$ that the MCR of both types of Pt-coating decreases as the cavity corners are reached. This decrease results in a slightly lower MCR valuers inside the cavities compared to the planar-wall channel. The MCR then increases outside of the cavities. The difference between the two types of coating is however less pronounced compared to the channel with obstacles.
- The segmented coating enables a shorter conversion distance than the full coating for both channels with obstacles and cavities.

The above observations could be explained as follows :

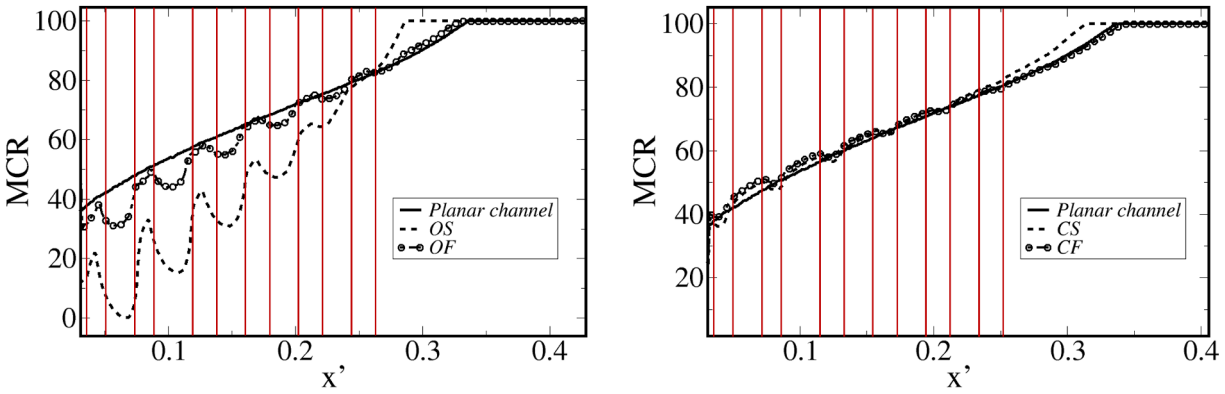

(A) Obstacles (B) Cavities

FIGURE 6.9: MCR for both types of Pt-coating : obstacles *vs.* cavities

- Full Pt coating presents a more important catalytic surface than the segmented one which may yield higher methane consumption through surface adsorption by the Pt active sites. This could explain why the MCR is higher in $0 \leq x \leq 0.26L_c$ if a continuous coating is applied, especially for the cases with obstacles (Fig 6.9a). The difference between the two types of coating is less notable for the cases with cavities (Fig 6.9b) probably because the coating ratio is much smaller in the OS case compared to CS case as described in Table 6.1.

- The shorter conversion distances resulting from the segmented coating could be explained by the fact that the flame stabilizes further upstream as shown in Figure 6.8. As gas-phase reactions might govern fuel consumption near the flame, conversion rates are likely to be shorter for the OS and CS cases for which the flame stabilizes closer to the inlet.

- regarding the channels with obstacles (OF and OF), the increase near the obstacle corners could be explained by the fact the channel section is restricted (Fig 6.4) which yields a shorter diffusive distance between the bulk fuel and the catalyst. This might lead to higher mass transfer to the reactive top edge of the obstacle. Unlikely, CS and CF cases exhibit decreasing MCR near the cavities because of a higher diffusive distance. The resulting wall mass transfers might be lower.

It is stressed that in order to assess the above presumptions, a further analysis is required by quantifying the interplay between the gas-phase and surface methane consumption.

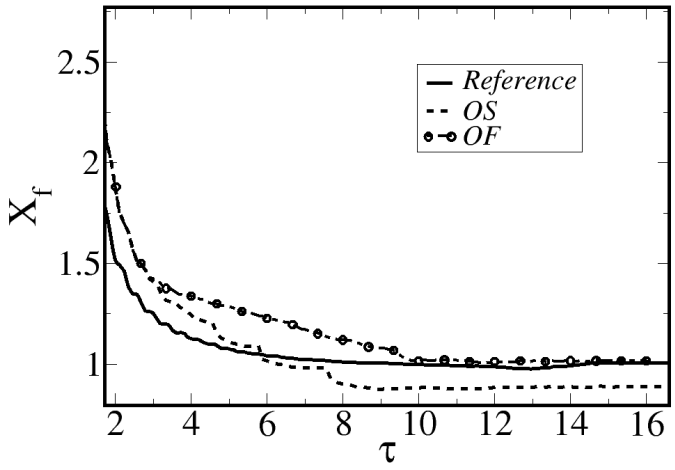

FIGURE 6.10: Temporal evolution of the normalized flame front positions X_f for the channels with obstacles

6.4 Impact on flame transients

The transient dynamics of the flame propagation are described in order to understand why introducing obstacles and segmented coating yields a flame anchoring position closer to the inlet, thus resulting in shorter conversion distances. The flame propagation dynamics in both segmented and full Pt-coated channels are presented for the configuration with obstacles only (OS and OF), as a similar behavior has been observed with cavities.

Figure 6.10 shows the overall temporal evolution of the normalized flame front position $X_f = x_{stab}/s^{ref}_{stab}$ for the cases with obstacles. Noticeably, the introduction of obstacles results in a propagation of the gas-phase reaction front that is slower compared to the planar channel, especially in the case of continuous coating (OF). In particular, the reaction front in the partially coated cases (OS) undergoes a sequence of abrupt variations starting from $t \approx 4\ t_{AI}$. At $t \approx 7.5\ t_{AI}$, the flame position of the OS case sharply decreases to anchor closer to the inlet compared to the planar channel and the OF case, as was shown in Figure 6.8. The OF case reaction front propagates smoothly and stabilizes at a channel position similar to the planar wall case.

In order to understand these time evolutions, the transient history of the gas-phase heat release maps and the channel center-line profiles of the OH mass fraction are described in what follows.

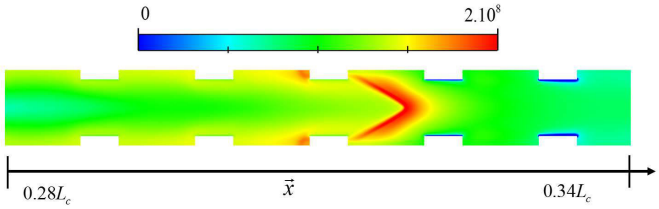

FIGURE 6.11: Propagation dynamic for the OS case at $t = 6.75\ t_{AI}$: Gas-phase heat release rate (log scale)

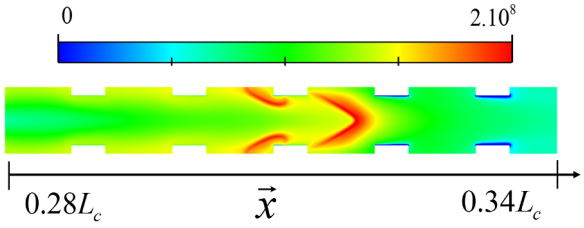

(A) Gas-phase heat release rate (log scale)

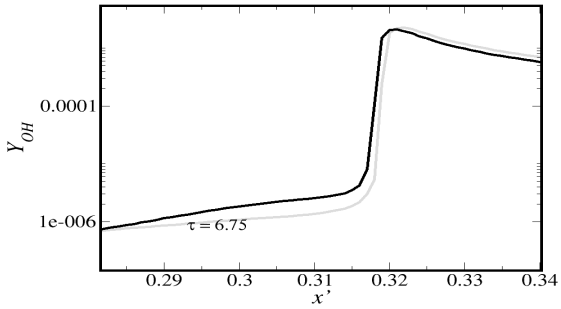

(B) Y_{OH} channel center-line profile

FIGURE 6.12: Propagation dynamic for the OS case at $t = 7\ t_{AI}$

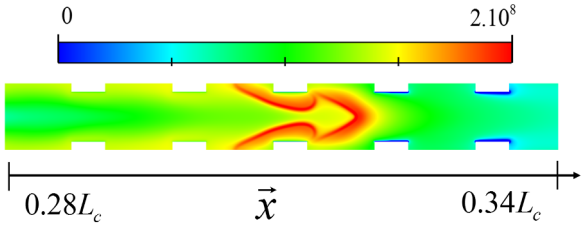

(A) Gas-phase heat release rate (log scale)

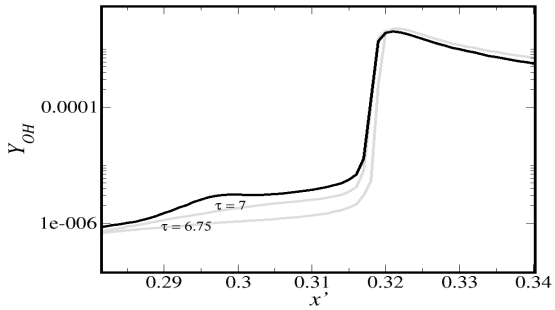

(B) Y_{OH} channel center-line profile

FIGURE 6.13: Propagation dynamic for the OS case at $t = 7.2\ t_{AI}$

6.4.1 Segmented Pt-coating (OS)

Figures 6.11 to 6.15 show for the OS case the transient history of the gaseous heat release maps and the OH mass fraction axial profiles at the channel center line. The grey OH lines stand for the past whereas

the thick black lines refer to the present. Figure 6.11 shows at $6.75t_{AI}$ that there is a gas-phase heat release spot in the first cavity corner located in the left side of the V-flame which is propagating upstream.

A few instants later, i.e. at $7t_{AI}$, Figure 6.12a shows that the heat release spot located in the cavity (observed in Figure 6.11) yields a reaction front. Therefore, two reaction fronts are observed which consist in the propagating V-flame located downstream the channel and the one emerging from the cavity located in the left side of the V-flame. The formation of a new reaction front inside the cavity coincides with a small increase in the OH mass fraction at $x = 0.3L_c$ as shown by Figure 6.12b.

A decrease of the V-flame sweep angles is observed at $7.2t_{AI}$ (Fig 6.13a). In the meanwhile, the reaction front emerging form the cavity comes across the V-flame as it propagates in the transverse direction. This yields a formation of a small OH peak at the channel center-line ($x = 0.3L_c$), as shown in Figure 6.13b.

As the two reaction fronts come across each other, Figure 6.14a indicates at $7.5t_{AI}$ that the reaction front which was emerging from the cavity results in a V-flame, whereas the tails of the V-flame that was initially propagating upstream the channel form a small kernel of fresh gases characterized by the trough (off-peak) in the OH center-line profile for $0.31 \leq x \leq 0.32$ (Fig 6.14b).

Finally, Figure 6.15a shows at $= 7.75t_{AI}$ that the initial flame undergoes complete extinction while the V-flame that was formed in the cavity propagates upstream as represented by the upstream convection of the OH peak shown in Figure 6.15b. From these observations, the following scenario can be proposed for the flame/obstacles interaction in the context of segmented coating :

As the V-flame propagates upstream the channel, the closest cavity could be preheated through heat diffusion which yields an ignition spot inside the cavity. This results in a reaction front that evolves into a V-flame which consumes the incoming fresh gases. Consequently, the initial propagating flame undergoes extinction. The flame does not propagate in a standard manner as in the planar-wall case: the dynamic corresponds to a sequence of flames resulting from the evolution of auto-ignition spots which might favor a further upstream propagation of the flame. The flame stabilizes when the local conditions are no longer promoting auto-ignition and the propagation of the resulting secondary front.

It is stressed that the abrupt decrease of the X_f profiles shown in Figure 6.10 are now explained by the reaction front emerging from the cavities.

6.4.2 Full Pt-coating

Figure 6.16 shows for the OF case the transient history of the gaseous heat release maps. At $9.85t_{AI}$ (Fig 6.16a), the gas-phase heat release spot in the first cavity corner is considerably less pronounced

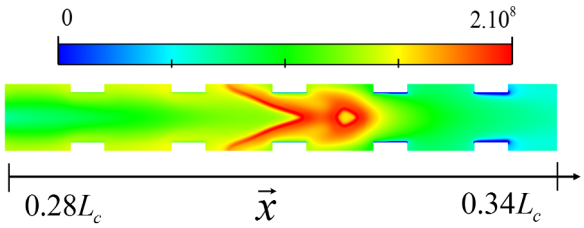

(A) Gas-phase heat release rate (log scale)

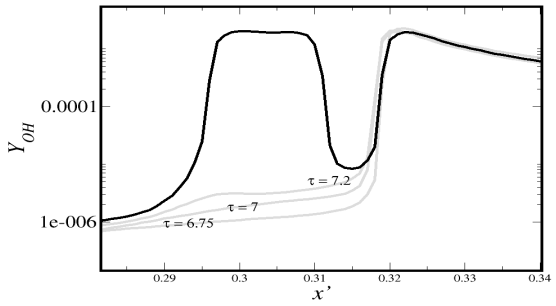

(B) Y_{OH} channel center-line profile

FIGURE 6.14: Propagation dynamic for the OS case at $t = 7.5\ t_{AI}$

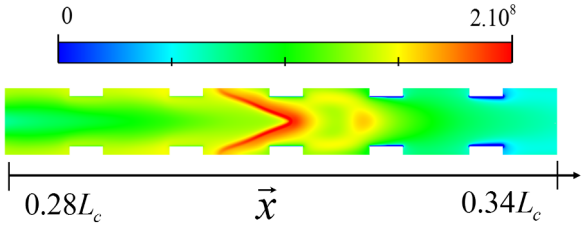

(A) Gas-phase heat release rate (log scale)

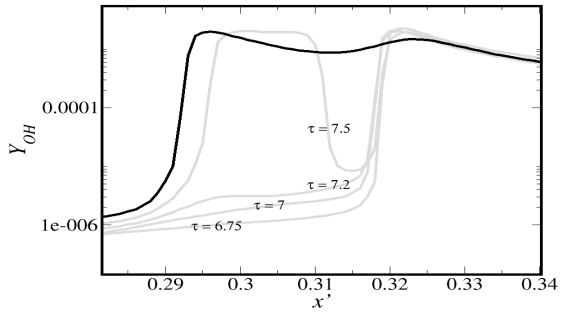

(B) Y_{OH} channel center-line profile

FIGURE 6.15: Propagation dynamic for the OS case at $t = 7.75\ t_{AI}$

compared to the OS case (Fig 6.11) as the V-flame propagates upstream. At $10.1t_{AI}$, the near-wall tails of the flame are extended toward the cavity (Fig 6.16b).

Figure 6.17 shows for the OF case the transient history of the gaseous heat release maps and the OH mass fraction axial profiles at the channel center-line. It is observed at $10.2t_{AI}$ that the flame propagates upstream (Fig 6.17a) in a standard manner. The OH peak has been progressively convected upstream for $9.75t_{AI} \leq t \leq 10.2t_{AI}$ as shown in Figure 6.17b.

It should be stressed that in Figures 6.16 and 6.17a, the heat release presents lower amplitudes than the segmented case. This could be explained by the fact that the level of adsorbed OH might be much higher tahn the levels of the segmented case, which yields lower gas-phase activity.

Comparably to the previous case, the following scenario can be proposed for the flame/obstacles interaction in the context of full coating :

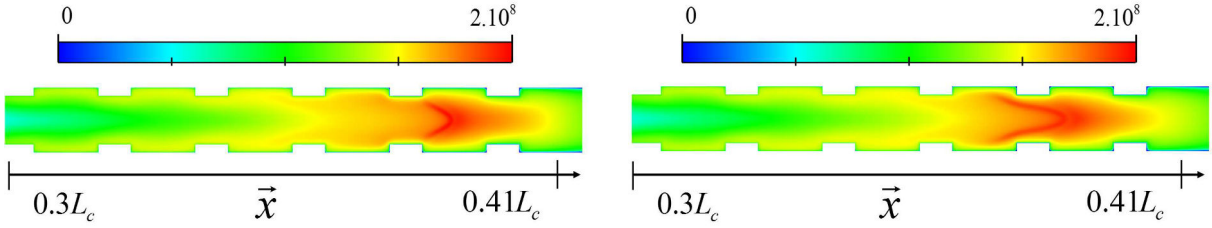

(A) $t = 9.85\ t_{AI}$ (B) $t = 10.1\ t_{AI}$

FIGURE 6.16: Propagation dynamic for the OF case: Gas-phase heat release rate (log scale)

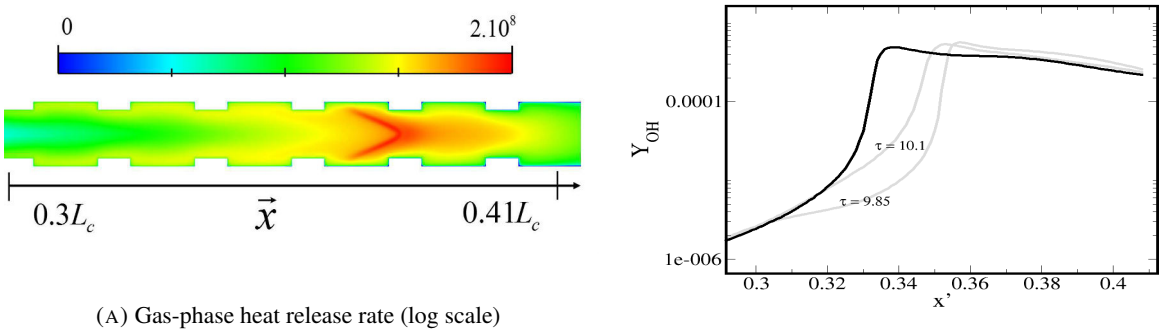

(A) Gas-phase heat release rate (log scale)

(B) Y_{OH} channel center-line profile

FIGURE 6.17: Propagation dynamic for the OF case at $t = 10.2\ t_{AI}$

In the case of channels with full Pt-coating, the chemical activity is less intense compared to the segmented catalyst. This results in conditions that are less favorable for the formation of auto-ignition spots in the cavities. The flame is therefore less likely to propagate further upstream. This could possibly explain why fully Pt-coated catalysts present flame anchoring positions that are located further downstream thus resulting in a shorter fuel conversion distance.

6.5 Conclusions

Four different wall configurations were explored, combining either obstacles or cavities, and a continuous or segmented Pt-coating. The analysis of these simulations indicated that the combination of obstacles with a segmented coating allowed achieving the increase of methane conversion rate, by allowing a flame anchoring further upstream as compared to the one of the initial planar channel. A first qualitative analysis showed that the benefit predicted for selectively coated obstacles could be explained by a specific transient flame dynamic resulting from successive auto-ignitions in the cavities between obstacles, allowing the

flame to propagate further upstream than with planar walls despite the higher flow velocities induced by the local flow section restrictions induced by the obstacles.

These findings can be considered to open very interesting perspectives for contributing to the optimization of the design of catalytic converters using the present modeling approach. Especially, the study of the impact of wall obstacles indicates the potential for contributing to further increase the efficiency of catalytic converters via the design of monolith geometries that would allow a more efficient and thus less costly usage of Pt-coating as a consequence of optimized interactions between the gas flow, gas phase chemistry and surface chemistry.

Chapter 7

Conclusions & Perspectives

The overall objective of the present work was to develop and validate a numerical approach based on 2D CFD for studying the detailed interactions between flow and heterogeneous chemistry found in particular in catalytic converters used in exhaust-gas after-treatment systems in the automotive industry.

In order to achieve this goal, a first key element was the formulation and integration into the AVBP CFD code of a numerical approach combining specific boundary conditions for reactive walls and ODE solvers for the gas phase and surface chemistry in order to allow accounting for detailed kinetics. The resulting approach was then validated by applying it to the simulation of two planar reactive channel flows, and comparing the predictions with experimental findings. Finally, the future potential of the resulting tool was illustrated by applying it to the study of the impact of non-planar catalytic walls, and of the induced flow modifications, on the ignition behavior and steady-state flame stabilization, in an attempt to identify first elements for increasing by design the conversion rate of catalytic devices.

The inclusion of chemical kinetics into the AVBP CFD code was addressed by introducing into the kinetic solver CLOE developed at IFPEN and which was initially dedicated to the resolution of gas-phase kinetic schemes. For the purpose of addressing the heterogeneous chemistry found in catalytic converters, the kinetic solver was adapted during this thesis to allow accounting for surface chemistry via the introduction of the required set of equations and their resolution, as detailed in the third Chapter. In order to properly represent the interactions between surface reactions and the gas-phase flow and chemistry, a novel reactive wall boundary condition was derived from the energy balance that account for the resulting exchanges of energy at the wall. Special attention was paid to ensure that the generic formulation properly degenerates to standard inert adiabatic and isothermal wall boundary conditions in the absence of surface chemistry.

In order to validate the inclusion of detailed gas phase and surface chemistry into AVBP, the resulting tool was applied to the simulation of a zero-dimensional heterogeneous reactor. It is composed of one computational cell whose boundaries are all set to be reactive walls, resulting in a simple closed volume reactor exhibiting gas phase and surface reactions, but no molecular or convective transport. The predicted temporal evolutions of temperature, gas-phase and surface species was shown to perfectly match the ones obtained with the reference kinetic solver SENKIN of the CHEMKIN library [41], thus validating the integration of detailed heterogeneous chemistry and related wall boundary conditions into AVBP.

The developed approach was then applied to the simulation of a one-dimensional transient heterogeneous case in order to illustrate the interaction between molecular gas-phase diffusion and surface reactions. It consisted of a quiescent CO_2/O_2 mixture initiated next to a carbonaceous reactive wall. As CO_2 and O_2 diffuse to the reactive wall and interact with solid carbon through surface reactions, CO species is produced and diffuses away from the wall; initiating a gas-phase CO/O_2 combustion. The resulting interaction between the gas-phase and the surface reactions resulted in an original dynamic. These results, as well as the underlying formulation of reactive wall boundary conditions, led to the publication of an article in the International Journal of Heat and Mass transfer (IJHMT) [26].

In a next step, the developed approach was applied to the simulation of a two-dimensional configuration experimentally studied by Dogwiler *et al.* [27]. It consists of a flow of a lean premixed CH_4/air mixture over a Pt-coated planar wall in a meso-scale channel similar to those found in monoliths of automotive after-treatment systems. The primary purpose of this study was to validate the predictions obtained with the developed simulation tool against experimental evidence in a realistic configuration involving both transport phenomena and heterogeneous chemistry. The following main conclusions can be drawn from these simulations:

- The developed approach proved to be able of reproducing main features of the combustion observed for different operating points. The V-shaped flames and the sweep angles were qualitatively well reproduced, as were the anchoring position of the flames once steady-state was reached. However, quantitative comparisons against OH measurements showed some discrepancies. Different factors that could explain the latter were explored:
  - Experimental uncertainty concerning the wall temperature and channel inlet conditions were found to have a small impact to be considered as sources for the observed discrepancies concerning OH levels;
  - An *a priori* analysis indicated that the simplifying assumptions made in the present work concerning molecular transport certainly a one source for the overprediction of OH levels by the performed simulations.

  - Given the high surface to volume ratio encountered within the studied meso-scale channel and the high wall temperature, neglecting radiative heat transfer as done in the present work was also identified as a possible source for discrepancies in temperature levels, and thus OH;
  - Uncertainties concerning the chemical kinetics used for both gas-phase and surface reaction certainly are another major source of discrepancies.

  It was not possible to address the two latter points in the present work. However these aspects would require careful attention in order to ensure reliable predictions in future studies.

- Surface reactions were found to have a stabilizing effect on the flame shape and stabilization under the studied conditions. This was indirectly confirmed by performing simulations where surface chemistry was numerically deactivated, resulting in an oscillatory asymmetric slant-shape flame, which anchored further upstream in steady-state than observed with reactive walls. This indicated the *a priori* ability of the developed tool to capture the possible instabilities encountered in meso-scale channels with inert walls and the stabilizing effects of surface reactions.

Finally, the developed tool was applied to explore the impact of introducing wall obstacles on the conversion rate of catalytic devices. In absence of available experimental results, this was performed using the reference operating point of the already studied Dogwiler *et al.* case. Four different wall configurations were explored, combining either obstacles or cavities, and a continuous or only a partial (selective) Pt-coating. The analysis of these simulations indicated that the combination of obstacles with a segmented coating allowed achieving the desired increase of methane conversion rate, as a direct consequence of allowing a flame anchoring closer to the channel inlet as compared to the one of the initial planar channel. A first qualitative analysis showed that the benefit predicted for selectively coated obstacles could be explained by a specific transient flame dynamic resulting from successive auto-ignitions in the cavities between obstacles, allowing the flame to propagate further upstream than with planar walls despite the higher flow velocities induced by the local flow section restrictions induced by the obstacles.

Despite the fact that much more research work will be required to yield a fully predictive and reliable tool and simulation methodology, the developments achieved in the present thesis can be considered to open very interesting perspectives for contributing to the optimization of the design of catalytic converters using 2D CFD and detailed heterogeneous chemistry. In particular, the study of the impact of wall obstacles indicates the potential for contributing to further increase the efficiency of catalytic converters via the design of monolith geometries that would allow a more efficient and thus less costly usage of Pt-coating as a consequence of optimized interactions between the gas flow, gas phase chemistry and surface chemistry.

In this context, the presented work can only be considered as an exploratory qualitative work, whose practical implications are necessarily limited by different key simplifying assumptions. Among those, future research would have to address amongst others:

- The detailed thermal state of the channel walls. In real applications the wall temperatures are not controlled, as was highlighted in the studies of karagiannidis *et al* [113] and Brambilla *et al.* [92].This could require in particular setting up a conjugate heat transfer approach, coupling the CFD code with a tool simulating the heat conduction in the solid walls. This would be required to be able to address amongst others the heating up of the catalysts, the temporal and spatial evolution of wall temperatures, the possible appearance of hot spots under certain conditions, or interactions between neighboring channels. In this context, it would certainly also be necessary to include radiative heat transfers between the walls and the gases, and potentially adapt the wall boundary conditions for that.

- Means to render a non- homogeneous coating or surface state. In this context, a proper description of the porous catalyst support could be achieved by resolving gas-phase transport inside the porous layer as was explored by Maffei *et al.* [114]. Furthermore, this could be complemented by models to account for fouling or the formation and effect of wall deposits, as such local phenomena will have a first order impact on the conversion rates and practical usability.

- The complexity of the burnt gases composition resulting from the combustion of higher order hydrocarbons as found in real applications and from their evolution in the exhaust ducts before reaching the catalytic converter. In the present work, only lower order hydrocarbon fuels and their products were addressed, for which the chemical kinetics are rather well known.

In this context, it would be of primary importance to set-up and acquire an as much detailed as possible experimental database allowing to carefully validate the different models to be developed. This would in particular include quantitative measurements of gas flow fields, gas and wall temperatures, and chemical species in the gas and at the wall, during both initiation and stabilized phases of realistic monolith channel configurations and operating conditions.

Finally, detailed 3D CFD studies could be exploited to support the formulation of reduced models for catalytic converters that could be included into system simulations for full EGA systems, and thus contribute to their overall optimization and to the development of model-based control strategies.

Bibliography

[1] http://hmf.enseeiht.fr/travaux/CD0708/beiep/8/html/introduction.html, 2015. xii, 1

[2] http://www.preciousmetals.umicore.com/recyclables/SAC/catalyticconverter/. xii, 2

[3] IFP Trainig. http://www.ifptraining.fr/. xii, 2

[4] Marcus FM Zwinkels, Sven G Järås, P Govind Menon, and Timothy A Griffin. Catalytic materials for high-temperature combustion. *Catalysis Reviews–Science and Engineering*, 35(3):319–358, 1993. xii, 3, 106

[5] EMITEC. http://www.emitec.com/en/technology/catalyst-substrates. xii, 4

[6] John Mantzaras. New directions in advanced modeling and in situ measurements near reacting surfaces. *Flow, turbulence and combustion*, 90(4):681–707, 2013. xii, 4, 5, 72

[7] Nicolas Lamarque. *Schémas numériques et conditions limites pour la simulation aux grandes échelles de la combustion diphasique dans les foyers d'hélicoptère.* PhD thesis, Institut National Polytechnique de Toulouse-INPT, 2007. xii, 14

[8] Eur-lex access to european union law. http://eur-lex.europa.eu/legal-content/EN, 2015. 1

[9] Tao Tang, Dongxiao Cao, Jun Zhang, Yan-guang Zhao, and Shi-jin Shuai. Experimental study of catalyzed diesel particulate filter with exhaust fuel injection system for heavy-duty diesel engines. Technical report, SAE Technical Paper, 2014. 1

[10] Pascal Granger and Vasile I Parvulescu. Catalytic no x abatement systems for mobile sources: from three-way to lean burn after-treatment technologies. *Chemical Reviews*, 111(5):3155–3207, 2011. 1

[11] April Russell and William S Epling. Diesel oxidation catalysts. *Catalysis Reviews*, 53(4):337–423, 2011. 1

[12] WEI JAMES. Catalysis for motor vehicle emissions. *Advances in catalysis*, 24:57, 1975. 2

[13] Larry C Young and Bruce A Finlayson. Mathematical models of the monolith catalytic converter: Part ii. application to automobile exhaust. *AIChE Journal*, 22(2):343–353, 1976. 2

[14] WC Pfefferle and LD Pfefferle. Catalytically stabilized combustion. *Progress in energy and combustion science*, 12(1):25–41, 1986. 2, 70

[15] S Lennart Andersson and Nils Herman Schoeoen. Methods to increase the efficiency of a metallic monolithic catalyst. *Industrial & engineering chemistry research*, 32(6):1081–1086, 1993. 3, 106

[16] Anna M Holmgren. Enhanced mass transfer in monolith catalysts with bumps on the channel walls. *Industrial & engineering chemistry research*, 38(5):2091–2097, 1999. 3

[17] Laxminarayan L. Raja, Robert J. Kee, and Linda R. Petzold. Simulation of the transient, compressible, gas-dynamic behavior of catalytic-combustion ignition in stagnation flows. *Symposium (International) on Combustion*, 27(2):2249 – 2257, 1998. ISSN 0082-0784. 3, 29, 44

[18] Haifa Belaid-Saleh, Stephane Jay, Julian Kashdan, Cyprien Ternel, and Christine Mounaïm-Rousselle. Numerical and experimental investigation of combustion regimes in a dual fuel engine. Technical report, SAE Technical Paper, 2013. 4

[19] Josef Stefan. Über das gleichgewicht und die bewegung, insbesondere die diffusion von gasgemengen. *Sitzber. Akad. Wiss. Wien*, 63:63–124, 1871. 5

[20] Raweewan Klaewkla, Matthias Arend, and Wolfgang F Hoelderich. *A review of mass transfer controlling the reaction rate in heterogeneous catalytic systems*. INTECH Open Access Publisher, 2011. 5

[21] E. A. Hamza. Suction and injection effects on a similar flow between parallel plates. *Journal of Physics D: Applied Physics*, 32(4):656–663, 1999. 5, 46

[22] Olaf Deutschmann, R Schmidt, Frank Behrendt, and J Warnat. Numerical modeling of catalytic ignition. In *Symposium (international) on combustion*, volume 26, pages 1747–1754. Elsevier, 1996. 5, 26, 40, 44, 79, 80, 90

[23] Renate Schwiedernoch, Steffen Tischer, Chrys Correa, and Olaf Deutschmann. Experimental and numerical study on the transient behavior of partial oxidation of methane in a catalytic monolith. *Chemical Engineering Science*, 58(3):633–642, 2003. 5

[24] Olivier Cabrit. *Wall modeling of the flow inside solid rocket motor nozzles*. PhD thesis, Montpellier 2, 2009. 6, 30, 45

[25] Olivier Cabrit and Franck Nicoud. Direct numerical simulation of a reacting turbulent channel flow with thermochemical ablation. *Journal of Turbulence*, 11(44):1–33, 2010. 6, 29, 30

[26] Adam M Chabane, Karine Truffin, André Nicolle, Franck Nicoud, Olivier Cabrit, and Christian Angelberger. Direct numerical simulation of combustion near a carbonaceous surface in a quiescent flow. *International Journal of Heat and Mass Transfer*, 84:130–148, 2015. 7, 43, 45, 121

[27] Urs Dogwiler, John Mantzaras, Peter Benz, Beat Kaeppeli, Rolf Bombach, and Andreas Arnold. Homogeneous ignition of methane-air mixtures over platinum: Comparison of measurements and detailed numerical predictions. In *Symposium (International) on Combustion*, volume 27, pages 2275–2282. Elsevier, 1998. 7, 70, 71, 72, 74, 79, 80, 102, 103, 121

[28] Thierry Poinsot and Denis Veynante. *Theoretical and numerical combustion*. RT Edwards, Inc., 2005. 9

[29] FA Williams. Combustion theory, the fundamental theory of chemically reacting systems, 1985. 11

[30] Joseph O Hirschfelder, Charles F Curtiss, Robert Byron Bird, et al. *Molecular theory of gases and liquids*, volume 26. Wiley New York, 1954. 11, 49, 63

[31] Kenneth K Kuo. *Principles of combustion*. Wiley New York et al., 1986. 13, 27, 31

[32] T Schoenfeld. The avbp handbook. `http://www.cerfacs.fr/4-26334-The-AVBP-code.php`, 2008. 13

[33] Peter D Lax and Burton Wendroff. Difference schemes for hyperbolic equations with high order of accuracy. *Communications on pure and applied mathematics*, 17(3):381–398, 1964. 14, 55

[34] Peter Lax and Burton Wendroff. Systems of conservation laws. *Communications on Pure and Applied mathematics*, 13(2):217–237, 1960. 55

[35] Charles Hirsch. *Numerical Computation of Internal and External Flows: The Fundamentals of Computational Fluid Dynamics: The Fundamentals of Computational Fluid Dynamics*, volume 1. Butterworth-Heinemann, 2007. 14

[36] Bruno Sportisse. An analysis of operator splitting techniques in the stiff case. *Journal of Computational Physics*, 161(1):140–168, 2000. 15

[37] Peter N Brown, Alan C Hindmarsh, and Linda R Petzold. Using krylov methods in the solution of large-scale differential-algebraic systems. *SIAM Journal on Scientific Computing*, 15(6):1467–1488, 1994. 18

[38] Makis Caracotsios and Warren E Stewart. Sensitivity analysis of initial value problems with mixed odes and algebraic equations. *Computers & Chemical Engineering*, 9(4):359–365, 1985. 18

[39] AC Hindmarsh and LR Petzold. Lsodar, ordinary differential equation solver for stiff or non-stiff system with root-finding. 2005. 18

[40] Peter N Brown, George D Byrne, and Alan C Hindmarsh. Vode: A variable-coefficient ode solver. *SIAM journal on scientific and statistical computing*, 10(5):1038–1051, 1989. 18, 20, 40, 80

[41] RJ Kee, FM Rupley, JA Miller, ME Coltrin, JF Grcar, E Meeks, et al. Theory manual chemkin release 4.0. 1, reaction design, 2004. 20, 39, 121

[42] Wayne K Metcalfe, Sinéad M Burke, Syed S Ahmed, and Henry J Curran. A hierarchical and comparative kinetic modeling study of c1- c2 hydrocarbon and oxygenated fuels. *International Journal of Chemical Kinetics*, 45(10):638–675, 2013. 20, 40, 79, 90

[43] https://mon-partage.fr/f/G0j67lg6/. 20, 79

[44] Olaf Deutschmann. Interactions between transport and chemistry in catalytic reactors. *Ruprecht-Karls-Universität Heidelberg, 2001*, 2001. 24, 26, 27, 29

[45] O Deutschmann, LI Maier, U Riedel, AH Stroemman, and RW Dibble. Hydrogen assisted catalytic combustion of methane on platinum. *Catalysis Today*, 59(1):141–150, 2000.

[46] H. Motz and H. Wise. In *Journal of Chemical Physics*, volume 32, 1960. 26

[47] Michael Elliott Coltrin, HK Moffat, RJ Kee, and FM Rupley. Creslaf (version 4. 0): A fortran program for modeling laminar, chemically reacting, boundary-layer flow in cylindrical or planar channels. Technical report, Sandia National Labs., Albuquerque, NM (United States); Sandia National Labs., Livermore, CA (United States), 1993. 29

[48] http://www.detchem.com/mechanisms/sm_Pt_CH4_O2_1.2_CHEMKIN, 1995. 40, 79, 80, 90

[49] RK Eckhoff. Prevention and mitigation of dust explosions in the process industries: A survey of recent research and development. *Journal of loss prevention in the process industries*, 9(1):3–20, 1996. 43

[50] J. Bouillard, A. Vignes, O. Dufaud, L. Perrin, and D. Thomas. Ignition and explosion risks of nanopowders. *Journal of Hazardous Materials*, 181(1-3):873 – 880, 2010. ISSN 0304-3894. 43

[51] Ao Makino and CK Law. Ignition and extinction of co flame over a carbon rod. *Combustion Science and Technology*, 73(4-6):589–615, 1990. 43, 44

[52] Jerry C. Lee, Richard A. Yetter, and Frederick L. Dryer. Transient numerical modeling of carbon particle ignition and oxidation. *Combustion and Flame*, 101(4):387 – 398, 1995. ISSN 0010-2180. 44

[53] Paul A. Libby and Thomas R. Blake. Burning carbon particles in the presence of water vapor. *Combustion and Flame*, 41:123 – 147, 1981. ISSN 0010-2180.

[54] A. Makino and C.K. Law. Quasi-steady and transient combustion of a carbon particle: Theory and experimental comparisons. *Symposium (International) on Combustion*, 21(1):183 – 191, 1988. ISSN 0082-0784. 43, 44

[55] Ethan S Hecht. *Single particle studies of pulverized coal oxy-combustion*. PhD thesis, The University of Utah, 2013. 44

[56] Daehee Kim, Sangmin Choi, Christopher R. Shaddix, and Manfred Geier. Effect of CO2 gasification reaction on char particle combustion in oxy-fuel conditions. *Fuel*, 120:130 – 140, 2014. ISSN 0016-2361. 44

[57] Ethan S. Hecht, Christopher R. Shaddix, Manfred Geier, Alejandro Molina, and Brian S. Haynes. Effect of CO2 and steam gasification reactions on the oxy-combustion of pulverized coal char. *Combustion and Flame*, 159(11):3437 – 3447, 2012. ISSN 0010-2180. 44, 55

[58] Silvia Granata, Tiziano Faravelli, and Eliseo Ranzi. A wide range kinetic modeling study of the pyrolysis and combustion of naphthenes. *Combustion and Flame*, 132(3):533 – 544, 2003. ISSN 0010-2180. 44

[59] Terry F Wall, Gui-su Liu, Hong-wei Wu, Daniel G Roberts, Kathy E Benfell, Sushil Gupta, John A Lucas, and David J Harris. The effects of pressure on coal reactions during pulverised coal combustion and gasification. *Progress in Energy and Combustion Science*, 28(5):405–433, 2002. 44

[60] Lei Chen, Sze Zheng Yong, and Ahmed F. Ghoniem. Oxy-fuel combustion of pulverized coal: Characterization, fundamentals, stabilization and cfd modeling. *Progress in Energy and Combustion Science*, 38(2):156 – 214, 2012. ISSN 0360-1285. 44

[61] Paul A. Libby and Thomas R. Blake. Theoretical study of burning carbon particles. *Combustion and Flame*, 36:139 – 169, 1979. ISSN 0010-2180. 44, 46, 52

[62] Guangwei Huang, Francis J Vastola, and Alan W Scaroni. Temperature gradients in the gas phase surrounding pyrolyzing and burning coal particles. *Energy & fuels*, 2(4):385–390, 1988. 44

[63] Kirsten Leistner, Andre Nicolle, David Berthout, and Patrick da Costa. Kinetic modelling of the oxidation of a wide range of carbon materials. *Combustion and Flame*, 159(1):64 – 76, 2012. ISSN 0010-2180. 44, 55, 56

[64] Robert H. Essenhigh, Mahendra K. Misra, and David W. Shaw. Ignition of coal particles: A review. *Combustion and Flame*, 77(1):3 – 30, 1989. ISSN 0010-2180. 44

[65] Atsushi Makino and Chung K. Law. An analysis of the transient combustion and burnout time of carbon particles. *Proceedings of the Combustion Institute*, 32(2):2067 – 2074, 2009. ISSN 1540-7489. 44

[66] D.B. Spalding. The prediction of mass transfer rates when equilibrium does not prevail at the phase interface. *International Journal of Heat and Mass Transfer*, 2(4):283 – 313, 1961. ISSN 0017-9310. 44

[67] Chun Zou, Lei Cai, and Chuguang Zheng. Numerical research on the homogeneous/heterogeneous ignition process of pulverized coal in oxy-fuel combustion. *International Journal of Heat and Mass Transfer*, 73:207 – 216, 2014. 44

[68] Ethan S Hecht, Christopher R Shaddix, and JoAnn S Lighty. Analysis of the errors associated with typical pulverized coal char combustion modeling assumptions for oxy-fuel combustion. *Combustion and Flame*, 160(8):1499–1509, 2013. 44

[69] Mingchuan Zhang, Juan Yu, and Xuchang Xu. A new flame sheet model to reflect the influence of the oxidation of CO on the combustion of a carbon particle. *Combustion and Flame*, 143(3):150 – 158, 2005. ISSN 0010-2180. 44

[70] Robert Lewtak and Aleksandra Milewska. Application of different diffusion approaches in oxy-fuel combustion of single coal char particles. *Fuel*, 113:844 – 853, 2013. ISSN 0016-2361. 44

[71] Moshe Matalon. Complete burning and extinction of a carbon particle in an oxidizing atmosphere. *Combustion Science and Technology*, 24(3-4):115–127, 1980. 44

[72] Guillaume Moula. *Analyse multi-échelle d'un écoulement réactif gaz-particule en lit fluidisé dense*. PhD thesis, 2012. 45

[73] H. Schlichting and K. Gersten. *Boundary Layer Theory*. Springer-Verlag, Berlin Heidelberg, Germany, 8th edition, 2000. 46

[74] J. C. Y. Koh and J. P. Hartnett. Skin friction and heat transfer for incompressible laminar flow over porous wedges with suction and variable wall temperature. *Int. J. Heat Mass Transfer*, 2(3): 185–198, April 1961. 46

[75] Daniel E Rosner. Convective diffusion as an intruder in kinetic studies of surface catalyzed reactions. *AIAA Journal*, 2(4):593–610, 1964. 46

[76] Lian Duan and M Pino Martín. Procedure to validate direct numerical simulations of wall-bounded turbulence including finite-rate reactions. *AIAA Journal*, 47(1):244–251, 2009. 46

[77] A Ern and V Giovangigli. Eglib: A general-purpose fortran library for multicomponent transport property evaluation. *CERMICS, ENPC and Centre de Mathématiques Appliquées, CNRS*, 2000. 53, 64, 85, 86, 87

[78] F. Nicoud L. Selle and T. Poinsot. Actual impedance of nonreflecting boundary conditions: Implications for computation of resonators. *AIAA Journal*, 42(5):958 – 964, 2007. 54, 74, 75

[79] David H. Rudy and John C. Strikwerda. A nonreflecting outflow boundary condition for subsonic navier-stokes calculations. *Journal of Computational Physics*, 36(1):55 – 70, 1980. ISSN 0021-9991. 54, 74, 75

[80] P.I. Crumpton, J.A. Mackenzie, and K.W. Morton. Cell vertex algorithms for the compressible navier-stokes equations. *Journal of Computational Physics*, 109(1):1 – 15, 1993. ISSN 0021-9991. 55

[81] Vincent Moureau and André René. *Simulation aux grandes échelles de l'aérodynamique interne des moteurs à piston*. PhD thesis, Châtenay-Malabry, Ecole Centrale Paris, 2004. 55

[82] Olivier Colin and Michael Rudgyard. Development of high-order taylor–galerkin schemes for les. *Journal of Computational Physics*, 162(2):338–371, 2000. 55

[83] Ethan S Hecht, Christopher R Shaddix, Alejandro Molina, and Brian S Haynes. Effect of co2 gasification reaction on oxy-combustion of pulverized coal char. *Proceedings of the combustion institute*, 33(2):1699–1706, 2011. 55

[84] Ljubisa R Radovic, Hong Jiang, and Anthony A Lizzio. A transient kinetics study of char gasification in carbon dioxide and oxygen. *Energy & fuels*, 5(1):68–74, 1991. 55

[85] Robert H Hurt and Joseph M Calo. Semi-global intrinsic kinetics for char combustion modeling. *Combustion and Flame*, 125(3):1138 – 1149, 2001. ISSN 0010-2180. 55

[86] Valerio Cozzani. Reactivity in oxygen and carbon dioxide of char formed in the pyrolysis of refuse-derived fuel. *Industrial and Engineering Chemistry Research*, 39(4):864–872, 2000. 55, 56

[87] Michael E Coltrin, Robert J Kee, Fran M Rupley, and Ellen Meeks. Surface chemkin III: A fortran package for analyzing heterogeneous chemical kinetics at a solid-surface-gas-phase interface. *Sandia National Laboratories Report SAND96-8217*, 1996. 55

[88] Theodore A Brabbs, Frank E Belles, and Steven A Zlatarich. Shock-tube study of carbon dioxide dissociation rate. *The Journal of Chemical Physics*, 38(8):1939–1944, 1963. 56

[89] G. Miessen, F. Behrendt, O. Deutschmann, and J. Warnatz. Numerical studies of the heterogeneous combustion of char using detailed chemistry. *Chemosphere*, 42(57):609 – 613, 2001. ISSN 0045-6535. Proceedings of the 6th Intl Congress on Toxic combustion. 56

[90] Atsushi Makino. An attempt for applying formulation of the carbon combustion in the stagnation flowfield to some experimental comparisons related to the boundary layer combustion. *Combustion and Flame*, 161(6):1537 – 1546, 2014. 59

[91] C. F. Curtiss and R. Byron Bird. Multicomponent diffusion. *Industrial and Engineering Chemistry Research*, 38(7):2515–2522, 1999. 63

[92] Andrea Brambilla, Marco Schultze, Christos E Frouzakis, John Mantzaras, Rolf Bombach, and Konstantinos Boulouchos. An experimental and numerical investigation of premixed syngas combustion dynamics in mesoscale channels with controlled wall temperature profiles. *Proceedings of the Combustion Institute*, 35(3):3429–3437, 2015. 72, 123

[93] Michael Reinke, John Mantzaras, Rolf Bombach, Sabine Schenker, and Andreas Inauen. Gas phase chemistry in catalytic combustion of methane/air mixtures over platinum at pressures of 1 to 16 bar. *Combustion and flame*, 141(4):448–468, 2005.

[94] Xin Zheng, Marco Schultze, John Mantzaras, and Rolf Bombach. Effects of hydrogen addition on the catalytic oxidation of carbon monoxide over platinum at power generation relevant temperatures. *Proceedings of the Combustion Institute*, 34(2):3343 – 3350, 2013. ISSN 1540-7489.

[95] Xin Zheng, John Mantzaras, and Rolf Bombach. Hetero-/homogeneous combustion of ethane/air mixtures over platinum at pressures up to 14bar. *Proceedings of the Combustion Institute*, 34(2): 2279–2287, 2013. 72

[96] PM Struk, JS T'ien, FJ Miller, and DL Dietrich. Transient numerical modeling of catalytic channels using a quasi-steady gas phase. *Chemical Engineering Science*, 119:158–173, 2014. 78

[97] G Groppi, A Belloli, E Tronconi, and P Forzatti. A comparison of lumped and distributed models of monolith catalytic combustors. *Chemical Engineering Science*, 50(17):2705–2715, 1995.

[98] G Groppi, A Belloli, E Tronconi, and P Forzatti. Analysis of multidimensional models of monolith catalysts for hybrid combustors. *AIChE Journal*, 41(10):2250–2260, 1995. 78

[99] Perrine Pepiot-Desjardins and Heinz Pitsch. An efficient error-propagation-based reduction method for large chemical kinetic mechanisms. *Combustion and Flame*, 154(1):67–81, 2008. 79

[100] Damien Poitou. *Modélisation du rayonnement dans la simulation aux grandes échelles de la combustion turbulente*. PhD thesis, Ph. D. thesis, Institut National Polytechnique de Toulouse, Toulouse, France, 2009. 91

[101] Chien-Hsiung Tsai. The asymmetric behavior of steady laminar flame propagation in ducts. *Combustion Science and Technology*, 180(3):533–545, 2008. 102

[102] Daniel Fernández-Galisteo, Carmen Jiménez, Mario Sánchez-Sanz, and Vadim N Kurdyumov. The differential diffusion effect of the intermediate species on the stability of premixed flames propagating in microchannels. *Combustion Theory and Modelling*, 18(4-5):582–605, 2014. 102

[103] Vadim N Kurdyumov. Lewis number effect on the propagation of premixed flames in narrow adiabatic channels: Symmetric and non-symmetric flames and their linear stability analysis. *Combustion and Flame*, 158(7):1307–1317, 2011.

[104] Vadim N Kurdyumov and Carmen Jiménez. Propagation of symmetric and non-symmetric premixed flames in narrow channels: Influence of conductive heat-losses. *Combustion and Flame*, 161 (4):927–936, 2014. 102

[105] Gianmarco Pizza, John Mantzaras, and Christos E Frouzakis. Flame dynamics in catalytic and non-catalytic mesoscale microreactors. *Catalysis Today*, 155(1):123–130, 2010. 102, 108

[106] Yueh-Heng Li, Guan-Bang Chen, Fang-Hsien Wu, Tsarng-Sheng Cheng, and Yei-Chin Chao. Effects of catalyst segmentation with cavities on combustion enhancement of blended fuels in a micro channel. *Combustion and Flame*, 159(4):1644–1651, 2012. 105, 106

[107] Yueh-Heng Li, Guan-Bang Chen, Hung-Wei Hsu, and Yei-Chin Chao. Enhancement of methane combustion in microchannels: effects of catalyst segmentation and cavities. *Chemical Engineering Journal*, 160(2):715–722, 2010. 105, 106

[108] PS Barbato, V Di Sarli, G Landi, and A Di Benedetto. Partially coated lamno3 monoliths as high pressure ch4 catalytic combustor. 105

[109] A Di Benedetto, G Landi, V Di Sarli, PS Barbato, Raffaele Pirone, and G Russo. Methane catalytic combustion under pressure. *Catalysis Today*, 197(1):206–213, 2012. 105

[110] Jingyu Ran, Liya Li, Xuesen Du, Ruirui Wang, Wenli Pan, and Weimin Tang. Numerical investigations on characteristics of methane catalytic combustion in micro-channels with a concave or convex wall cavity. *Energy Conversion and Management*, 97:188–195, 2015. 105

[111] Kenneth W Aniolek. A CFD study of diesel substrate channels with differing wall geometries. *SAE Technical Paper*, pages 01–0152, 2004. 106

[112] Jianlong Wan, Aiwu Fan, Yi Liu, Hong Yao, Wei Liu, Xiaolong Gou, and Daiqing Zhao. Experimental investigation and numerical analysis on flame stabilization of ch 4/air mixture in a mesoscale channel with wall cavities. *Combustion and Flame*, 162(4):1035–1045, 2015. 108

[113] Symeon Karagiannidis, John Mantzaras, and Konstantinos Boulouchos. Stability of hetero-/homogeneous combustion in propane-and methane-fueled catalytic microreactors: Channel confinement and molecular transport effects. *Proceedings of the Combustion Institute*, 33(2):3241–3249, 2011. 123

[114] Tiziano Maffei, Giancarlo Gentile, Stefano Rebughini, Mauro Bracconi, Filippo Manelli, Stefan Lipp, Alberto Cuoci, and Matteo Maestri. A multiregion operator-splitting cfd approach for coupling microkinetic modeling with internal porous transport in heterogeneous catalytic reactors. *Chemical Engineering Journal*, 283:1392–1404, 2016. 123